Investigation on microstructure and mechanical characteristics of stainless steel using Cold Metal Transfer (CMT)

THESIS

submitted to

DELHI TECHNOLOGICAL UNIVERSITY

For the award of the degree of

DOCTOR OF PHILOSOPHY

IN

MECHANICAL ENGINEERING

By

JAYANTA GHOSH ROY

(2K17/Ph.D/ME/37)

Under the supervision of

Dr. N. Yuvaraj
(Department of Mechanical Engineering, DTU)

Prof. Vipin
(Department of Mechanical Engineering, DTU)

DEPARTMENT OF MECHANICAL ENGINEERING

DELHI TECHNOLOGICAL UNIVERSITY

(Formerly Delhi College of Engineering)

Main Bawana Road, Shahabad Daulatpur, Delhi - 110042, India

2022

CERTIFICATE

This is to certify that the thesis entitled "**INVESTIGATION ON MICROSTRUCTURE AND MECHANICAL CHARACTERISTICS OF STAINLESS STEEL USING COLD METAL TRANSFER (CMT)**" submitted to the Delhi Technological University , Delhi -110042, is fulfillment of the requirements for the award of degree of Doctorate in Philosophy in Mechanical Engineering embodies the original research work carried out by **Mr. JAYANTA GHOSH ROY**, Enrollment No: 2K17/Ph.D/ME/37 under my supervision. This work has not been submitted in part or full for any other degree or diploma of this or any other University.

DR. N. YUVARAJ
Department of Mechanical Engineering
Delhi Technological University, Delhi.

PROF. VIPIN
Department of Mechanical Engineering
Delhi Technological University, Delhi.

DECLARATION

I certify that the work which is being presented in this thesis entitled "**Investigation on microstructure and mechanical characteristics of stainless steel using Cold Metal Transfer (CMT)**" in the partial fulfillment of requirement for the award of degree of Doctorate in Philosophy submitted in the Department of Mechanical Engineering at Delhi Technological University, is an authentic record of my own work carried out during a period from August 2017 to May 2021, under the supervision of **DR. N. YUVARAJ** and **PROF. VIPIN**, Department of Mechanical Engineering, Delhi Technological University, Delhi. The matter presented in this thesis has not been submitted in any other University/Institute for the award of any degree or diploma.

01-09-2022

(JAYANTA GHOSH ROY)

Roll No: 2K17/Ph.D/ME/37

ACKNOWLEDGEMENT

I am greatly indebted to my supervisor Dr. N. Yuvaraj and Prof. Vipin, Department of Mechanical Engineering, Delhi Technological University, Delhi, for his invaluable guidance, constant inspiration, numerous suggestions and continued support throughout this research work. I am profoundly grateful to him with reverence for helping me with necessary information and equipment & materials as well.

With great humbleness, I sincerely thank Prof. S.K. Garg, Professor, and Head for his insightful comments and constant encouragement. SRC Committee members and faculty members of Department of Mechanical Engineering, Delhi Technological University for their suggestions and support throughout the research work.

I would also thank with much appreciation the people whose help and support were a great asset; the technical staff at DTU, namely, Mr. Net Ram, Mr. Lalan Kumar Sinha, Mr. Girish Anand, and Mr. Sanjay Gupta who provided great help for conducting the experiments and material characterization; Mr. Sandeep for their help in conducting the XRD studies, Mr. Tek Chand for his help in revealing the microstructures, Mr. Om prakash for his help and assistance in doing the tensile tests.

Finally I dedicate my work to my Parents. My sincere gratitude to my father late Mr. Jitesh Ghosh Roy, my mother Mrs. Neelima Ghosh Roy and my wife Mrs. Soma Ghosh Roy for their blessings and sacrifice which greatly helped me in carrying out this research work.

JAYANTA GHOSH ROY

ABSTRACT

Gas Metal Arc Welding (GMAW) is an effective process of joining of various materials such as stainless steel, aluminum, nickel etc. The cold metal transfer (CMT) welding is the latest innovation of GMAW process with lower heat input for specially joining of lower thickness materials. CMT welding is much suitable for defect free welding with superior quality of thin materials. The microstructural characterization and mechanical properties of the CMT welded joints is found beneficial over conventional GMAW welding processes.

Stainless steel ~~metal~~ is widely using in various industrial and structural applications due to its excellent mechanical, wear and corrision properties. In this research CMT welding process have been applied for studying the the weld bead geomentry and fabrication of thin AISI 304 stainless steel sheets butt welded joints. Studies were carried out to examine the effect of various input welding parameters such as welding current, welding speed and contact-to work-distance (CTWD) on the bead geometry, dilution and heat input of CMT weld bead. Taguchi L9 orthoganal design matrix was applied for finding the optimal process parameters on weld bead geometry. Results shows that welding speed is the most significant welding process parameter, followed by welding current and CTWD on weld bead geometry.

Box-Behnken design matrix under Response Surface Methodology (RSM) technique was applied for finding the optimal input welding parameters to in order to obtain

maximum tensile strength of welded joints. Welding speed, welding current, CTWD and arc correction factors are chosen as input welding parameters and analysed the relationship with tensile properties of welded joints. The optimal welding parameters are welding current of 95 A, a welding speed of 8 mm/sec, CTWD 5 mm and arc correction factor of -10 for obtaining maximum tensile strength of the welded joints. The results show that there is no fracture on the weld joint; the tensile residual stress levels of all the samples are in a controlled manner. FESEM images reveal a dimpled morphology and crack-free tensile fracture surfaces in welded joints.

Ultrasonic vibrations combined fabrication techniques enhances the structural efficiency of manufactured products. It gives an appreciable advantages in microstructural and mechanical properties of products. Ultrasonic assisted Cold Metal Transfer (U-CMT) welding technique is used to join the AISI 304 stainless steel. The welded joints are analyzed using optical microscopy, FESEM and XRD. The mechanical properties of the U-CMT welded joint are evaluated using microhardness, tensile and residual testing and compared CMT welded joints. Two different ultrasonic vibrational amplitude 50 µm & 99 µm and three different welding currents 85A, 90A and 95A were chosen in this study. The microhardness and tensile results of U-CMT welded joint shows considerable improvement in their properties. The U-CMT welded samples experiences enhanced mechanical properties due to refinement of grains in welded region, which is produced by ultrasonic vibrations. The joint prepared by welding current of 95A with ultrasonic vibrational amplitude 50 µm shows better welding properties than other welded samples.

TABLE OF CONTENTS

CERTIFICATE i

DECLARATION ii

ACKNOWLEDGEMENT iii

ABSTRACT iv

TABLE OF CONTENTS vi

LIST OF FIGURES x

LIST OF TABLES xiii

CHAPTER 1 : INTRODUCTION 17

1.1 INTRODUCTION 17

1.2 MOTIVATION 22

1.3 OVERVIEW OF THE THESIS 23

1.4 SUMMARY 25

CHAPTER 2 : LITERATURE REVIEW 26

1.1 INTRODUCTION 26

1.2 GMAW-based Cold Metal Transfer welding 26

1.2.1 Steel alloys 26

1.2.1 Aluminium alloys 34

1.3 ULTRASONIC-ASSISTED CMT WELDING 41

1.4 RESEARCH GAPS 45

1.5 RESEARCH OBJECTIVES 46

1.6 FLOW CHART FOR PRESENT WORK 46

1.7 SUMMARY 48
CHAPTER 3 : EXPERIMENTAL SETUP & PROCEDURE 49
3.1 MATERIAL SELECTION 49
3.1.1 Base Material and Filler material 49
3.2 SAMPLE PREPARATION 50
3.2.1 Macrostructure Characterization 50
3.2.2 Microstructural characterization 50
3.2.3 Microhardness 51
3.2.4 Tensile Testing 51
3.2.5 Residual Stress 52
3.3 EXPERIMENTAL MACHINES 53
3.3.1 CMT Machine 53
3.3.2 Tensile Testing Machine 55
3.3.3 Microhardness Machine 56
3.3.4 Optical Microscopy 58
3.3.5 Field Emission Scanning Electron Microscope 60
3.3.6 X-Ray Diffraction 62
3.3.7 Residual Stress Measurement Machine 64
3.4 OPTIMIZATION OF CMT WELD PROCESS PARAMETERS 65
3.4.1 Process Parameters 65
3.4.2 Taguchi design 67
3.5 EXPERIMENTAL PROCEDURE 68
3.5.1 CMT weld bead 68
3.5.2 CMT Butt Weld Joint 70
3.5.3 Ultrasonic Assisted CMT (U-CMT) Butt Joint 71

3.6 SUMMARY 74

CHAPTER 4 : RESULTS AND DISCUSSIONS 75

4.1 OPTIMIZATION OF PARAMETERS FOR CMT WELD BEAD 75

4.11 Introduction 75

4.12 Opmization of welding parameter 75

4.13 Checking the adequacy of the model for Microhardness response values with ANOVA 86

4.14 Checking the adequacy of the model for Dilution (%) response values with ANOVA 87

4.15 Checking the adequacy of the model for Heat Input response values with ANOVA 88

4.16 Optimal Parameter for weld bead 89

4.2 OPTIMIZATION OF PARAMETERS FOR CMT WELD JOINTS 90

4.2.1 Introduction 90

4.2.2 Select the feasible input welding parameters 91

4.2.3 Design the experimental matrix as per Box-Behnken model 91

4.2.4 To perform the welded joints as per experimental design matrix 92

4.2.5 Recoding the experimental results 92

4.2.6 Developing empirical relationships 94

4.2.7 Use of ANOVA for finding the significant factors 94

4.2.8 Optimized process parameters & confirmation with experimental results 101

4.3 MICROSTRUCTURAL ANLYSIS ON CMT BUTT WELD 102

4.4 MECHANICAL PROPERTIES ON CMT BUTT WELD 107

4.4.1 Ultimate Tensile Strength 107

4.4.2 Microhardness 111

4.4.3 Residual Stress 112

4.5 SUMMARY 117

CHAPTER 5 : RESULTS AND DISCUSSION ON U-CMT BUTT JOINTS 118

5.1 Introduction 118

5.2 COMPARISON BETWEEN CMT AND U-CMT BUTT JOINTS 118

5.1.1 Effect of ultrasonic vibrations on the microstructure 118

5.1.2 Effect of ultrasonic vibrations on the microhardness 130

5.1.3 Effect of ultrasonic vibrations on tensile strength 133

5.1.4 Effect of ultrasonic vibrations on Residual Stress 136

5.3 SUMMARY 139

CHAPTER 6 : CONCLUSIONS AND SCOPE FOR FUTURE WORK 140

6.1 CONCLUSIONS 140

6.1.1 CMT weld bead geometry 140

6.1.2 CMT weld Joint 140

6.1.3 Ultrasonic-Assisted CMT Butt Joining 141

6.2 Scope For Future Work 142

REFERENCES 143

LIST OF PUBLICATIONS 163

CURRICULUM VITAE 164

LIST OF FIGURES

Fig. 1. 1 Current and voltage waveform in CMT [Feng et al., 2009] 19
Fig. 1. 2 Demonstration of CMT welding arc [Fronius, (2004)] 21

Fig. 3.1 XRD Plots of SS 304 50
Fig. 3.2 Tensile test specimen dimensions as per ASTM E8 52
Fig. 3. 3 TPS400i CMT welding machine 53
Fig. 3.4 Tensile machine (Model: Tinius Olsen H50KS) 55
Fig. 3. 5 Microhardness testing machine (Struers Duramin-40) 56
Fig. 3. 6 Olympus GX41 compact inverted metallurgical microscope..... 58
Fig. 3.7 Field Emission Gun Scanning Electron Microscope (FEG-SEM) (Model: FEI QUANTA 3D FEG)..... 60
Fig. 3. 8 X-Ray diffraction (Model: BRUKER D8 ADVANCED)..... 62
Fig. 3 9 Pulstec μ-X360n Full 2D High-Resolution X-ray Diffraction (HR-XRD) machine 64
Fig. 3.10 CMT welding machine setup..... 69
Fig. 3.11 CMT weld bead samples as per design matrix 69
Fig. 3.12 CMT welded samples as per design matrix 71
Fig. 3.13 (a) Ultrasonic assisted CMT welding experimental setup (b) Enlarged view 73
Fig. 3.14 Ultrasonic assisted CMT welded samples 74

Fig. 4.1 Weld bead diagram 75
Fig. 4.2 Macro-images of CMT weld bead samples S1 to S4 77
Fig. 4.3 Macro-images of CMT weld bead samples S5 to S9 78
Fig. 4.4 Control parameters vs Microhardness: Mean Microhardness (HV) at different welding parameters..... 83

Fig. 4.5 Control parameters vs Dilution: Mean Dilution (%) at different welding parameters 83
Fig. 4.6 Control parameters vs Heat Input: Mean Heat Input (J/mm) at different welding parameters 84
Fig. 4.7 Control parameters vs Microhardness: Mean S/N Microhardness ratios at different welding parameters 84
Fig. 4.8 Control parameters vs Dilution: Mean S/N Dilution ratios at different welding parameters 85
Fig. 4.9 Control parameters vs Heat Input: Mean S/N Heat Input ratios at different welding parameters 85
Fig. 4.10 UTS graphs (a) Predicted vs Actual (b) Perturbation plots (c) Contour plot (d) 3-D surface plot 97
Fig. 4.11 Percentage of Elonganation graphs (a) Predicted vs Actual (b) Perturbation plots (c) Contour plot (d) 3-D surface plot 100
Fig. 4.12 Microstructure of weld sample (current of 95A, speed of 4 mm/sec and CTWD of 7mm) **at various position (a) Weld bead (b) Fusion Line (c) Base metal zone (d) HAZ** 104
Fig. 4.13 XRD images of (a) Base material (b) Weld bead 105
Fig. 4.14 FESEM and EDX results of CMT at weld bead (a) The points indicate FESEM image taken on weld bead (b) & (c) FESEM image at point 1 and point 2 respectively (d) & (e) Spectrum image of point 1 with its composition in weight % (f) & (g) Spectrum image of point 2 with its composition in weight % 106
Fig. 4.15 CMT tensile samples after fracture 107
Fig. 4.16 Stress vs strain graphs of CMT and MIG P welded joint 108
Fig. 4.17 (a – d) FESEM images of the fracture surface of CMT welded sample taken at various magnifications and (e & f) EDX was taken at spectrum 3 and 4 points 110
Fig. 4.18 Radiography test as per ASME Sec.-V:2017 of CMT welded sample 111
Fig. 4.19 Microhardness at various position 112
Fig. 4.20 Residual stress graph of welded samples taken at various points 115
Fig. 4.21 Debye ring (3D), distortion and profile curve of residual stress for (a) Higher residual stress sample and (b) Lower residual stress sample 116

Fig. 5. 1 Schematic diagram of weld bead dimensions 119
Fig. 5. 2 Variation in macro images of weld bead geometry of CMT and U-CMT welded samples 120
Fig. 5. 3 Macrostructure (a) and Microstructure of CMT welded sample 9 (95-4-7) at various positions (b) Base metal region (c) HAZ (d) weld region 121
Fig. 5. 4 Macrostructure (a) and microstructure of U-CMT welded sample 6 (95-4-7, 99µm) at various positions (b) Base metal region (c) HAZ (d) weld region 122
Fig. 5. 5 Grain size comparison for U-CMT and CMT samples at (a) Weld bead (b) HAZ 125
Fig. 5. 6 Microstructure of (a) Fusion region & (b) HAZ of sample 3 (U-CMT, 90A & 50µm) and (c) Fusion region & (d) HAZ of sample 4 (U-CMT, 90A & 99µm) 126
Fig. 5. 7 FESEM images of sample 5 (a) and sample 6 (c) and (b) and (d) are enlarged views 127
Fig. 5. 8 EDS analysis of sample 6 (U-CMT) taken at different regions in FESEM micrograph 128
Fig. 5. 9 XRD plots of CMT and U-CMT welded samples 130
Fig. 5. 10 Micro-hardness variation of welded joints 131
Fig. 5. 11 Microhardness of welded samples (a) Base Metal region (b) HAZ (c) Weld region 133
Fig. 5. 12 UCMT Tensile samples (a) Before testing (b) After tensile testing 134
Fig. 5. 13 Stress-strain curves of welded samples 135
Fig. 5. 14 FESEM fractography of tensile fractured surface of (a) CMT sample -9 and (b) U-CMT sample-6, (c) and (d) are higher magnification views 136
Fig. 5. 15 Residual Test results of welded samples taken at various points 137
Fig. 5. 16 Residual stress distortion and profile curve of (a) Lower residual stress sample 6 and (b) Higher residual stress sample 8 at weld bead 138
Fig. 5. 17 Radiography inspection test of U-CMT sample 6 139

LIST OF TABLES

Table 2. 1 Major conclusions on GMAW-CMT welding of steel based similar metals 30

Table 2.2 Major conclusions on GMAW-CMT welding of steel based dissimilar metals 32

Table 2. 3 Major conclusions on GMAW-CMT of Aluminium alloys 38

Table 2.4 Major conclusions on Ultrasonic assisted welding process (U-CMT) 43

Table 3. 1 Chemical compositions (wt%) of AISI 304 SS and ER 308L SS 49

Table 3. 2 Mechanical properties of base material 49

Table 3. 3 CMT welding machine specifications (TPS 400i) 54

Table 3. 4 Tensile Testing Machine specifications 56

Table 3. 5 Microhardness testing machine specifications 57

Table 3. 6 Optical Microscope specifications (Make:Olympus GX41) 59

Table 3. 7 FESEM specification 61

Table 3. 8 Specification of XRD machine 63

Table 3. 9 Residual stress machine specifications 65

Table 3. 10 Design of experiments for CMT weld bead. 67

Table 3. 11 Taguchi design matrix for CMT weld bead 68

Table 3. 12 Welding parameters and their levels for CMT Butt Joints 70

Table 3. 13 Experimental welding parameters for different welding process 72

Table 4. 1 Welding parameters and their response variables with S/N ratios 76

Table 4. 2 Response table for mean Microhardness 81

Table 4. 3 Response table for mean Dilution 81

Table 4. 4 Response table for mean Heat Input 81

Table 4. 5 Response table for S/N ratios for Microhardness 81

Table 4. 6 Response table for S/N ratios for Dilution 81

Table 4. 7 Response table for S/N ratios for Heat Input 82

Table 4. 8 ANOVA for Microhardness response variable 86

Table 4. 9 ANOVA for Dilution (%) response variable 87
Table 4. 10 ANOVA for Heat Input response variable 89
Table 4. 11 Predicted vs Experimental results 90
Table 4. 12 Welding Input parametes and their levels CMT welded joints 91
Table 4. 13 Design matrix and experimental results of CMT welded joints 93
Table 4. 14 ANOVA test results for Ultimate tensile strength 95
Table 4. 15 ANOVA test results for % of Elongation..... 98
Table 4. 16 Optimized condition for CMT welded joints..... 101
Table 4. 17 Validation of the test results..... 102

Table 5. 1 EDS main elements in the SEM micrograph (Fig. 5.7) of CMT and U-CMT (in w%)..... 128
Table 5. 2 Selected CMT & UCMT welding parameters and welded joint results 131

NOMENCLATURE

AA	Aluminium Association
Al	Aluminium
ANOVA	Analysis of variance
ASTM	American Society for Testing Materials
BCP	Background Current Phase
BHN	Brinell Hardness Number
BM	Base Metal
CAV	Constant Arc Voltage
CMT	Cold Metal Transfer
CO	Carbon Monoxide
CO_2	Carbon Di-Oxide
CSC	Conventional Short Circuit
CTWD	Contact Tip To Workpiece Distance
Cu	Copper
DCEN	Direct Current Electrode Negative
DCEP	Direct Current Electrode Positive
DCRP	Direct Current Reverse Polarity
DE	Design Expert
DOE	Design of Experiments
DPC	Digital Process Control
EDM	Electrical Discharge Machine
EDS	Energy Dispersive Spectrometer
EDX	Energy Dispersive X-ray
FESEM	Field Emission Scanning Electron Microscope
FL	Fusion Line
FZ	Fusion Zone
GMAW	Gas Metal Arc Welding
GTAW	Gas Tungsten Arc Welding
HAZ	Heat Affected Zone

HR-XRD	High-Resolution X-ray Diffraction
IMC	Inter-Metallic Compounds
IML	Inter-Metallic Layer
Mg	Magnesium
MIG	Metal Inert Gas
NDT	Non-Destructive Technique
OCV	Open Circuit Voltage
PCP	Peak Current Phase
PDC	Pulse Dynamic Correction
PWHT	Post Weld Heat Treatment
RSM	Response Surface Methodology
RT	Radiography Technique
SAW	Submerged Arc Welding
SCP	Short Circuiting Phase
SEM	Scanning Electron Microscope
SMAW	Shielded Metal Arc Welding
THI	Thermal Heat Input
TIG	Tungsten Inert Gas
U-CMT	Ultrasonic Assisted Cold Metal Transfer
UTM	Universal Testing Machine
UTS	Ultimate Tensile Strength
VHN	Vickers Hardness Number
VP-CMT	Variable Polarity Cold Metal Transfer
WFS	Wire Feed Speed
WM	Weld Zone / Weld Metal
XRD	X-Ray Diffraction

CHAPTER 1 : INTRODUCTION

1.1 INTRODUCTION

For fabrication of various industrial applications such as automotive components, defense products, aerospace parts, power plants elements, shipbuilding components, structural elements, heat exchangers, turbines, rail coaches, chemical plants, gas & oil industries, etc., and others many applications, the majority of joining takes place by fusion welding processes. The various materials are effectively joined by a variety of fusion welding techniques which includes Shielded Metal Arc Welding (SMAW), Submerged Arc Welding (SAW), Gas Metal Arc Welding (GMAW), Gas Tungsten Arc Welding (GTAW), etc. [Satyanarayana 2005].

GMAW, called Metal Inert Gas welding (MIG) or Metal Active Gas (MAG) welding, is an electric arc between a consumable wire electrode and the workpiece metal. It heats the workpiece, enabling them to melt and join with an external supply of shielding gases. GMAW is a very stable welding process with a higher metal deposition rate due to higher heat input, widely used in manufacturing [Ibrahim, 2012]. GMAW is based on conventional short-circuit transfer (CSC) mode, enabling the liquid droplet detachment from filler wire due to Lorentz forces. The electromagnetic field, which surrounds the electrode, provides the power, which squeezes (more commonly known as a pinch) the molten droplet from the end of the electrode. In the GMAW process, various defects are forming due to high thermal heat input. The welding defects are metal penetration, cracks,

the spattering of filler material and distortion, etc. Fronius of Austria 2004 developed Cold Metal Transfer (CMT) welding as a modified and upgraded version of the conventional GMAW welding process, which is based on short-circuiting transfer process [[Kumar et al., (2016)]. Cold Metal Transfer incorporates a digitally controlled method of material deposition with very low thermal input by a super innovative wire feed mechanized system coupled with high-speed digital control [Irizalp et al., (2016); Lin et al., (2010)]. GMAW-modified CMT welding process provides low heat input during the welding process. This process is very suitable for welding thin materials with the slightest distortion, less dilution rate, and less structural stress with lower residual stress in the weld area [Selvi, 2017; Cao, 2014].

In the CMT process, the electrode wire is moved towards the molten weld pool at the arcing phase of the electrode. Here the electrode wire tip establishes contact with the molten weld pool, then the arc extinguishes, and the welding current drops to a sub-zero level. It helps result in the avoidance of any spatter generation. Due to the lesser welding current, the heat input during the short-arc variation is comparatively reduced, making it proven to weld remarkably thinner materials without distortion and residual stress in the weld joints. The movement of the wire is reversed by digital process control helps droplet detachment during the short circuit phase. The wire retracting motion is caused by the retractor mechanism of the CMT by the digital process control mechanism. The wire feeder of the machine returns the drawing force and transfers the metal droplets into the molten weld pool. The arc then reignites, and the sequence of the process begins all over again by itself. It is found that the CMT technique helps to decrease the heat affected zone

width due to its considerable low heat input to the base metal, which is the most pioneering feature of this process. Due to the temperature variations between the welds and the parent metals while welding, remarkable effects were observed on the metallurgical characteristics of weld material, residual stresses, as well as on dimensional accuracy and shape aesthetics of the weld joints [Koli et al., (2021 a); Tian, (2018)].

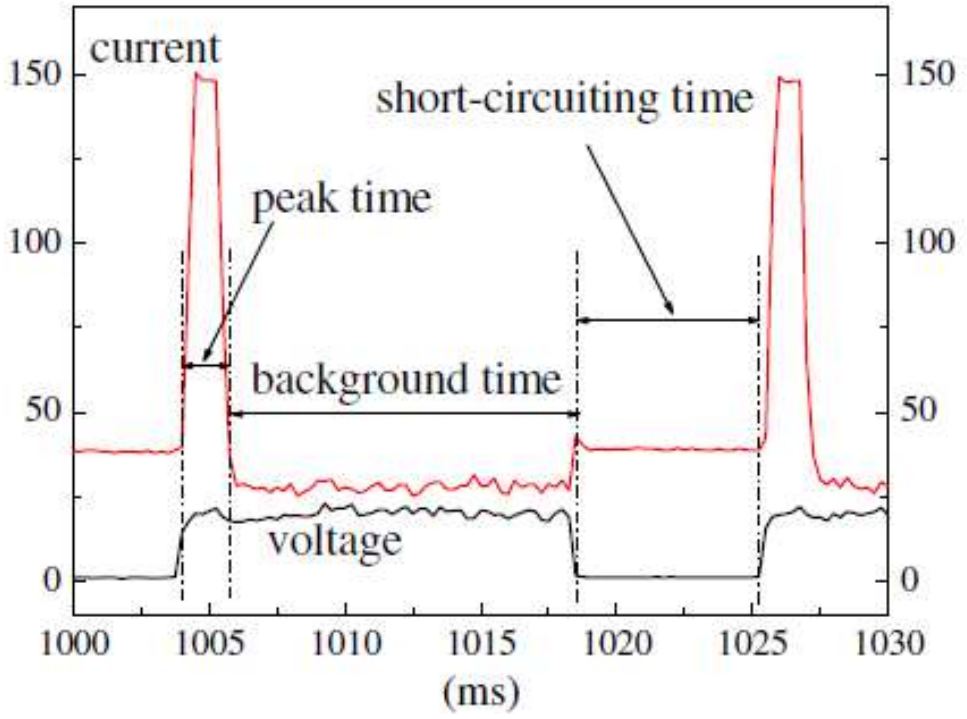

Fig. 1. 1 Current and voltage waveform in CMT [Feng et al., 2009]

The typical electrical signal cycle in CMT is defined as the period needed for depositing the liquid droplet from the electrode wire. The current and the voltage is analyzed to assess the energy divisions associated with various phases of the transfer [Feng et al., (2009); Pickin et al., (2011)]. The CMT cycle of the current-voltage waveform is shown in Fig 1.1. The cycle indicates the following three distinguished phases:

The peak current phase: Here a high pulse current caused due to the arc ignition, heats the electrode wire which produces a droplet. The arc voltage remains constant in this phase.

The background current phase: This corresponds to a much lower current phase. The droplet formed in the peak current phase at the tip of the electrode wire prevents the globular transfer as the current is minimized to a non-zero level. This also causes considerably much too avoid spattering formation. Thus, better bead aesthetics is observed. No distortion takes place even for thin sheet welding by CMT due to such a non-zero level of current, causing significantly less heat input. This phase is comparatively longer and continues till the next short-circuiting step starts.

The short-circuiting phase: At the end of the background time phase, the short-circuiting phase occurs where the arc voltage drops to zero. The electrode wire at this point contacts the molten weld pool, causing the short circuit. At the same time, the digital process control mechanism, through its return signal, pulls back the electrode wire by a reversing force. This helps transfer the metal from the wire in the form of a droplet to the molten pool caused by the fracture of the liquid bridge. Thus, the wire is retracted, and the next cycle begins.

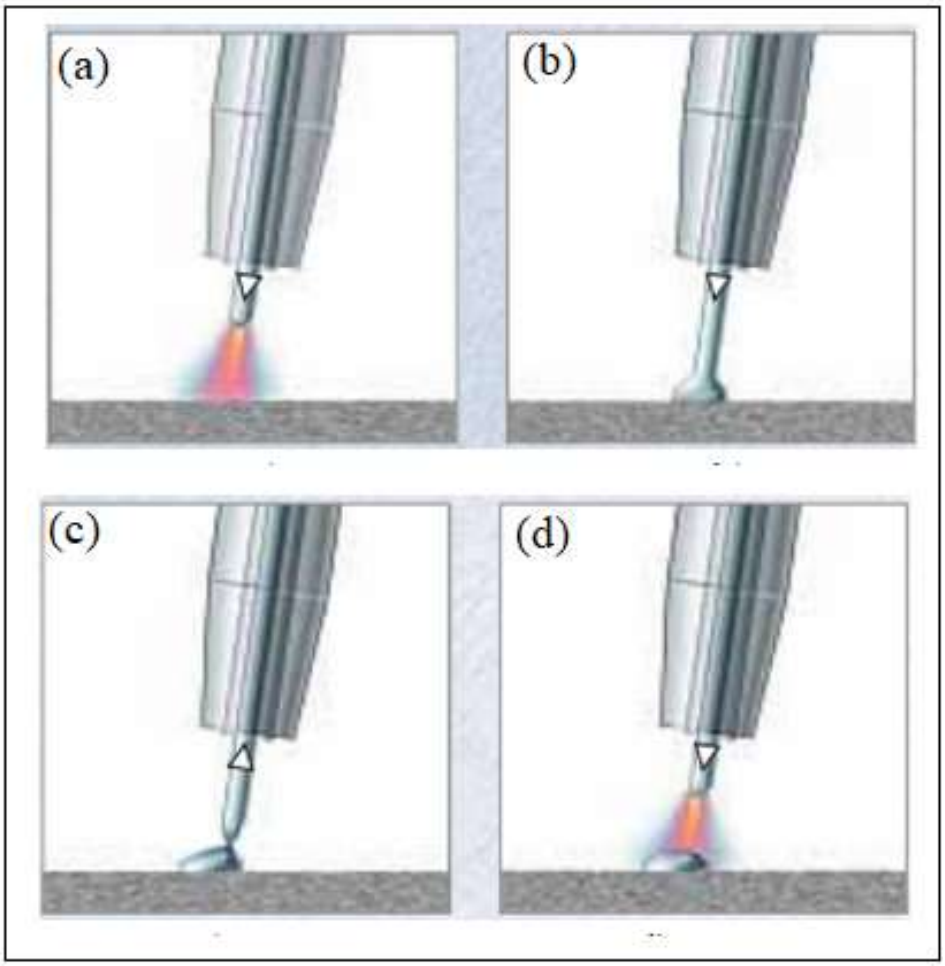

Fig. 1. 2 Demonstration of CMT welding arc [Fronius, (2004)]

CMT is a cold process that constantly moves alternately between hot and cold phases. During the time of initial arcing period, the electrode filler is moved towards the molten pool (Fig. 1.2 (a)) the arc is initiated and is known as the hot phase. In the next phase (Fig. 1.2 (b)), the filler wire dips into the molten pool, the arc is fully pulled out, and the welding current is considerably lessees to a sub-zero level, called as cold phase. The retracting reverse movement of the wire forms the droplet, detached during the short circuit mode at a lower current. (Fig. 1.2 (c)) termed as another cold phase. At last, the wire motion is

reversed by a digital mechanism, and the process restarts again (Fig. 1.2 (d)), which is finally called the hot phase.

1.2 MOTIVATION

New welding methods replace traditional techniques in modern engineering applications and industrial purposes. CMT, a modified version of GMAW, is now used world wide for better bead aesthetics, negligible spatter generation, and, most notably, lower heat input best applied for thin sections welding different materials [Cao et al., (2013); Lin, 2013]. These characteristics have made CMT unique in its applications and very popular throughout the length and breadth of renowned industries. There will be approximately 1/4th of the total time in the CMT welding in short-circuit phase; during this time, the current magnitude turns to zero. It reduces the cost of welding by around 30% to 40% reduction in energy consumption. AISI 304 consists of 18% chromium, which makes it highly corrosion-resistant, with good toughness and ductility. The role of 8% Ni is to stabilize the austenite, which promotes ductility, which, in the absence, can lead to forming a magnetic martensitic structure. AISI 304 stainless steel is being used in several areas such as food processing, dairy equipment, architectural structures, chemical, rail, transportation, aerospace industries, nuclear power plants, pressure vessels, cryogenic, petrochemical units, and sanitary appliances because of their excellent properties like strength, non-magnetic, lower thermal and electrical conductivity in comparison with other carbon steels [Kumar and Shahi, (2016); Jha (2003); Baek, (2001); Taraphdar (2020 a)].

The consumption of 304 and 304L stainless steel is approximately 20,000 tons per year according to the global market size [Singh et al., (2018 a)]. Traditionally carbon steels are welded using GMAW, GTAW, and SMAW process provides high heat input which is the cause for the creation of coarse grains and wider heat affected zone [Raghu Nathan et al., (2015)]. GTAW is an effective welding process for joining thin carbon steels with good quality weld and aesthetic bead appearance. Slower welding speed, less deposition of metal, and lack of penetration are a few disadvantages of the GTAW process. GMAW modified CMT welding process provides low heat input during the welding, which is very suitable for welding thin materials. The lesser amount of distortion, less dilution rate, and less structural stress with lower residual stress in the weld area [Cao et al., (2014)]. The difference between conventional GMAW and CMT is the liquid droplet mode detached by the electrode wire [Zhang et al., (2020)]. In addition, ultrasonic vibration-assisted welding has significantly contributed to the further enhancement of the welded joint. Thus fabrication of thin sheet stainless steel welding with CMT technology assisted by ultrasonic vibration has become an interesting phenomenon to study and research.

1.3 OVERVIEW OF THE THESIS

Chapter 1 includes the introduction of CMT and the motivation behind using CMT in place of its parent process, GMAW.

Chapter 2 includes a literature review related to CMT and U-CMT. It discusses various outcomes by the researchers in the field of different types of material being joined by using these processes with research gaps. The research objectives and flow diagram of experimentation are discussed.

Chapter 3 includes CMT mechanism, materials, methods and experimentation, and information about the fabrication of butt joining of similar material (AISI 304) using CMT and Ultrasonic-assisted CMT (U-CMT). Working principle of CMT welding and information regarding using ultrasonic vibrations during CMT welding. Experimental welding input process parameters and procedures are elaborated on in this section. Information regarding the microstructure, micro-hardness, tensile test, and residual stress has been explained.

Chapter 4 includes results and discussion on CMT weld bead on plate and CMT butt joints of stainless steel 304. Optimization of input welding parameters for achieving the maximum micro-hardness of the fusion region and dilution of the weld bead through the Taguchi L9 design matrix. The optimized input welding parameters were identified for reaching the maximum welded joint strength properties using Response Surface Methodology (RSM) technique. Confirmation tests from the predicted optimal parameters are also carried out to validate the test results. The microstructural analysis, micro-hardness, tensile properties, and residual stresses of the welded joint are discussed.

Chapter 5 includes results and a discussion on ultrasonic-assisted CMT (U-CMT). Welding process. The influence of various welding parameters on microstructural analysis, micro-hardness, tensile properties, and residual stresses is included in this chapter. Comparison is made without ultrasonic assisted vibrations produced by welded joints.

Chapter 6 includes the conclusion drawn from this research work, significant contributions, and the future scope of the research study.

1.4 SUMMARY

Thin materials joining through welding have several difficulties such as burn-through, high residual stresses, distortion, lower mechanical properties, etc. This chapter briefly overviews joining thin SS304 materials through cold metal transfer welding techniques. The advantages and limitations of the GMAW process in thin welding sheets are illustrated. CMT mechanism of welding and benefits of using CMT process over GMAW process with its application also discussed. The motivation behind using CMT in place of its parent process GMAW is illustrated. The organization of the thesis is also presented.

CHAPTER 2 : LITERATURE REVIEW

1.1 INTRODUCTION

This chapter presents a literature review on GMAW-based Cold Metal Transfer Welding (CMT) and Ultrasonic Assisted Cold Metal Transfer Welding (U-CMT) Techniques. Based on the literature review, the research gap and objectives of the work are identified. Finally, a plan of work to fabricate the welded joints is presented. The literature review is discussed in the following area.

- GMAW-based CMT welding of similar and dissimilar steel alloys
- GMAW-based CMT welding of Aluminium alloys
- Ultrasonic-assisted CMT welding

1.2 GMAW-based Cold Metal Transfer welding

1.2.1 Steel alloys

Kannan et al., (2019 a) studied the CMT welding of 2mm 316L SS sheets with a different arc correction factor for finding the tensile properties. Tensile properties of the joint enhanced with an increase in arc length correction from 0% to 20%. Higher arc length correction improves the filler reinforcement in the welded joint. 316L SS sheets welded at 300mm/min welding speed and a welding current of 105A have the best weld profile with sound joints [Kannan et al., (2019 b)].

Ahsan et al., (2017) studied the CMT process of hot rolled steel sheets with three different filler wires with varying deoxidizing elements such as silicon and

manganese to detect the slag's oxygen content and weld pool. A lower quantity of deoxidizers produces good quality weld joint with greater than 0.006 wt% of oxygen in the welded region. An increase in oxygen changes the temperature gradient of surface tension with lower deoxidizers. Ahsan et al., (2016) studied different heat input rages for welding of CMT-GMAW of Zinc coated steels and found that very low and high heat has an increased tendency to form porosity in the weld beads. Optimized values of heat input range from 200 to 250 J/mm welded joints have reduced the porosity with lesser defects.

Balbande et al., (2019) performed 3 mm duplex stainless steel and super austenitic stainless-steel dissimilar joint by CMT technique and studied the tensile properties. The fine dendritic Mo content structure in the joint resulted in the crack-free weld joint. Luchten-Berg et al., (2019) reviewed the different heat inputs of S32205 for welding Duplex stainless steel with the CMT process, the change in heat input changed the ferrite/austenite balance in the fusion region of a welded joint. Higher heat energy increases the intergranular austenite formation and decreases ferrite formation.

Zhou et al., (2019) used ER 308L filler wire to weld the AISI 430 ferritic stainless and studied the effect on grain size in the fusion zone and HAZ. The tensile strength of welded samples does not show any remarkable changes compared to the base metal. The strength of the HAZ mainly depends upon the formation of intergranular martensite, and carbide dispersion generates a stronger effect than the formation of

ferrite grain size. Dharmik and Lautre, (2020) found that CMT welded CRNGO 0.5mm thin electrical sheets had lesser heat affected zone than GMAW and GTAW welded samples due to more secondary heat input and smaller grain size in the welded region. Stanciu et al., (2017) reported that in CMT welding of 1mm low S235JR low carbon steel sheet, by increasing the welding speed, improper penetration took place and reduced the wire speed reinforcement.

Jan et al., (2014) compared CMT mode arc with standard and pulsed arc modes in laser hybrid welding of thicker steel sheets and observed that CMT mode produces a narrower HAZ than other processes. The reduction of power with the higher stability of beads and lesser HAZ is advantageous in use on CMT arc mode. Babu et al., (2019) studied the CMT process's lap joining of AA2219 to AISI 321 steel. The strength of the welded joint depends on the thickness of the Al coating on steel prepared by friction surfacing before welding. Similarly, Zhang et al., (2008) investigated the Q235 zinc coated low carbon steel with 6061 aluminum alloys through the CMT process. The strength of the joint was increased with lower heat input compared with high input joints.

Benoit et al., (2011) reported that CMT welding is an exemplary process for welding Inconel 718 alloy in comparison with GMAW welding. The microstructural analysis has confirmed that there is no lack of fusion in the joint due to the excellent quality of the prepared weld joint. The HAZ of the CMT welded sample has a small size (0.5 mm) compared to the same sample welded by the GMAW process. The large size of

dendrites is observed in the HAZ of the GMAW process. Ghosh et al., (2009) reported metal transfer's arc characteristics and behavior in pulse current GMAW of stainless steel and compared it with conventional GMAW. The pulse parameters were a significant key to controlling the arc and metal transfer behavior in pulsed GMAW. Costanza et al., (2016) studied the weldability of AISI 316 & AISI 304 stainless steel by GMAW process with various shielding gas compositions, i.e., 98%Ar +2% H_2, 95%Ar+5%H_2, 100%Ar, 90%Ar+8%CO_2+2%O_2, 95%Ar+5%H_2. The 90% weld joint efficiency was obtained with the samples welded with 98%Ar +2% H_2 & 100%Ar shielding gas compositions. Meena et al., (2017) studied the welding of AISI 304 SS by GMAW process with different welding parameters such as welding current, voltage, and welding speed. They found that welding current is a more influencing factor for weld joint strength due to finer grain size in the fusion region.

Chen et al., (2017 a) reported CMT welding of mild steel with a current range from 250 A to 320 A resulted from excellent regular and stable welding, whereas beyond this current range, the welding was very unstable. Yagati et al., (2019) studied the effect of Al–5%Si and Al–12%Si filler wire on joining Al 6061-T6 to Interstital steel by CMT brazing and found that jointly made prepared with Al–12%Si filler wire recorded superior quality. Ola and Doern, (2014) reported that the CMT process was a good technique for producing the low-dilution cladding of the INCONEL 718 superalloy without any defects.

Kumar and Shahi, (2011) studied the dissimilar GTAW of 316L SS with S32205 duplex SS. With higher heat input during welding, the grain size of the weld metal and HAZ area increased. Lower heat input is selected to reduce HAZ and grain coarsening to improve mechanical properties. CMT-based welding of similar and dissimilar steels is investigated by various researchers and is exhibited in Table.2.1 and 2.2, respectively.

Table 2. 1 Major conclusions on GMAW-CMT welding of steel based similar metals

Researcher Name	**Material Investigated & Filler wire diameter**	**Shielding Gas & Flow rate**	**Welding Parameters**	**Prominent Results**
Li et al., (2014)	Mild Steel Plate 10 mm; ER70S-6, 1.2 mm	Argon + 20% CO_2 20L/min	Welding speed 1 m/min CMT arc mode Current – 198 A Standard arc mode Current – 204 A Pulsed arc mode Current – 235 A	CMT arc mode was the most stable arc and resulted in the least spatter compared with other arc modes. CMT welded samples have highest tensile strength, then pulse arc mode and the smallest observed in standard arc mode samples.
Ahsan et al., (2016)	Zinc Coated Steel 2mm; ER70S-3 1.2mm		Current – 120 A to 263 A Voltage – 12 V to 20 V Speed – 40 cm/min to 120 cm/min	The zinc bubble could not grow at lower heat input, resulting in less porosity. On the other side with the high heat temperature, the zinc bubble could grow and, lesser chances of escape due to the molten weld pool slowing down the solidification.

Stanciu et al., (2017)	S235JR Low carbon steel; ER70S-6 1.2 mm	82% Argon & 18% CO_2 15L/min	Current – 85 A Voltage – 18.3 V Welding speed 600mm/min, 800mm/min and 1000 mm/min	CMT welded samples have better results than synergic pulse welding samples. Increase in welding speed results in improper penetration
Kannan et al., (2019 b)	AISI 316L SS 2 mm; ER 308L	98% Argon & 2% CO_2 20L/min	Current - 105A welding Speed - 350mm/min Arc length correction factor from -20% to +20%.	Increased arc length correction factor improves the tensile strength due to increase in reinforcement. Tensile strength of 569 MPa and percentage elongation of 36.47% were observed for +10% arc correction factor samples.
Dharmik and Lautre, (2020)	CRNGO steel sheets 0.5 mm; $ERCuSi_3$, ER316L & ER70S6,			Better mechanical properties were observed in CMT samples due to less HAZ than GMAW and GTAW samples.
Chen et al., (2017 a)	Q235 mild steel 3mm; ER50-6 1.2 mm	Pure CO_2 15 L/min	Wire feed-83.33mm/sec Welding Speed-8.33mm/sec	With an increase in boost current and duration, the deposition rate of the droplets, size of the droplet, weld width and penetration also increases.

Table 2.2 Major conclusions on GMAW-CMT welding of steel based dissimilar metals

Researcher Name	Material Investigated & Filler wire diameter	Shielding Gas & Flow rate	Welding Parameters	Prominent Results
Zhang et al., (2008)	Q235 low carbon steel 1mm & Al6061; AlSi5 1.2 mm	Argon 15L/min	Feed rate - 3.7 m/min to 3.8m/min Speed - 13.9 m/min to 14m/min	In dissimilar welding, the intermetallic layer formed between the two materials mainly in the $FeAl_3$ phase. The strength of the joint is increased due to less heat input, which affects the intermetallic layer.
Yang et al., (2013)	Zinc coated low Carbon Steel (1.2mm) & Al6061-T6 (2mm); ER 4043 1.2mm	Pure Argon 16L/min	Welding speed - 0.5m/min Pre-set gap distance of 0mm, 0.1mm, 0.3mm & 0.5mm Offset distance of 0mm, 1mm & 2mm.	The presetting gap helps to escape the zinc vapor during welding. Weld strength was directly proportional to the preset gap and inversely to offset distance.
Lin et al. (2013)	Zinc coated low carbon steel (0.7mm, 1.2mm) & Al6061-T6 (2mm) ER 4043 CMT Brazing		Current - 70A Voltage - 11.5V Speed – 0.7 m/min	Higher joint strength in 1.2mm thick carbon steel CMT brazed with Al 2mm sheet and lower joint strength in 0.7mm thick steel sheet CMT brazed with Al 2mm sheet were reported.
Babu et al. (2019)	AISI321 SS (3mm) & Al2219 (3mm); Al 4047 1.2mm	Argon 15L/min	Current -70A Speed - 400mm/min Before CMT welding, the surface of SS sheet was friction surfaced with Al with	With increases in Al coating from 0.3 mm to 1.2 mm on surface, the intermetallic thickness layer is decreased from 5 microns to 0.4 microns, which reducing Aluminums

			different thicknesses from 0.3mm to 1.2mm.	liquid wetting on stainless steel. Higher Joint strength of 260N/m produced with 0.6 mm coating surfacing.
Chen et al. (2019)	Q235 Low Carbon Steel 2mm & Al5052 2mm; ER5356	Argon Gas flow rate - 15L/min	Welding Speed - 1.5m/min to 4 m/min Wire feed rate - 3.1, 4.1, 5.1 m/min	An increase in wire feed rate decreases the strength of the CMT joint due to an increase in thick brittle inter metallic layers.
Yang et al. (2019)	Q235 Low Carbon steel 1.2mm & Al5754 1.8 mm; ER4043 diameter 1.2 mm.		Current – 67A to 69 A Voltage - 10.9V to 11.8V Speed – 3 mm/sec to 7 mm/sec Wire feed rate - 4m/min	CMT Steel/Al joints with low heat input lesser than 157 J/mm formed only $Al_{7.2}Fe_{1.8}Si$ single phase intermetallic layer and with heat input 210J/mm above multi-phase intermetallic layer of $FeAlSi_3$ and $Al_{7.2}Fe_{1.8}Si$ formed. Low heat input formed sound joint with good bonding due to thin interface single phase layer.
Mou et al., (2019)	SS304 2mm & Titanium alloy TC4 2mm; ERCuSi-A Filler wire	Argon 25L/min	Welding speed – 45cm/min Wire feed rate – 3.5m/min to 5.5m/min Welding current – 60A to 110A Welding Voltage 10.8V to 11.3V	At a higher welding feed rate of 5.5 m/min highest strength of 294 MPa was reported due to an increase in speed. The thickness of Cu/Ti layer also increases. The bonding between Cu/Ti and Cu/Fe layer mainly affects joints' fracture.

1.2.1 Aluminium alloys

Xu et al., (2020) welded DC56 galvanized mild steel with a thickness of 1.5mm and Al6451 alloy with a thickness of 0.8 mm by ER1100 filler wire by CMT variable polarity process and studied the intermetallic compounds (IMC) and zinc accumulation in welded joints. The IMC layer at the Al/steel interface consisted of a significant Fe_2Al_5 with polygonal grains adjacent to the steel and a minor serrated FeAl3 adjacent to the Al side. The weld joint strength was governed by Zn accumulation near the Al/steel interface and the IMC growth at the Al/steel side interface. An insufficient heat input induced Zn accumulation in the fusion region, leading to the formation of Al-Zn hypo eutectoid structure with shrinkage around the Al/steel interface, which results in deterioration of weld joint strength.

Tang et al., (2020) investigated Inconel 718 and ferrous alloy SUS316 with 3 m thickness by $ERNiFeCr_2$ filler by CMT process with different currents (130 A, 160 A & 192 A), and welding speeds (3 mm/sec, 4 mm/sec, 5 mm/sec, 6 mm/sec, 7 mm/sec & 8 mm/sec) and studied the tensile properties of the welded joints. The tensile strength of welded joint decreases with a decrease in welding speed due to the formation of the Ni-Fe phase in the fusion line of a welded joint. In the Ni-Fe fusion line region, stress concentration occurs with higher temperatures and makes the different joint fusion lines weak, resulting in a decrease in weld collective strength.

Elrefaey, (2015) reported that CMT-produced welded joints have better tensile properties than the GMAW process that produced 7075-T6 aluminum alloy. The base metal region

has higher hardness, and HAZ has a marginally lower hardness than base metal and the lowest hardness in the fusion region.

Ahmad and Bakar, (2011) fabricated AA6061 welded joints by CMT process and studied the tensile and hardness of the fabricated joints and post-weld heat treatment (PWHT) joints. The tensile strength of the welded joint is 55.32 Mpa, and PWHT welded join tensile strength is 53.31Mpa. The tensile strength of the joint is improved with PWHT due to enhancement of microstructural properties. Similarly, the hardness value of the PWHT samples is improved by 25.6% compared to welded joints with heat-treated samples. The fusion region hardness value of the welded sample is around 68.8HV. With the application of PWHT, there is a significant improvement in the strength of the welded joints.

Zhang et al., (2013) concluded that Al6061 welded with Laser-CMT hybrid technique gets finer grain size with narrower columnar dendrite zone. The tensile strength of the hybrid welded joint is obtained at 223MPa, which is 10 % higher than the Laser-MIG hybrid welded joint. The results revealed that Laser-CMT hybrid welding is a probable technique for joining thin aluminum alloy sheets.

Pang et al., (2016) reported that CMT with pulses is a stable welding process without a spattering of welding of Al6061-T6 alloy than without pulses welding. With increased pulses in CMT welding, deeper penetration with a higher bead contact angle was obtained. Pavan Kumar et al., (2016) fabricated Al6061 alloy thin sheets with the same filler wire composition by pulsed CMT welding. They found that the joint exhibits a quasi-binary composition, resulting in less susceptibility to solidification cracking. The reduced HAZ

area, reduction of intermetallic phases, and thin fusion line were observed in the welded joints due to refined recrystallization grains in the fusion region. Welding current range of 60-70A and speed range of 8-10mm/s is suitable for producing fine quality welded joints with better mechanical properties. Madhavan et al., (2017) found that CMT welding of Al 6061 alloy and AZ31B Magnesium alloy and revealed that pitting corrosion resistance was found with high heat input resulted in lower tensile strength due to compressive residual stress in the weld zone.

Lei et al., (2017) found that CMT welding of Al6061-T6 1 mm thick welds has good weld joints without welding defects such as porosity, partial tearing, etc., which results in better mechanical properties in comparison with MIG pulsed and standard mode welded joints. The Fusion region of the welded joint has the weakest area due to some micropores observed compared to HAZ.

Liang et al., (2018) investigated the effect of GTAW current in microstructural characterization and mechanical properties of Al6061-T6 alloy welded with GTAW-CMT hybrid welding technique. The addition of GTAW current during welding results in appreciable metal penetration taking place in the joints. CMT welding current under 100A is generated in controlled short-circuit transition. Within low GTAW current with CMT hybrid process enhances the strength properties of the welded joint due to the heat input more molten base material mixes with weld material.

Feng et al., (2009) reported that CMT welded pure aluminum thin sheet have a better appearance without spatter due to low heat input, reduces the deflection deformation, and develops the gap bridging of the sheets. Similarly, Pickin and Young, (2006) reported

that CMT welding of thin aluminum alloy has high filler wire melting with lower heat input.

Girinath et al., (2019) studied the effect of three different torch angles (-100, 00, +100) on the formability of AA5052 alloy by CMT welding. Weld blank prepared by -100 torch angle has more formability than other torch angles due to arc preheating. Dutra et al., (2015) used two different Al 5183 and Al 5087 filler wires for CMT welding of Al5083H116 alloy. The welded joint produced by Al 5087 filler wire has higher tensile strength than Al5183 filler wire due to the increased extent of pores in the joint. Both the filler wire fabricated joints showed the same toughness.

Liu et al., (2013) investigated double pulsed GMAW of Al5754 alloy and found that the tensile strength of the welded joint is around nearly the base material. The grain size of the welded joint decreases owing to the high-frequency pulse occurs of droplet metal transfer. The uniform distribution of Mg_2Si precipitates in the fusion region enhances the strength properties of the joint.

Feng-yuan et al., (2015) found that Al7A52 CMT welded joint with the number of passes. The grain size of the fusion region is refined with heat treatment. With an increase in weld passes, the coarse grain boundary occurs between weld passes, which enhances the mechanical properties. Various researchers are investigating CMT-based welding of different aluminum alloys are exhibited in Table.2.3.

Table 2. 3 Major conclusions on GMAW-CMT of Aluminium alloys

Researcher	Material investigated	Shielding gas & Flow rate	Welding Parameters	Prominent Results
Comez et al., (2020)	Al5754 - H22 & Al7075-T6; ER5356	Argon gas	Current (87, 104 & 120 A), Welding speed (0.5 & 1 m/min), Heat input (74.69, 94.61, 108.99 J/mm)	The tensile strength of dissimilar joints for all heat input welded samples was approximately above 230 MPa. Increase in heat input above 74.69 J/mm, the tensile strength of welded joint marginally decresed to and it was not extreme due to Al5754 alloy does not go through over-aging. The corrosion resistance of the joints decreases with an increase in heat input.
Lei et al., (2017)	AA6061-T6, 4 mm thick; ER4043		Current 500 A, Wire feeding speed (5, 5.5 & m/min), Welding speed (7, 7.5 & 8 m/s), Wire withdrawal (0, 1.5 & 3 mm)	Solidification cracks of CMT welding of Al-Si increase with an increase in welding speed and, the crack rate reduces with increase in wire feed rate and wire withdrawal rate. The most significant factor for reduction of crack is wire withdrawal, followed by welding speed and welding current.
Ahmad and Bakar, (2011)	AA 6061 10mm thick; ER 4043, 1.2 mm dia	Argon	Current 210A, Voltage – 24V Wire feed- 190 mm/sec	By implementing post-weld heat treatment, there was a 3.8% increase in tensile strength and hardness by 25.6%.
Zhang et al., (2013)	AA6061 aluminum alloy 2mm; ER5356 1.2mm dia	Argon Flow of torch to nozzle 20L/min & to root nozzle 10L/min	Current 63 to 105A Welding speed-91.67mm/sec Wire feed speed-66.66, 83.33, 100mm/sec	The weld gets finer microstructure and a narrower columnar dendrite zone. The melt flow prevented from flowing out of the weld pool, avoiding spatters and reducing hydrogen porosity by decreasing the surface area of the weld pool.

Dutra et al., (2015)	Al5083-H116 6mm; AA5183 and AA5087	Pure Argon; 15L/min	Current-106A Wire feed speed - 116.67mm/sec Welding speed-66.67mm/sec	AA5087 wire electrode has better tensile properties than AA5183 wire-electrode welded samples. Both wire-electrodes fabricated samples have similar hardness and toughness.
Leo et al., (2016)	AA5754, 3mm; thick, ER 5356	Argon; 15L/min	Current-128 to 140A Voltage-26.5 to 28V Wire Speed-0.19 to 0.20 mm/sec Welding Speed-58.33mm/sec	Untreated and post weld heat treatment GMAW welded samples have similar elongation due to coarser grain size and porosity.
Pavan Kumar et al., (2016)	Al 6061, 2mm thick; Al 6061, 1.6mm dia	Argon ; 18 L/min	Current-50A to 70A Voltage-11V to 14.2V Welding speed-6.67mm/sec to 10mm/sec	Sound welded joint obtained with pulsed CMT process with the welding current in the range of 60-70 A and the welding speed in the range of 8-10 mm/s.
Irizalp et al., (2016)	Al1050; 2mm	Argon	Current- 107A to 121A Voltage- 17.5V to 18.2V Wire feed-80mm/sec to 96.67mm/sec Welding speed-25mm/sec to 33.34mm/sec	CMT welding process was method successfully joined without any burning related defects, due to its low heat input owing to rapid cooling rate makes the suppression of amalgamation of pores in the fusion region. It increases the fusion performance and bonding line of weld metal, which eventually increasing the bending strength.
Cong et al., (2016)	AA2219 T851 19mm; ER2319 1.2 mm dia	Pure Argon; 25 L/min	Wire feed-125mm/sec Wire speed-8.33mm/sec to 16.67mm/sec	The weld melting area is effectively increased using the CMT-P process compared to that of the conventional CMT process. It is beneficial to reduce the porosity effectively with an appropriate heat input.
Liu al. (2017)	6005A 3mm; ER4043 1.2 mm dia	Pure Argon	Current- 94A Voltage- 17.8V Welding Speed-6mm/sec	The fusion region is the weakest area in the welded joint due to presence of micropores.

Wang et al., (2017)	AA6061-T6 2mm; ER4043 1.2 mm dia	Pure Argon; 15 L/min	Burn Current-40A-100A Wire feed-61.67mm/sec, 81.67mm/sec & 103.34mm/sec	The burn phase current should be low enough to contribute to a smooth short-circuiting transfer without the spattering caused by high arc pressure and over-heated droplet to fabricate CMT welded joints. With increase in speed of wire feed motion the burn phase duration decreases and increases the short-circuiting duration.
Lei et al., (2017)	AA6061-T6 1mm; ER4043 1.2 mm	Pure Argon; 15 L/min		CMT arc mode produces welds having lesser welding defects, such as minor porosity, and a partial tearing, which results in better strength of pulsed and standard arc modes of spot welding.
Ahsan et al., (2017)		Argon and CO_2 mixture (Ar/CO_2 = 9:1)	Current-200A Welding speed-13.33mm/sec	ER70S-G wire contains the higher content of the deoxidizers, whereas ER70S-6 wire has a lower amount. With ER70S-6 wire more suitable for welding with good quality welded joint.
Cornacchia et al., (2018)	Al6005; ER 4043 1mm dia	Argon; 14.5 L/min	Current-136A Voltage-17.7V Wire feed-100mm/sec	Regarding the weld defects, the porosity amount is higher for MIG than for the CMT weld. The GMAW welded joint have larger HAZ than the CMT with lower weld defects and lesser porosity.

1.3 ULTRASONIC-ASSISTED CMT WELDING

In recent years ultrasonic-assisted welding has been given more attention due to grain refinement of welded material and increased homogeneity of filler material with the base material [Zhou et al., (2018); Wang et al., (2020)]. The ultrasonic vibration treatment during welding is an alternative method for heat treatment and eliminating the post-weld heat treatment of the welded joint to lower the residual stresses for enhancement of mechanical properties [Jose et al., (2016)]. The various methods of ultrasonic probe applied by the various researchers during welding to generate ultrasonic vibrations such as the side of the substrate, top of the substrate, the filler metal, the electrode, and directly on the weld pool for achieving the best outcome (Kumar et al., (2017); Ning and Cong (2020)]. The ultrasonic vibration was introduced directly into the welding pool through filler metal for ferrite stainless steel GMAW welding [Watanabe et al., (2010)]. The tensile strength & elongation of the welded joint is improved due to more equiaxed grain formed in the welded joint compared to samples processed without vibration.

Xie, W. et al., (2020) imposed ultrasonic vibrations on the GMAW arc to fabricate Al-Zn-Mg alloy welded joint and revealed that larger HAZ and fusion region sizes were observed in vibration-assisted welded joints than in conventional GMAW welded joints. Dai, (2003) positioned the ultrasonic probe on the top surface of Al 7075-T6 alloy for GTAW welding, enhancement of hardness in the fusion region, and better weld penetration observed in ultrasonic-assisted welding in comparison to samples processed without vibrations welded samples. Zhao et al., (2020) inserted a tungsten needle with ultrasonic vibrations in the front side of the molten pool

during welding. Grain refining occurs at welded material due to the tungsten needle being located at the low-temperature zone of the molten pool material. Chen et al., (2016) reported that ultrasonic vibrations promoted heterogeneous nucleation of Al-Li alloy during GMAW welding. Yuan et al., (2016) placed an ultrasonic probe at the back of the arc to stir the weld pool during welding. The vibrations are transferred to the molten metal, which results in refined grains of welded material. Tian et al., (2018) placed an ultrasonic peening system on the Al alloy workpiece with CMT welded and found that refinement of grains with lesser porosity of welded joints.

Fattahi et al., (2020) investigated GMAW welding of Al alloy by including nanoparticles and ultrasonic vibrations under the workpiece. They found that with enhanced mechanical properties of welded joints. Ning and Cong, (2016) employed SS powder on low carbon steel to fabricate stainless steel parts by applying vibrations in the laser engineering net shaping technique (UV-LENST). The mechanical properties of the parts produced by UV-LENST are much higher than without ultrasonic vibration fabricated samples due to finer dispersion of particles, refinement of grain size, lower residual stress, and lower micro-cracks with reduction of porosity. Chen et al., (2020) introduced the ultrasonic vibration in pulsed GTAW of Q235 steel and found that refinement of grains occurred in weld seams compared to conventional GTAW. With the application of ultrasonic vibration-assisted different welding techniques are investigated by various researchers are exhibited in Table.2.4.

Table 2.4 Major conclusions on Ultrasonic assisted welding process (U-CMT)

Researcher Name	Material investigated	Welding Type (Ultrasonic-Vibration assisted)	Ultrasonic Operating parameters	Prominent Results
Zhao et al., (2020)	Ti-6Al-4V	Cold Metal Transfer	UV Frequency-20 kHz, Amplitude 100±5 μm	The ultimate tensile strength of welded joints with ultrasonic vibration shows remarkable improvement due to grain refinement.
Chen et al., (2018)	Al 1060 and Al 1003 filler wire	Pulse MIG welding (MIG-P)	UV Frequency-20 kHz	Ultrasonic assisted MIG-P welded with 120 kHz pulsed frequency sample is deepest weld penetration compared to without Ultrasonic vibrations MIG welding.
Chen et al., (2019)	Al-Cu	Pulse MIG welding (MIG-P)	UV Frequency-20 kHz	The better microstructural property, weld appearance, and deepest penetration were achieved in Ultrasonic assisted MIG-P samples in comparison with conventional MIG samples.
Fan et al., (2018)	Al 1060 & S301 filler wire	MIG welding	UV Frequency-20.1 kHz, Amplitude 30 μm	With the utilization of vibrations, the aspect ratio of the welding seam increases due to increased density of arc energy and reaching of heat in molten metal deeper easily.
Hua et al., (2017)	304 SS & FM-52M filler wire	TIG welding	UV Frequency-20 kHz	Ultrasonic vibration creates finer grains and grain fragmentation with more homogeneous filler wire in the weld.
Lan et al., (2020)	316L and L415 dissimilar	TIG welding	UV Frequency-20 kHz	The mechanical properties of the welded joint are enhanced with the ultrasonic effect owing to cavitation and acoustic streaming effect.
Li et al., (2021)	304 SS	Plasma arc welding	UV Frequency-25 kHz,	Ultrasonic vibrations increase plasma arc pressure which results in a reduction

			Amplitude- 20 µm UP-500W	in weld pool size and enhancement in weld penetration.
Kolubaev et al., (2020	A 516-55 low carbon steel	LASER welding	UV Frequency- 22 kHz Amplitude- 20 µm UP-500W	Ultrasonic vibrations enhance the welded joint hardness and marginal improvement of tensile strength & toughness. Microstructural properties of joint improve due to the change of plate-like Widmanstatten ferrite into submicron-sized equiaxed grains.
Yu et al., (2019)	AISI 321 SS	LASER welding	UV Frequency- 19.7 & 20.75 kHz, Amplitude- 20 µm; UP output- 600W, 970W & 1200W	Higher hardness and tensile strength of Ultrasonic LASER welded joined with 600W sample is obtained. Ultrasonic vibration supports for producing the grain refinement and improves the stacking fault number of welded samples.
Zhou et al., (2018)	Hastelloy C-276 & 304 SS	Laser welding	UV Frequency- 20kHz Amplitude 1.9µm and 2.7µm UP/W 0, 250 & 500	With Ultrasonic vibrations the weld depth penetration and dilution level were increased. With the higher ultrasonic power, the width of the unmixed zone near the fusion boundary has reduced due to cavitation.
Chen et al., (2020)	H40 marine steel	Ultrasonic-assisted droplet transfer controlling method	UV Frequency- 28 kHz, Amplitude- 10 µm UP-120W & 240W	This method with 240W power reduces the unstable transfer arc mode to 23% and spatter to 4%. The toughness of welded joint is increased to 20% compared with non-ultrasonic underwater welding due to grain refinement with fewer defects in a welded joint.
Gorunov et al., (2018)	Low carbon steel (09G2S)	LASER welding	UV Frequency- 20 kHz, Amplitude- 3 µm	With vibrations, the weld material strength is increased to 16% owing to a decrease in the weld pool and thick, deeper

				penetration of welded material.
Ou et al., (2021)	Inconel 718 super alloy	LASER welding	Vibration Frequency-0, 522,919,1331Hz	Vibration-assisted weld joint produces a uniform and refined microstructure owing to the evolution of equiaxed crystals and the lesser formation of carbides in the fusion region.
Jin et al., (2020)	Al 5052	LASER welding	Vibration Frequency-0, 545,956Hz Acceleration- 0, 35.5, 39, 40, 70.8 72.5m/s^2	With micro-vibration, the molten pool disperses uniformly in the weld region, which develops the refined equiaxed grains. Lower residual stresses are observed in joints with a mix of lower vibration frequency and higher vibration acceleration.
-Metal Inert Gas; TIG-Tungsten Inert Gas; UV-Ultrasonic Vibration; UP-Ultrasonic Power				

1.4 RESEARCH GAPS

- It is clear from the literature review that researchers have not explored the CMT welding process using stainless steel, high nitrogen steel, and boron steel.
- Very little research is carried out on the stainless-steel material with different process parameters such as welding current, voltage, welding speed, filler wire speed, shielding gas flow rate, and arc correction factor and compared with conventional GMAW process. Very limited work has been done with thin 304 stainless steel sheets with a CMT welding process.
- No work is carried out using 304 stainless steel with an ultrasonic-assisted CMT welding process.
- Limited work is carried out in the dissimilar steel-based CMT welding process.

1.5 RESEARCH OBJECTIVES

I. To study the effect of various CMT welding parameters on weld bead geometry of 304 stainless steel and to determine the optimal welding parameters.

II. To study the effects of various welding parameters (i.e., welding current, welding speed, contact tip to workpiece distance, and arc correction factor) on tensile properties of the CMT welded joints.

III. To determine the optimal welding parameters for welding stainless steel alloy joints using the CMT process.

IV. To characterize the joints by a metallographic study such as Optical Microscope and Field Emission Scanning Electron Microscope (FESEM).

V. To study of mechanical properties of welded metals such as micro-hardness, tensile behavior, and residual stresses.

VI. To perform a comparative analysis between CMT and ultrasonic assisted CMT welding process.

1.6 FLOW CHART FOR PRESENT WORK

The various stages of the research activity are as described below:

i. Literature survey.

ii. Selection of work material and filler metal.

iii. Experimental work.

iv. Welding parameters.

v. Testing of welded joints.

vi. Analysis of results

vii. Comparative study of CMT with U-CMT.

viii. Conclusions

The flow chart gives the summarized version of the detailed work. Fig. 2.1 shows the flow chart of the present work, which includes step by step procedure or methodology carried out during this work.

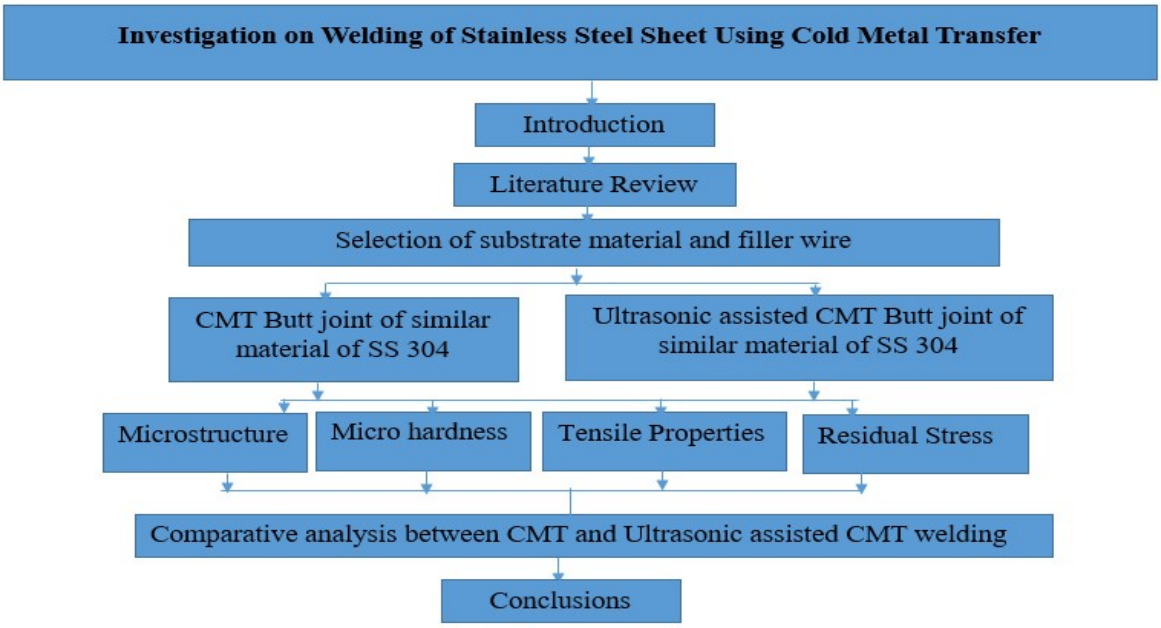

Fig. 1.1 Flow chart of present research work

1.7 SUMMARY

This chapter presents a detailed review of the joining of the CMT welding process of steels and aluminum alloys. Major conclusions are highlighted for joining similar materials and dissimilar steels in the GMAW/CMT welding process. The different methods of CMT, process parameters, and other weld material & filler wire combinations, the mechanical and microstructural studies of CMT welding stated by numerous researchers are discussed. The core inferences of this study are:

- The filler wire's retraction motion during the short-circuiting phase plays a vital role, as it helps minimize the generation of spatter, which allows producing sound welded joints.
- Optimum process parameters depend on the base material chosen, type of filler metals, environmental conditions, and shielding gases.
- The rate of wire feed, welding current, and welding speed influence heat input. As the rate of wire feed & welding current increases and travel speed decreases, the heat input increases, and vice versa.
- Ultrasonic vibration assistance during welding enhances the welding strength properties.

CHAPTER 3 : EXPERIMENTAL SETUP & PROCEDURE

3.1 MATERIAL SELECTION

3.1.1 Base Material and Filler material

The rolled sheet of AISI 304 SS of sizes 100 mm x 60 mm x 2 mm is considered as a base material. The filler wire ER 308L SS diameter of 1.2 mm is used to join. Table 3.1 displays the chemical compositions (wt. %). of AISI 304 SS base material and ER 308L SS filler wire.

Table 3. 1 Chemical compositions (wt%) of AISI 304 SS and ER 308L SS

Materials	Fe	Cr	Mn	Ni	Si	C	P	S	Mo	V	Ti
AISI304	Bal.	17.90	1.88	8.38	0.254	0.043	0.046	0.016	0.224	0.072	0.006
ER308L	Bal.	19.15	1.42	10.03	0.422	0.029	0.022	0.012	0.256	0.032	0.003

Table 3. 2 Mechanical properties of base material

Properties	σ_{UTS} (MPa)	σ_{YS} (MPa)	δ (%)	$HV_{0.5}$
AISI304	723.3	555.6	60	230
σ_{UTS} – Ultimate tensile strength (UTS); δ – Elongation; $HV_{0.5}$ – Vicker's microhardness at 500 grams load				

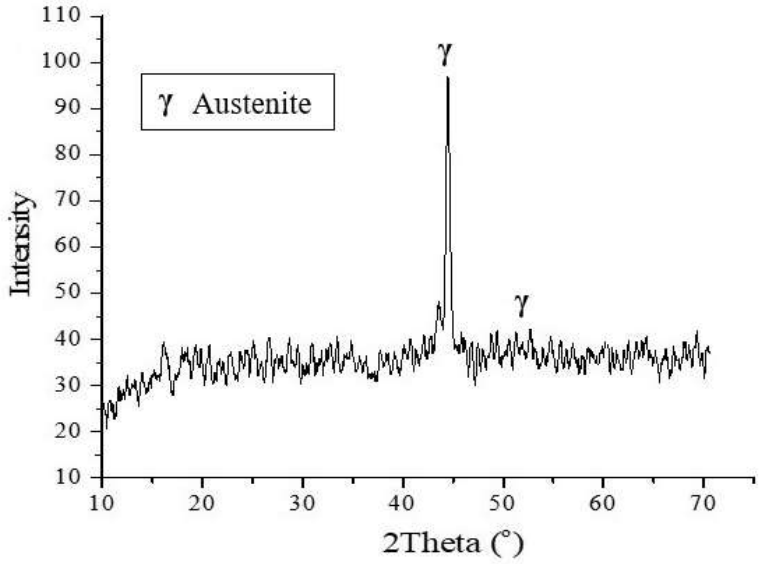

Fig. 3.1 XRD Plots of SS 304

3.2 SAMPLE PREPARATION

3.2.1 Macrostructure Characterization

The macrostructure of the weld bead dimensions is used to understand the depth of metal penetration and helps to study the weld strength and quality of the weld. Specimens were prepared by taking out the 15 x 15 mm square piece from the weld bead. Then the cross-sectional surface of the weld bead was polished with the help of the emery paper of grades 100, 320, 400, 600, 800, 1000, 1200, 1500, 1800, and 2000. Dry and wet polishing is needed to explore the macrostructure of the weld bead.

3.2.2 Microstructural characterization

The cross-section of welded sample's microstructure was observed with the help of an optical microscope (Make OLYMPUS). The cross-section specimens were polished with 320, 400, 600, 800, 1000, 1200, 1500, 1800, and 2000 grits of emery sheet. Then samples

are polished with velvet cloth polishing using three grades of I, II, and Alumina suspension. Then the polished surface was etched with the composition of 30 ml HCl + 120 ml distilled water + 10 g $FeCl_3$ [Singh et al., (2018)] for 20 seconds. The samples are washed with distilled water and then dried with a drier to remove the carbon deposits. The microscopic study was carried out using the optical microscope, and the grain size analysis was carried out with image J software.

3.2.3 Microhardness

Vicker's microhardness tester (STRUERS) was used to estimate the hardness of the fusion region and HAZ of the weld bead samples with an applied load of 500 gm for 20 s as per ASTM E384-99 standard. Before testing, the hardness sample was mounted with bakelite powder in a mounting press to facilitate preparation and testing. Then the specimens were polished up to 1200 grit fine emery paper and by alumina polishing. A diamond pyramid indenter was used to make an indentation. Three indentations were carried out laterally for experimental purposes, and the average of three hardness values was taken for all the samples.

3.2.4 Tensile Testing

The tensile test at a cross-head speed of 1 mm/min was performed by UTM (Tinius Olsen H50KS). The specimens were prepared as per ASTM: E8/ E8M-011 standards with a gauge length of 25 mm, as shown in Fig. 3.2. The Ultimate Tensile Strength (UTS) and percentage of elongation were recorded. The average of three sample testing data was reported.

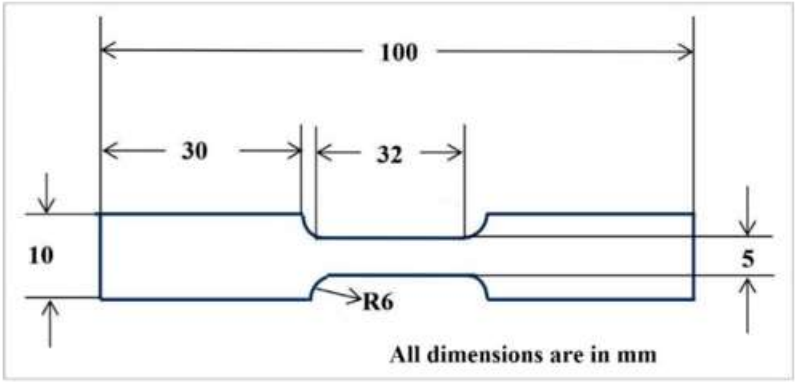

Fig. 3.2 Tensile test specimen dimensions as per ASTM E8

3.2.5 Residual Stress

Residual stress specimens are extracted from the middle of welded samples at the size of 10 mm x 10 mm by wire EDM machine. Before the testing, the cross-sectional surface of pieces is polished with different grades of emery (180, 320, 400, 600, 800, 1000, 1200, 1500, 2000, and 2500) sheets. Specimens were prepared by taking out the 15 x 15 mm square piece from the weld bead.

3.3 EXPERIMENTAL MACHINES

3.3.1 CMT Machine

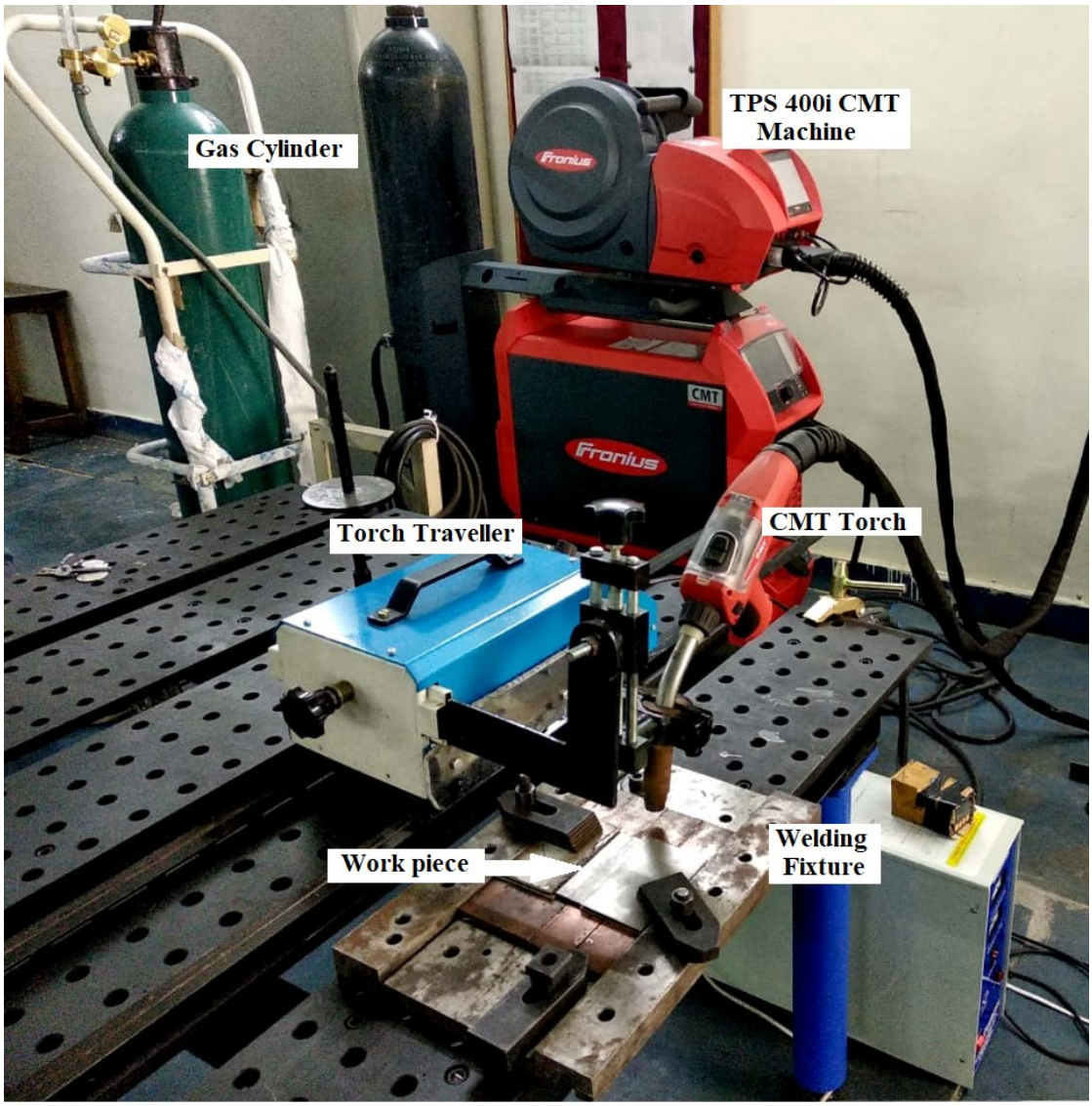

Fig. 3. 3 TPS400i CMT welding machine

Table 3. 3 CMT welding machine specifications (TPS 400i)

Mains voltage	3x 460V
Mains range	323-529 Vac
Fuse Protection	35A slow blow
Mains tolerance	+/-15%
MIG current range	3-400A
MIG voltage range	14.2-34.0
Duty cycle 104°F (40°C)	400A @ 40%
	360A @ 60%
	320A @ 100%
Degree of protection	IP 23
Dimensions (LxWxHmm)	706x300x510
Weight	32.5kg

3.3.2 Tensile Testing Machine

Fig. 3.4 Tensile machine (Model: Tinius Olsen H50KS)

Table 3. 4 Tensile Testing Machine specifications

Capacity	kN/Kg	50/5000
Clearance between columns	mm	405
Load cells	-	Rapid change, low profile Z type load cells with digital encoading for automatic recogonition.
Maximum cross head travel	mm	1100
Testing speed range	mm/min	0.001-500
Capacity at maximum speed	kN	25
Maximum speed at capacity	mm/min	250
Jog speed	mm/min	0.001-500
Return speed	mm/min	0.001-500
Dimensions (H x W x D)	mm	1613 x 720 x 500
Weight	Kg	140

3.3.3 Microhardness Machine

Fig. 3. 5 Microhardness testing machine (Struers Duramin-40)

Table 3. 5 Microhardness testing machine specifications

Model	Duramin-40 M1
Loads and Applications	
Load Range (Main Loads)	10 gf – 10 kgf
Vickers Capability	Yes
Knoop Capabiblity	Yes
Brinell Capability	Yes
Stages and Turrets	
XY-stage	Manual
XY-stage or anvil size (mm)	90 x 90
XY-stage stroke, max (mm)	25 x 25
Vertical capacity	172
Throat depth (mm)	170
Motorized Z-axis	Yes
Motorized turret	Yes
Turret positions	6
Anti-collision protection	Yes
Machine weight	101 kg
Camera and Optics	
Evaluation camera resolution	18 MP
Auto illumination	Yes
Stage illumination	Yes
Laser or LED guider	Yes
Interfaces and Connectivity	
Operation	Embedded Windows 10 PC with 15 inch touch screen.
Communication Ports	HDMI, VGA, RJ45, WLAN, USB, RS232

3.3.4 Optical Microscopy

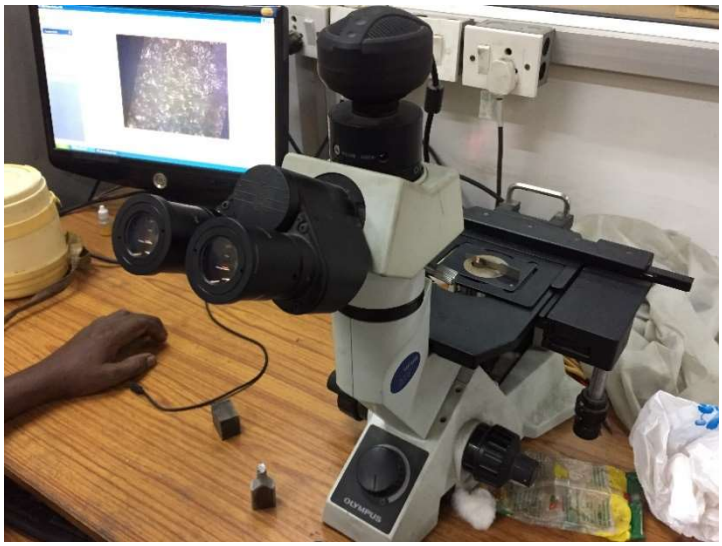

Fig. 3. 6 Olympus GX41 compact inverted metallurgical microscope

Table 3. 6 Optical Microscope specifications (Make:Olympus GX41)

Optical System			UIS2 Optical System (Infinity-corrected)
Microscope Frame	Observation Method		BF/KPO
	Reflected/Transmitted		Reflected
	Illumination System	Reflected light	30W Halogen or Fiber Light Guide(Light source:100 W)
	Focus	Motorized/Manual	Manual Revolving Nosepiece Up/Down Movement (Stage Stationary Type)
		Stroke	9 mm
		Resolution/Fine adjustment sensitivity	Fine Stroke per Rotation 0.2 mm
	Revolving Nosepiece	Manual type	Quadruple for BF
Stage	Stroke		120(X)x78(Y) mm
Observation Tube	Standard Field (Field number 18)	Inverted Image	Tilting Binocular Observation Tube
	Standard Field (Field number 20)	Inverted Image	Binocular/Trinocular/Tilting Binocular Observation Tube
	Wide Field (Field number 22)	Inverted Image	Binocular/Trinocular/Tilting Binocular Observation Tube
Dimensions			236(W) x 624(D) x 407(H) mm
Weight			10kg

3.3.5 Field Emission Scanning Electron Microscope

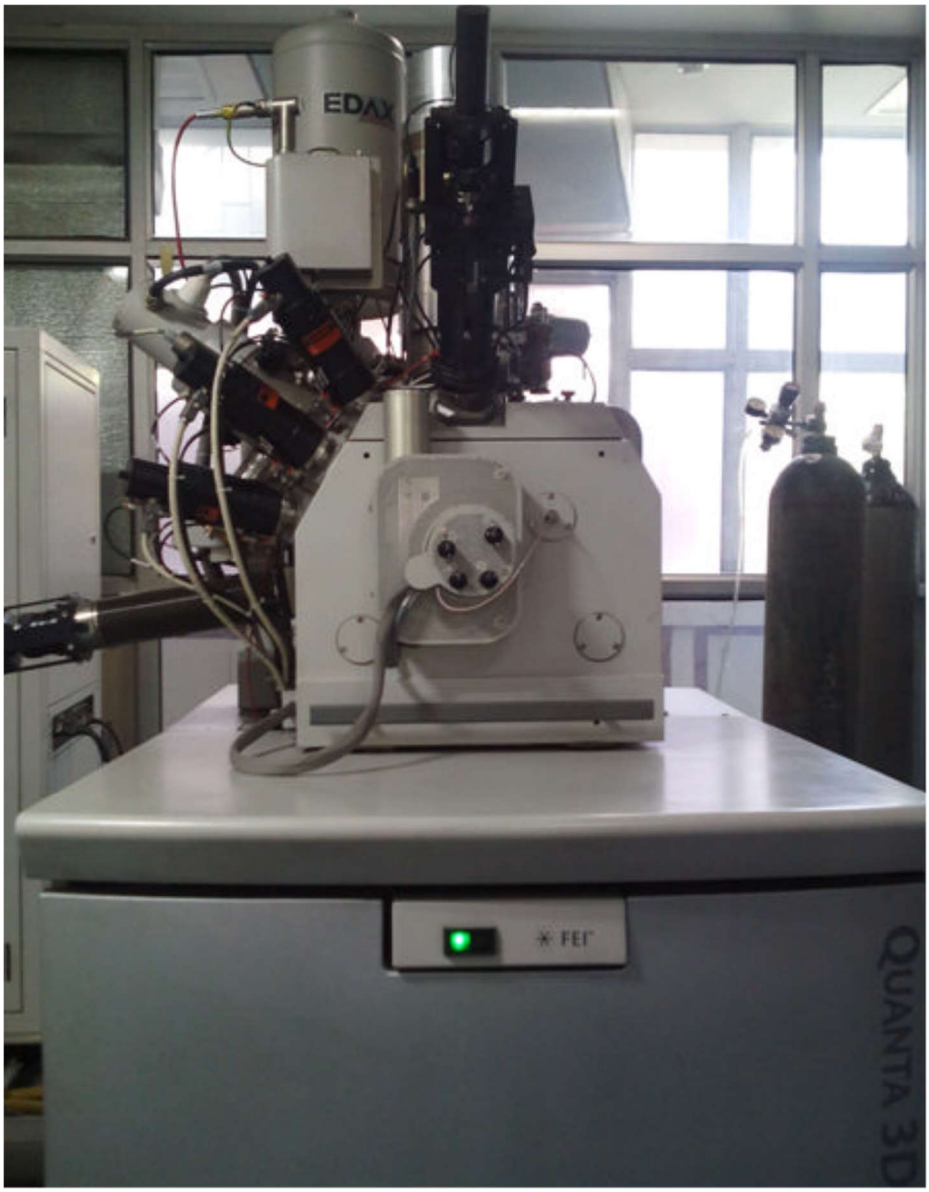

Fig. 3.7 Field Emission Gun Scanning Electron Microscope (FEG-SEM) (Model: FEI QUANTA 3D FEG)

Table 3. 7 FESEM specification

Electron optics	High-resolution FESEM column optimized for high brightness/high current
Ion optics	Magnum ion column with Ga liquid metal ion source with a lifetime of 1500 hours
Electron beam resolution	- 1.2 nm @ 30 kV @ high vacuum mode - 1.5 nm @ 30 kV @ ESEM mode - 1.5 nm @ 3 kV @ low vacuum mode
Ion beam resolution	10 nm @ 30 kV @ 1pA
Accelerating voltage	200V to 30 kV for electron beam imaging and 5 to 30kV for ion beam imaging
Detectors	Everhardt-Thornley SED, Low-vacuum SED, Gaseous SED, IR-CCD, EDS detector and Gaseous BSED
Specimen stage	4-axis motorized eucentric goniometer stage X = 50 mm, Y = 50 mm, T = -15 +75°(manual), Z = 50 mm (25 mm motorized), rotation = 360° continuous

3.3.6 X-Ray Diffraction

Fig. 3. 8 X-Ray diffraction (Model: BRUKER D8 ADVANCED)

Table 3. 8 Specification of XRD machine

X-ray	
Source	2.2 kW Cu anode long fine focus ceramic X-ray tube
Running Condition	40 kV and 40 mA
X-ray Beam Shaping Optics	
Beam [Cu-$K_{\alpha 1}$]	Collimated, compressed and frequency filtered by a Göbel mirror and V-Groove
Collimated beam dimensions	0.3 mm by 11 mm
Göbel mirror	60 mm multilayer X-ray mirror on a high precision parabolic surface
Goniometer	
Maximum and minimum measurement circle diameter	250 mm & 100 mm
Smallest angular step size	0.0001°
Reproducibility	+/- 0.0001°
Maximum rotational speed	1500 °/min
Angular range (Theta)	-5° to 40°
Angular range (2Theta)	-10° to 60°
Reflectometry Sample Stage	
Samples size	200 mm in diameter and 50 mm thick
Detector	
Maximum count rate	2 x 10^6 s^{-1} (although it should not be exposed to in excess of 5 x $10^5 s^{-1}$ for periods longer than about 1 second)
Detector electronics count rate	3 x 10^7 s^{-1}

3.3.7 Residual Stress Measurement Machine

Residual stresses of the welded joints of various regions were measured by µ-X360n Pulstec High-Resolution Full 2D X-ray Diffraction (HR-XRD) machine. A standard Cr x-ray tube (30 kV and 1 mA) with a collimator size of 1 mm and measuring conditions are included in the device specification. This equipment works on the Cosa method, and it obtaining a full Debye–Scherrer ring to collect the entire diffraction through a 2D detector.

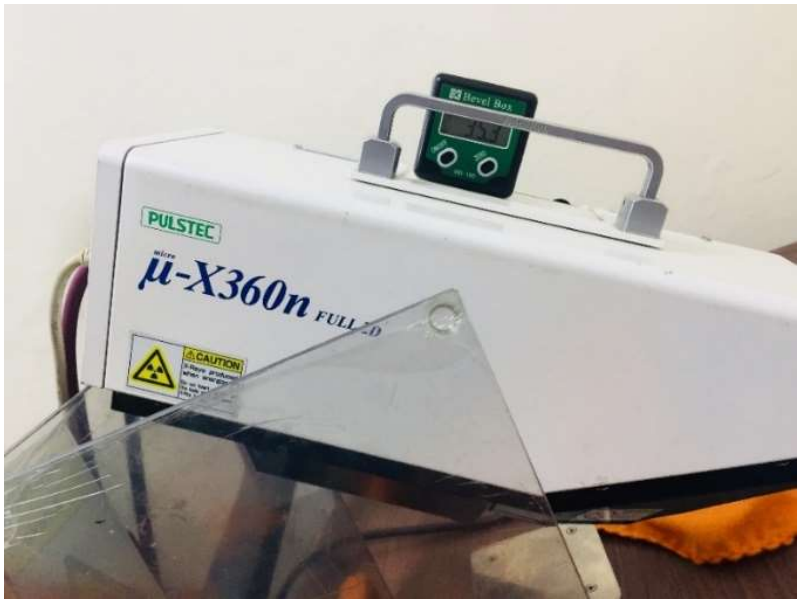

Fig. 3.9 Pulstec µ-X360n Full 2D High-Resolution X-ray Diffraction (HR-XRD) machine

Table 3. 9 Residual stress machine specifications

X-ray tube	30 kV & 1 mA (Safety & Ecology)
Collimator size	φ 1 mm (φ 0.04 inch)
X-ray detector	Full 2 D (visual analysis)
Precision mech.	Not necessary
2D Full data of Debye-Scherrer ring	Max. 500 points
Cos α line Data	Max. 125 points
Permissible range	±5 mm (easy setting)
Measurement time	90 sec.
Portable	Air cooling, Goniometer not required
Sensor unit weight	4 kg (8.8 lbs) (Z height stage)
Power supply unit weight	6 kg (13.2 lbs)

3.4 OPTIMIZATION OF CMT WELD PROCESS PARAMETERS

3.4.1 Process Parameters

Welding Current: In GMAW/CMT welding, the generation of heat input mainly depends upon the welding current [Selvi et al., (2017)]. The welding current influences the size of weld width, dilution, and depth of penetration of welded joint, as a result of good microstructural and mechanical properties of welding joint. The welding current value is chosen on the basis of the thickness of the base material. Appropriate welding current requires fabricating sound welding joint without lack of penetration. In this research, the work current is chosen as one of the process parameters.

Welding speed: Welding speed is a vital welding parameter for generating heat input during welding [Dhobale et al. (2015)]. Higher welding speed produces lower heat input as a result of improper penetration in welded joints. Too much lower welding speed creates high heat input, which may result in excess melting of the base material. The welding speed is the total time the welding torch takes to complete the welding.

Contact tip to work distance (CTWD): The distance between the base material to filler wire tip is the CTWD. With increase or decrease in CTWD value affects the welding current. Suitable CTWD should be maintained for better welding results.

Voltage: Arc voltage is also directly proportional to the heat input. In this study welding current is taken as an independent welding parameter and the voltage depends upon the welding current. When changing the welding current, the machine automatically adjusts the voltage value.

Gas flow rate: Shielding gas protects the molten weld pool from the formation of ill effects from harmful atmospheric gases such as hydrogen, nitrogen, oxygen, etc. Gas flow rate influences the quality of weld bead and penetration. In this work, constant gas flow is maintained.

Pulse Dynamic Correction factor: This parameter dispenses the droplet detachment at a slower rate or uniform energy level from the filler wire. The pulse dynamic correction factor controls the average current and influences the direct current [Rajeev et al., (2019)].

There are three arc correction factor levels: -10, 0, and +10. When the detachment of droplet force is required for the lower side (-10), no increase or decrease in the separation of droplet force (0) for the higher side (-10) is fixed in the machine.

Wire feed rate is defined as the rate at which filler wire moves towards the weld bead. Wire feed rate directly affects the formation of weld width, HAZ, and intermetallic layer thickness. [Mehrani et al., (2016)].

3.4.2 Taguchi design

From the literature review and preliminary trials, the vital welding parameters such as welding current, travel speed, and contact tip to work distance (CTWD) were fixed to study the CMT weld bead experiments. Other parameters like shielding gas flow rate, arc correction factor, and wire feed rate are kept constant. Based on Taguchi's L9 orthogonal array design matrix, nine parametric combinations were designed using three levels of welding current, welding speed, and CTWD. Table 3.10 shows the values of three different welding parameters and their levels. Table 3.11 shows the design matrix and the actual values of welding parameters for weld bead experiments. Minitab software is used to check the optimal parameters for finding larger, better responses.

Table 3. 10 Design of experiments for CMT weld bead.

Welding process parameters	**Units**	**Symbols**	**Levels**		
			-1	**0**	**1**
Current	A	I	85	90	95
Welding speed	mm/sec	S	4	6	8
CTWD	mm	L	3	5	7

3.5 EXPERIMENTAL PROCEDURE

3.5.1 CMT weld bead

The rolled sheet of AISI 304 SS of 100 mm x 60 mm x 2 mm is considered a base material. The filler wire ER 308L SS diameter of 1.2 mm is used to join. A large number of preliminary experiments were carried out to find the upper and lower limits of welding parameters. The selected welding parameters & their levels are presented in Table 3.10 as per Taguchi L9 orthogonal array. With the set parameters of current, welding speed, and CTWD, the machine automatically decides the voltage in the range of 10V-20.8V. Pure argon gas (99.99%) of 14 L/min flow rate was considered for all the experiments. The CMT welding machine setup is shown in Fig. 3.10. The prepared weld bead samples as per the design matrix is shown in Fig. 3.11.

Table 3. 11 Taguchi design matrix for CMT weld bead

S.No.	Process Parameters		
	Current A	Welding Speed mm/sec	CTWD mm
1	85	4	3
2	85	6	5
3	85	8	7
4	90	4	5
5	90	6	7
6	90	8	3
7	95	4	7
8	95	6	3
9	95	8	5

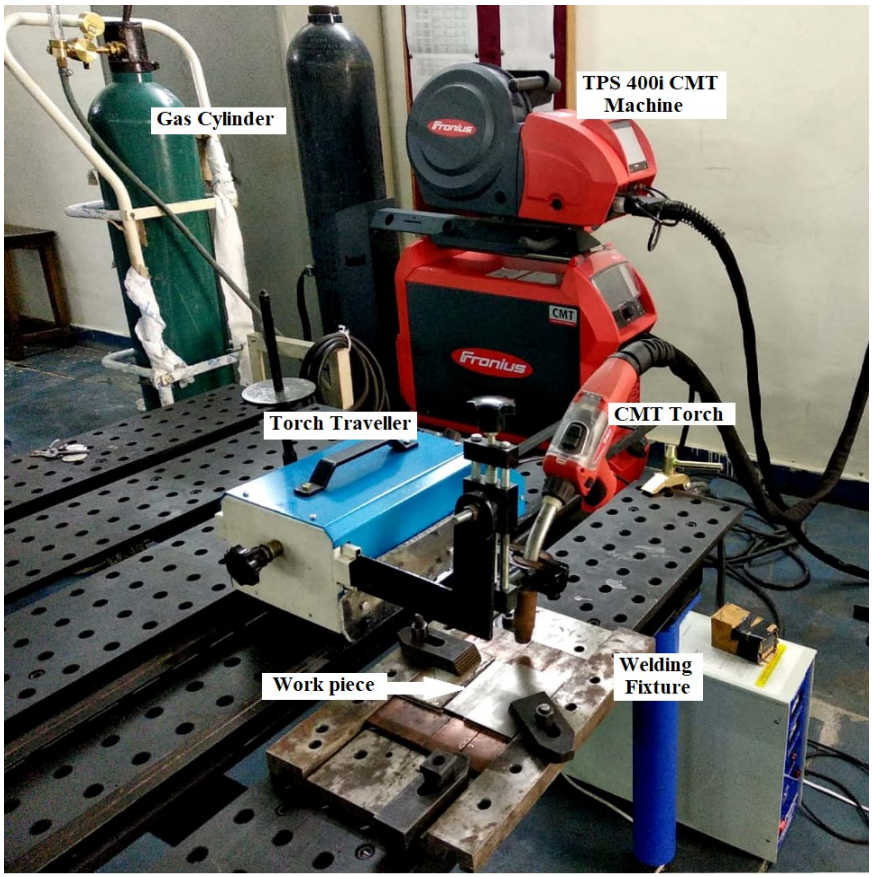

Fig. 3.10 CMT welding machine setup

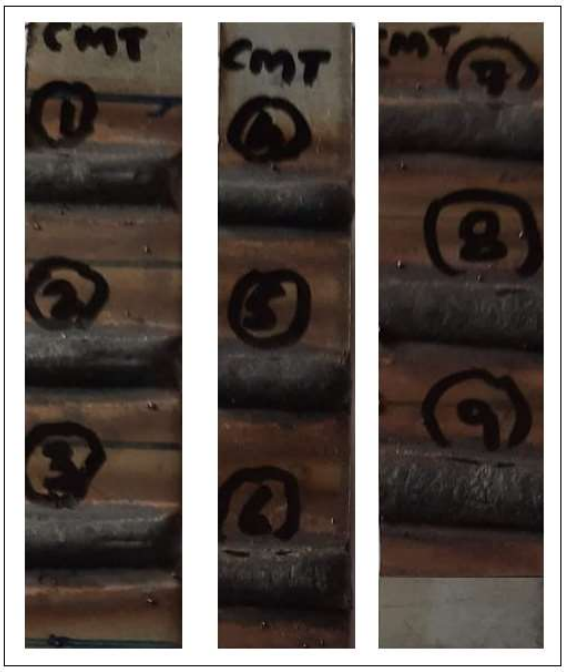

Fig. 3.11 CMT weld bead samples as per design matrix

3.5.2 CMT Butt Weld Joint

Experimental trials were carried out on SS304 sheets of dimension 100mm × 60mm × 2mm. SS304L electrode wire of 1.2 mm diameter was used as filler wire. The samples were welded by the CMT process using a TPS 400i CMT welding machine. Before welding, the samples were cleaned with acetone to eliminate the dirt, oxide film, paints, etc. The samples were clamped on the welding fixtures tightly to avoid bending the sheets during the welding. A shielding gas with pure argon (99.99%) was used for conducting all experiments. The selected welding parameters & their levels are presented in Table 3.12 as per the Box-Behnken design matrix given in Table 3.13 for CMT butt weld joints. With the set input weld parameters such as welding current, welding speed, and fire feed rate, the machine automatically fixes the voltage in the range of 10V-20.8V.

Table 3. 12 Welding parameters and their levels for CMT Butt Joints

Parameter	Notation	Levels		
		-1	0	+1
Welding Current (A)	I	85	90	95
Welding Speed (mm/s)	S	4	6	8
Contact tip to workpiece distance (mm)	D	3	5	7
Arc Correction factor	C	-10	0	10

Fig. 3.12 CMT welded samples as per design matrix

3.5.3 Ultrasonic Assisted CMT (U-CMT) Butt Joint

Fig. 3.13 (a) shows the ultrasonic-assisted CMT welding setup. The ultrasonic probe is clamped on the fixture to touch the middle of the two workpieces from the width side, as shown in Fig 3.13 (b). Ultrasonic vibrations of 20 kHz constant frequency and vibration amplitude in the range of 11-99 μm are generated by the ultrasonic generator. For comparison between CMT and ultrasonic assisted CMT welding process, the selected welding parameters were chosen in this study. The selected welding parameters are exhibited in Table. 3.13. The Ultrasonic assisted CMT and without vibration welded samples are displayed in Fig. 3.14.

Table 3. 13 Experimental welding parameters for different welding process

EXP NO	Weld Type	Current (A)	Welding Speed (mm/sec)	Contact to work piece distance (mm)	Ultrasonic Vibrational amplitude (µm)
S1	U-CMT	85	4	7	50
S2	U-CMT	85	4	7	99
S3	U-CMT	90	4	7	50
S4	U-CMT	90	4	7	99
S5	U-CMT	95	4	7	50
S6	U-CMT	95	4	7	99
S7	CMT	85	4	7	--
S8	CMT	90	4	7	--
S9	CMT	95	4	7	--

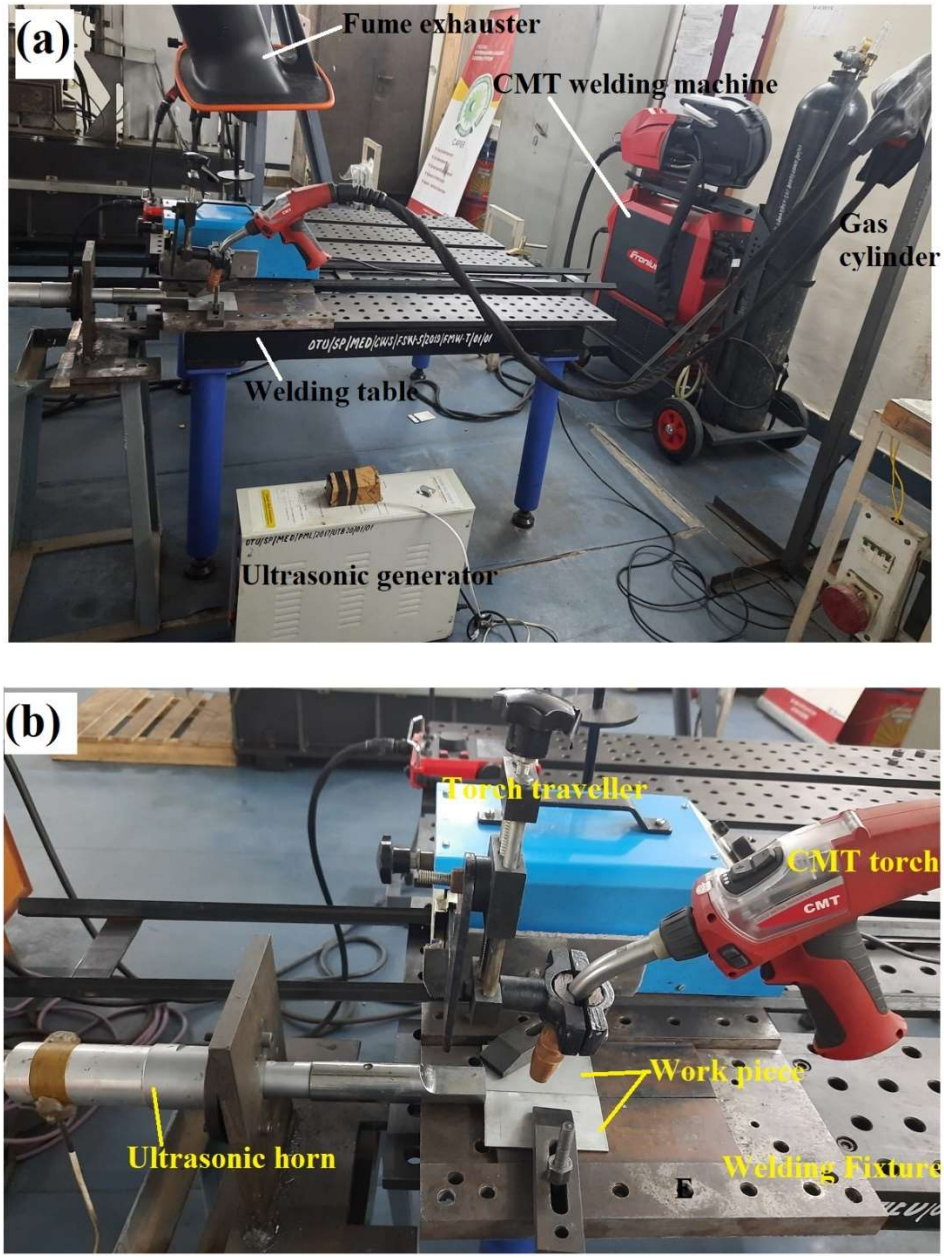

Fig. 3.13 (a) Ultrasonic assisted CMT welding experimental setup (b) Enlarged view

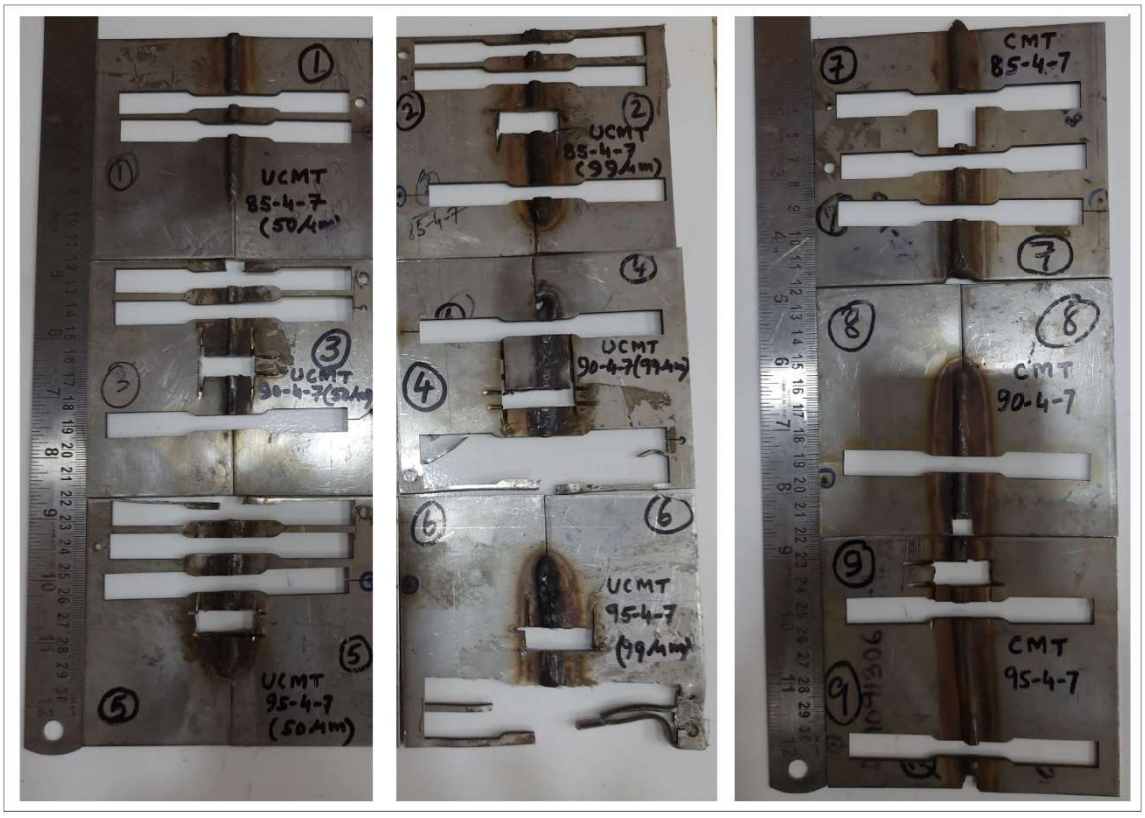

Fig. 3.14 Ultrasonic assisted CMT welded samples

3.6 SUMMARY

AISI 304 stainless steel and ER304L were chosen as base material and filler wire. Sample preparation for various tests such as macrostructure and microstructural characterization, microhardness, tensile and residual tests were described in detail. Different machines involved in welding and microstructural and mechanical characterization were discussed. All specimens were prepared as per ASTM standards. Experimental methods for weld bead-on-plate, CMT Butt weld joining, and Ultrasonic assisted welding (U-CMT) are explained briefly. Optimization for weld bead-on-plate was carried out using Taguchi L9 orthogonal array. For CMT welding optimization Box-Behnken design matrix was used to find the maximum tensile strength of the welded joint. Lastly, U-CMT samples were prepared and compared with CMT welded samples.

CHAPTER 4 : RESULTS AND DISCUSSIONS

4.1 OPTIMIZATION OF PARAMETERS FOR CMT WELD BEAD

4.11 Introduction

Weld bead analysis is essential to understand before welding to find the weld penetration and dilution, which assist in evaluating the overall quality of the welding. Stronger weld strength with economic weld joints requires deeper penetration, lower HAZ, and less consumption of filler material. A Schematic diagram of the weld bead is shown in Fig.4.1.

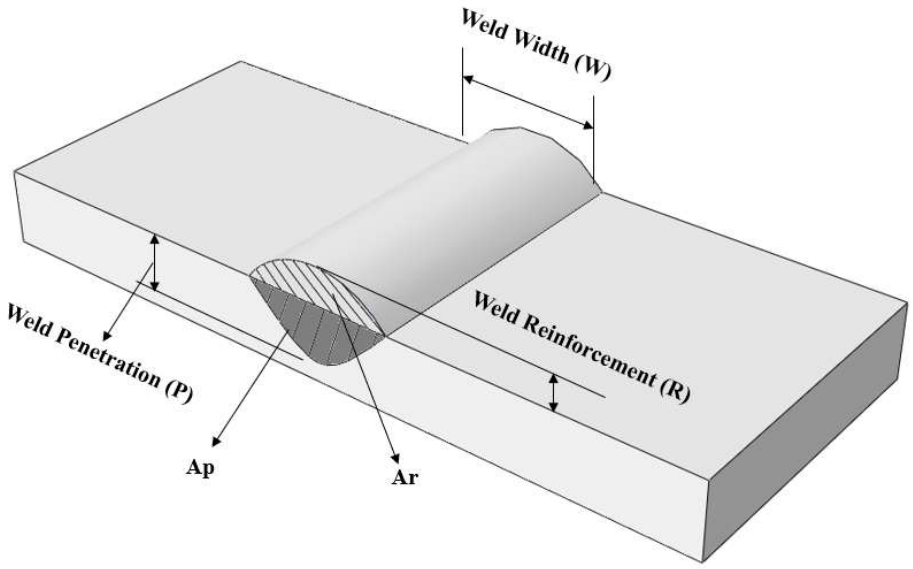

Fig. 4.1 Weld bead diagram

4.12 Opmization of welding parameter

Many preliminary weld bead trials were performed to fix the upper and lower limits of welding parameters. As per Taguchi L9 orthogonal array, the selected welding parameters and their levels are exhibited in Table 4.1. The machine automatically decides the voltage with the set welding parameters of current and speed. The voltage ranges from 10V to

20.8 V. Shielding gas of pure argon gas (99.99%) at a flow rate of 14L/min was selected at 14 L/min for all experiments.

Table 4. 1 Welding parameters and their response variables with S/N ratios

S.No	Welding current	Welding speed	CTWD	Micro hardness	Dilution	Heat Input	S/N ratio Harness	S/N ratio Dilution	S/N ratio Heat Input
	I (A)	S (mm/sec)	D (mm)	($HV_{0.5}$)	(%)	Q (J/mm)			
S1	85	4	3	153.8	33.91	178.50	43.7391	30.6066	45.0328
S2	85	6	5	144.5	24.21	119.00	43.1974	27.6799	41.5109
S3	85	8	7	142.2	33.40	89.25	43.0580	30.4749	39.0122
S4	90	4	5	173.1	55.03	190.80	44.7659	34.8120	45.6116
S5	90	6	7	155.4	48.47	127.20	43.8290	33.7095	42.0897
S6	90	8	3	161.8	49.75	95.40	44.1796	33.9359	39.5910
S7	95	4	7	180.7	64.41	205.20	45.1392	36.1791	46.2435
S8	95	6	3	168.5	52.40	136.80	44.5320	34.3866	42.7217
S9	95	8	5	175.4	56.76	102.60	44.8806	35.0808	40.2229

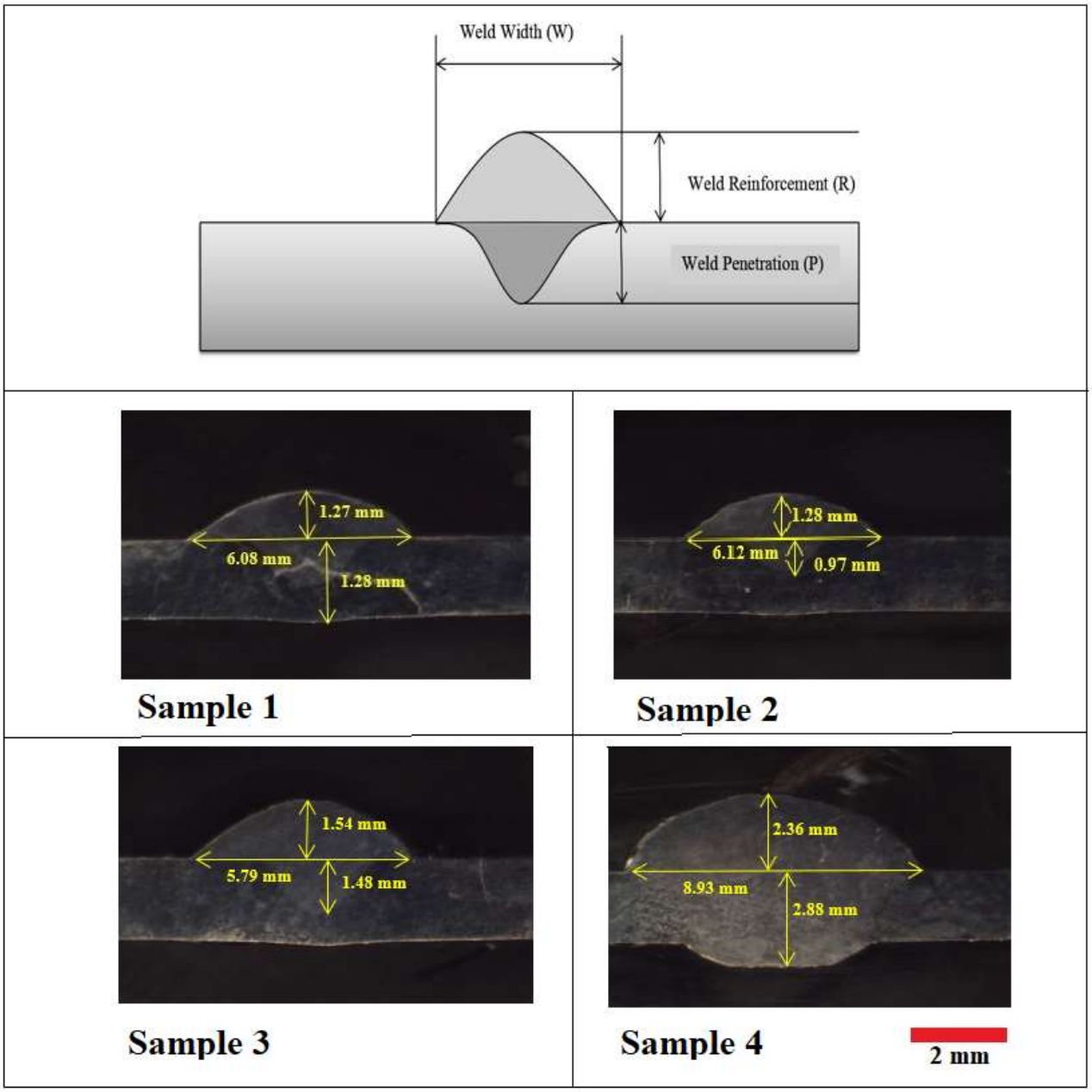

Fig. 4.2 Macro-images of CMT weld bead samples S1 to S4

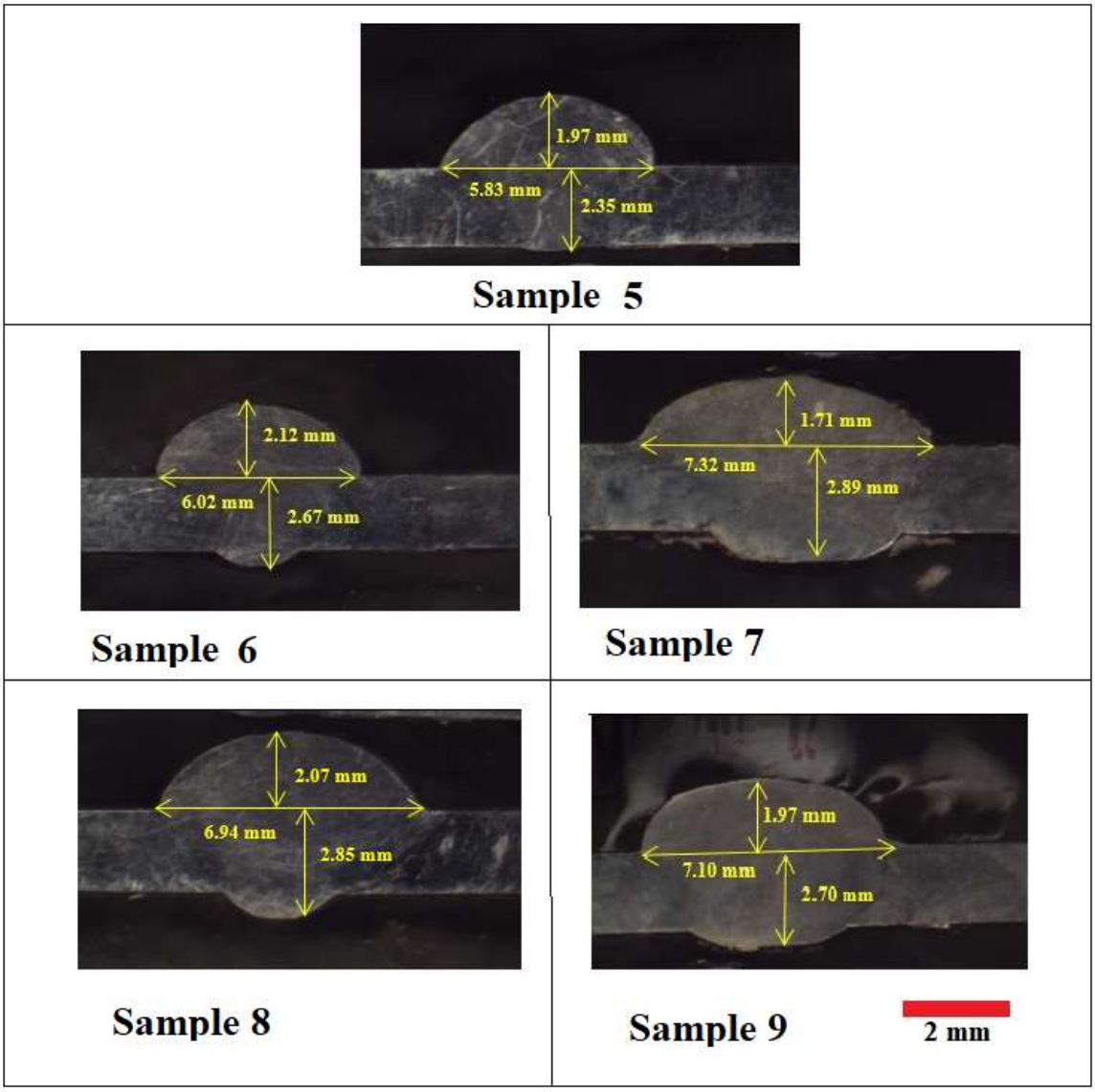

Fig. 4.3 Macro-images of CMT weld bead samples S5 to S9

The weld bead experiments were performed per the Taguchi L9 design matrix, and the cross-section macro images of weld bead samples are shown in Fig 4.2 and Fig. 4.3. The response variables, Microhardness (HV), Dilution (%), and Heat input (J/mm), were estimated, which is presented in Table 4.1. The estimation of dilution (%) of the weld bead is given in equation (4.1).

Dilution = Ap/ (Ap + Ar)……..(4.1)

Whereas, Ap = Area of weld penetration Ar = Area of weld reinforcement [koli et al., 2019]

The heat input is calculated using the following equation (4.2) [Hsieh et al (2013)].

Heat Input (Q) =

$$\eta\frac{V\ X\ I}{S}\text{……..…..(4.2)}$$

Where efficiency of the welding (η); voltage (V); current (I); welding speed (S). The welding efficiency in this study has been assumed as 80% [koli et al., (2020)]. The S/N ratios of experiments were estimated using equation 4.3, and the values are exhibited in Table 4.1. In the response table, the higher value of the S/N ratio represents the most significant input welding parameter to obtain maximum responses.

The S/N ratios were calculated using the following equation.

$$\left(\frac{S}{N}\right)s = -10 * \log(\frac{1}{n}\sum_{i=1}^{n} 1/yi\ ^2)\text{……..(4.3)}$$

In this study highest S/N ratios show the appreciable response parameters for good weld bead on the plate. S/N ratios impact the noise on the response variables. The most significant S/N ratios for microhardness of 45.1392, dilution of 36.1791, and heat input of 46.2435 were observed in this study. The most influencing welding input parameters are welding current of 95A, welding speed of 4mm/sec, and CTWD of 7 mm for all response variables.

The response tables for means of microhardness, dilution, and heat input are exhibited in Tables 4.2 to 4.4. The estimated delta value of means for the response variable of microhardness is welding current (28), welding speed (13.1), and CTWD (4.9). The

highest delta value represents the most influencing input parameter, welding current, followed by welding speed and CTWD. The lowest delta value represents for least influencing input parameter. The contribution percentage of input welding parameters are 60.86 % for welding current, 28.47% for welding speed, and 10.65 % for CTWD.

The delta value of means for the response variable of dilution is welding current (27.35), welding speed (9.42), and CTWD (3.43). A similar trend of input influencing parameters was observed for the higher dilution value. However, the delta value of means order is changing for the response variable of heat input. The delta value of means for the response variable of heat input is welding current (19.28), welding speed (95.75), and CTWD (3.65). The highest delta value is observed in welding speed, followed by welding current and CTWD. The contribution percentage input welding parameters are 16.24 % for welding current, 80.67% for welding speed, and 3.07 % for CTWD. The welding speed is a more responsible influencing factor for generating heat input. With an increase in welding speed at a constant current, lower heat input occurs, resulting in a lower depth of penetration and a lower dilution percentage. On the other hand, with a decrease in welding speed, higher penetration depth occurs as the dilution percentage increases. The response tables for S/N ratios of microhardness, dilution, and heat input are exhibited in Tables 4.5 to 4.7. Similar delta values were also observed for input variables in the S/N ratio Table 4.5 to 4.7. Fig. 4.4 to 4.6 shows the main effect plots of input welding parameters to response parameters created by Minitab software.

Table 4. 2 Response table for mean Microhardness

Level	Welding current	Welding Speed	CTWD
1	146.8	169.2	161.4
2	163.4	156.1	164.3
3	174.9	159.8	159.4
Delta	28.0	13.1	4.9
Rank	1	2	3

Table 4. 3 Response table for mean Dilution

Level	Welding current	Welding Speed	CTWD
1	30.51	51.12	45.35
2	51.08	41.69	45.33
3	57.86	46.64	48.76
Delta	27.35	9.42	3.43
Rank	1	2	3

Table 4. 4 Response table for mean Heat Input

Level	Welding current	Welding Speed	CTWD
1	128.92	191.50	136.90
2	137.80	127.67	137.47
3	148.20	95.75	140.55
Delta	19.28	95.75	3.65
Rank	2	1	3

Table 4. 5 Response table for S/N ratios for Microhardness

Level	Welding current	Welding Speed	CTWD
1	43.33	44.55	44.15
2	44.26	43.85	44.28
3	44.85	44.04	44.01
Delta	1.52	0.70	0.27
Rank	1	2	3

Table 4. 6 Response table for S/N ratios for Dilution

Level	Welding current	Welding Speed	CTWD
1	29.59	33.87	32.98
2	34.15	31.93	32.52
3	35.22	33.16	33.45
Delta	5.63	1.94	0.93
Rank	1	2	3

Table 4. 7 Response table for S/N ratios for Heat Input

Level	Welding current	Welding Speed	CTWD
1	41.85	45.63	42.45
2	42.43	42.11	42.45
3	43.06	39.61	42.45
Delta	1.21	6.02	0.00
Rank	2	1	3

The main effect plots give the importance of individual input parameters and the independent variation of the responses. In Fig 4.4, the welding current has a sharp curve compared to welding speed and CTWD parameters, which shows the maximum effect. Higher the welding current increases the heat input, resulting in increased weld material dilution. Higher hardness occurs with a rise in welding current and reduced welding speed with suitable CTWD. The S/N ratio main effect graphs are also used for finding the optimal welding parameters. It is also used to identify and measure the effect of outside factors or noise factors. Fig. 4.7 to 4.9 shows the S/N main effect graphs of the various response factors. From the plots, the best quality weld on the bead is obtained at 95A welding current, 4 mm/sec welding speed, and 7mm CTWD.

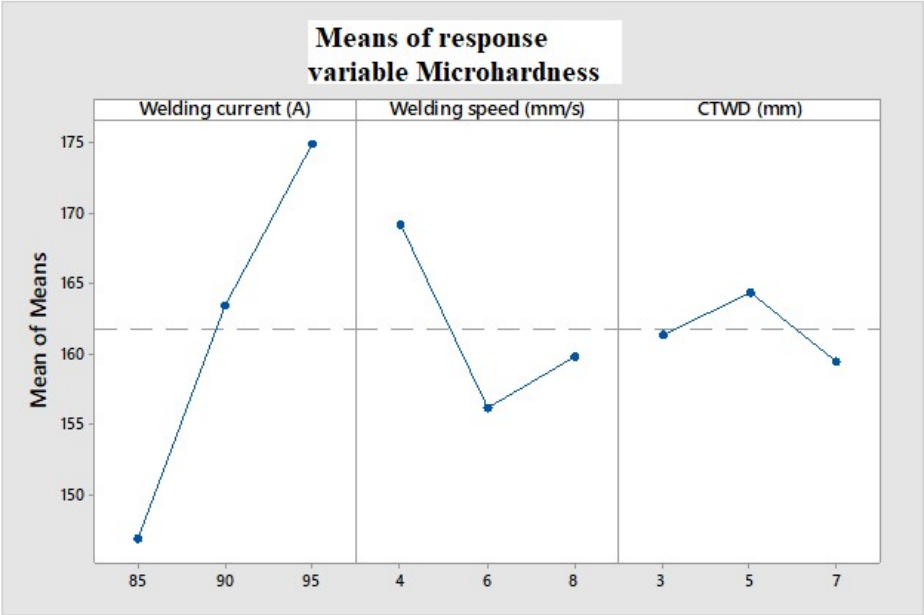

Fig. 4.4 Control parameters vs Microhardness: Mean Microhardness (HV) at different welding parameters

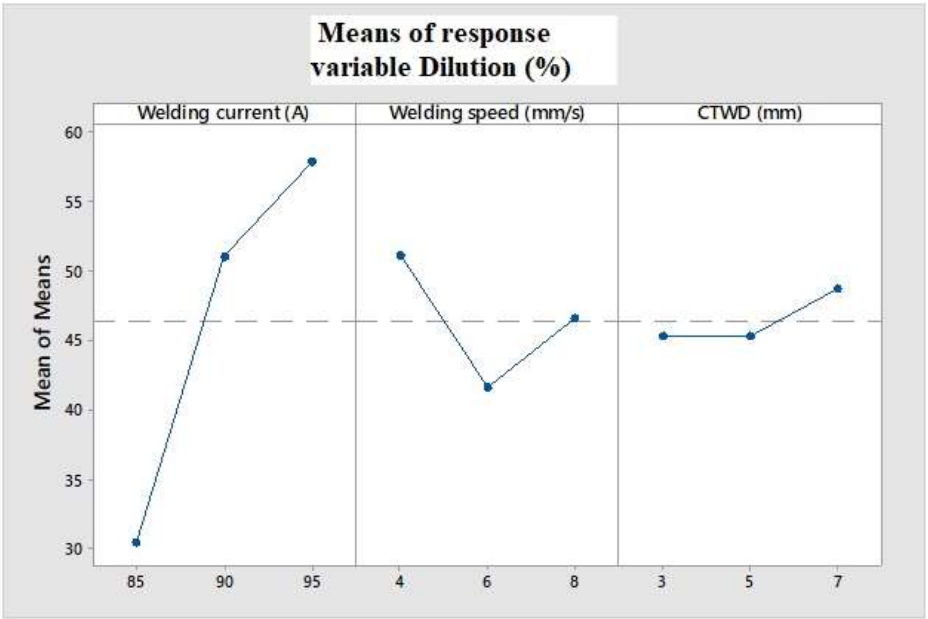

Fig. 4.5 Control parameters vs Dilution: Mean Dilution (%) at different welding parameters

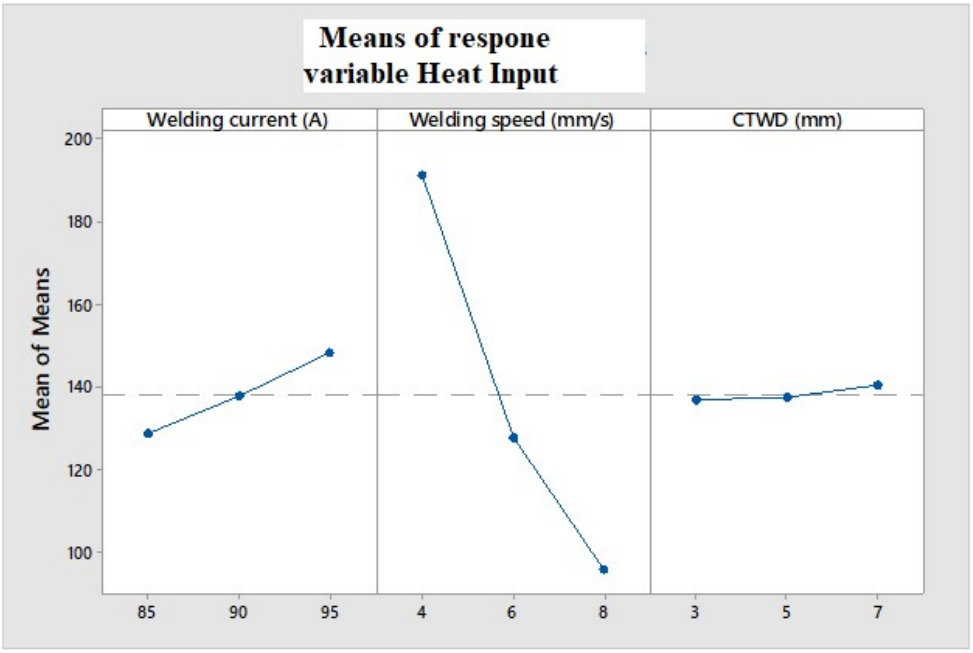

Fig. 4.6 Control parameters vs Heat Input: Mean Heat Input (J/mm) at different welding parameters

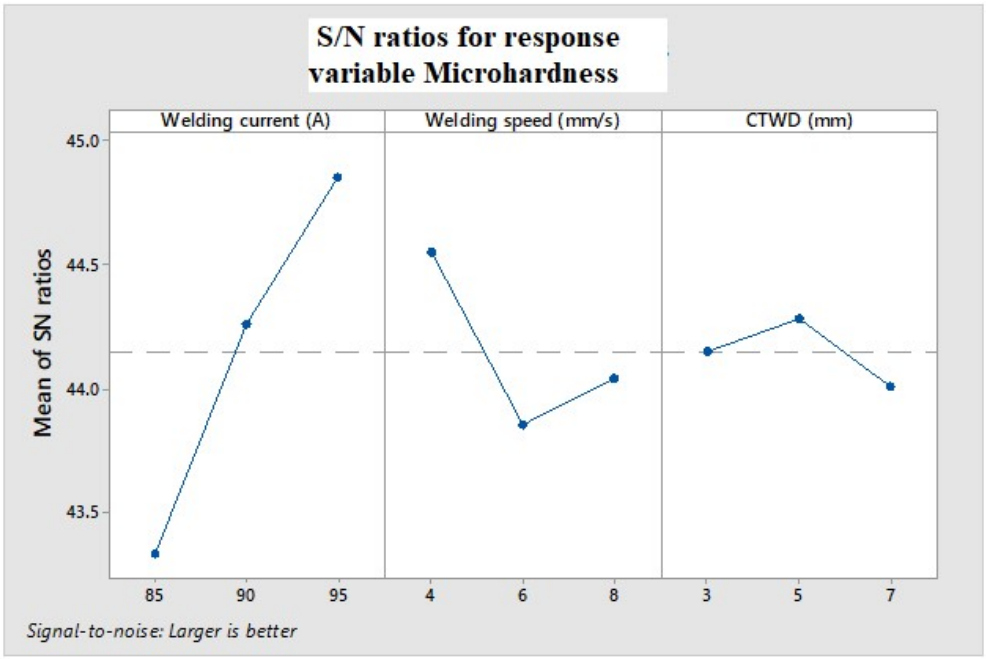

Fig. 4.7 Control parameters vs Microhardness: Mean S/N Microhardness ratios at different welding parameters

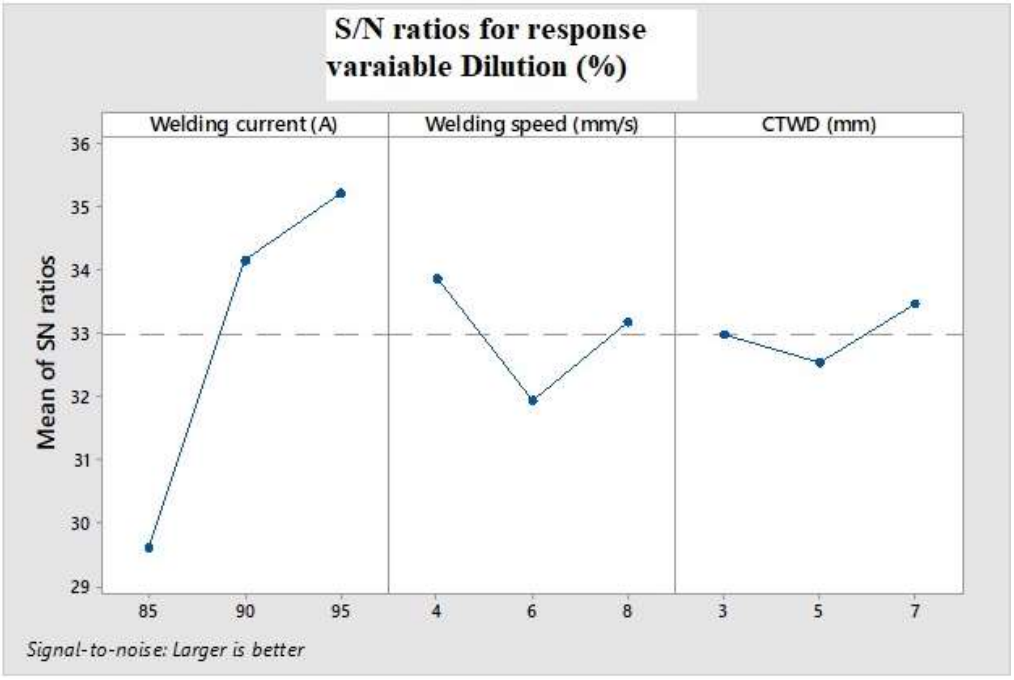

Fig. 4.8 Control parameters vs Dilution: Mean S/N Dilution ratios at different welding parameters

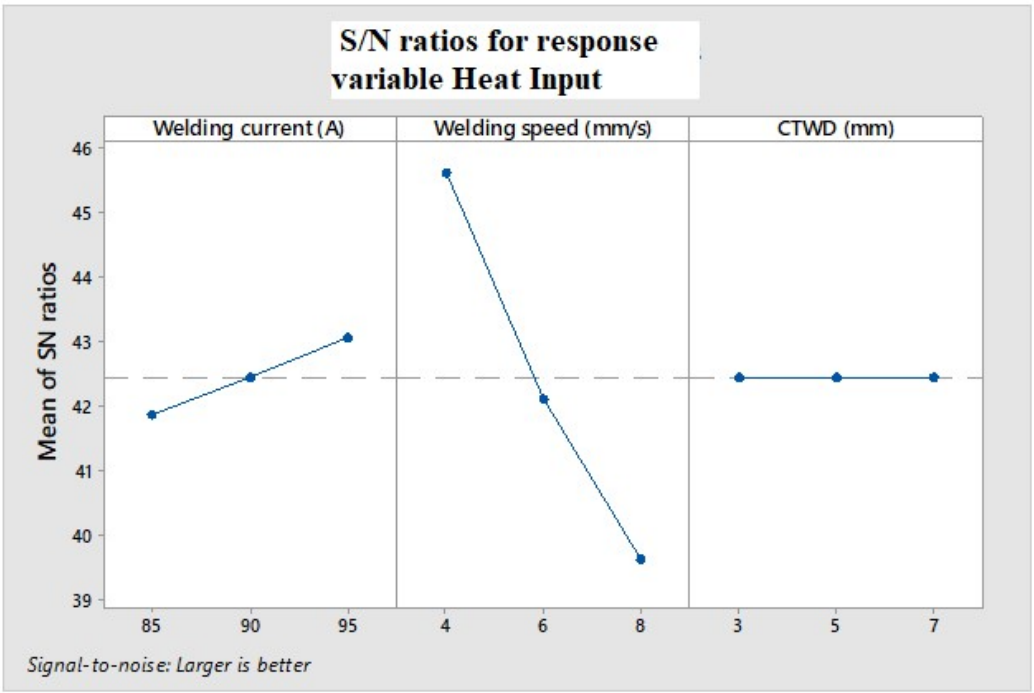

Fig. 4.9 Control parameters vs Heat Input: Mean S/N Heat Input ratios at different welding parameters

4.13 Checking the adequacy of the model for Microhardness response values with ANOVA

The ANOVA statistical technique was used to check the adequacy of the model. The results of the ANOVA for microhardness are presented in Table 4.8. The (α) value of 0.05 was used as a significance level for analysis. The p-value is compared and equated with the (α) value, which is less than the (α) value, indicating that welding parameters are significant in the output responses. The fitness of the model R-Sq the predicted R-Sq, and the adjusted R-Sq were also evaluated. The predicted R-Sq (97.51%) is also very close to the adjusted R-Sq (99.51%), which shows the high significance of the model. The value of S shows the scattering of the data from the fitted model. Lesser the value of S signifies the model is better. In Table 4.8 for microhardness response, the S value is 0.96148, which indicates the model is significant.

Table 4. 8 ANOVA for Microhardness response variable

Parameters	DOF	Adj SS	Adj MS	F-value	p-value
Welding current	2	1192.15	596.074	644.79	0.002
Welding speed	2	272.54	136.271	147.41	0.007
CTWD	2	36.55	18.274	19.77	0.048
Error	2	1.85	0.924		
Total	8	1503.09	3		
Model summary					
S	R-Sq	R-Sq(adj)	R-Sq(Pred)		
0.961480	99.88%	99.51%	97.51%		

The following Regression equation reveals the relationship between the microhardness of weld bead fusion region and input welding parameters is

Microhardness (HV) = 161.711 - 14.878 Welding current (A) (85) + 1.722 Welding current (A) (90) + 13.156 Welding current (A) (95) + 7.489 Welding speed (mm/s) (4) - 5.578 Welding speed (mm/s) (6) - 1.911 Welding speed (mm/s) (8) - 0.344 CTWD (mm) (3) + 2.622 CTWD (mm) (5) - 2.278 CTWD (mm) (7)……(4.4)

4.14 Checking the adequacy of the model for Dilution (%) response values with ANOVA

The ANOVA results for dilution responses are presented in Table 4.9. The predicted R-Sq (98.45%) is also very close to the adjusted R-Sq (99.69%), which shows the high significance of the model. The (α) value of 0.05 was used as a significance level for analysis. The p-value is compared and equated with the (α) value, less than the (α) value of input parameters, which is significant in the responses. The value of S is 0.726506, which indicates the model is effective, which is exhibited in Table 4.9.

Table 4. 9 ANOVA for Dilution (%) response variable

Parameters	DOF	Adj SS	Adj MS	F-value	p-value
Welding current	2	1217.30	608.650	1153.16	0.001
Welding speed	2	133.31	66.653	126.28	0.008
CTWD	2	23.35	11.674	22.12	0.043
Error	2	1.06	0.528		
Total	8	1375.01	3		
Model summary					
S	R-Sq	R-Sq(adj)	R-Sq(Pred)		
0.726506	99.93%	99.69%	98.45%		

The following Regression equation reveals the relationship between dilution (%) of weld bead and input welding parameters is

Dilution (%) = 46.482 - 15.976 Welding current (A) (85) + 4.601 Welding current (A) (90) + 11.374 Welding current (A) (95) + 4.634 Welding speed (mm/s) (4) - 4.789 Welding speed (mm/s) (6) + 0.154 Welding speed (mm/s) (8) - 1.129 CTWD (mm) (3) - 1.149 CTWD (mm) (5) + 2.278 CTWD (mm) (7)…….(4.5)

4.15 Checking the adequacy of the model for Heat Input response values with ANOVA

The ANOVA results for Heat Input are presented in Table 4.10. The predicted R-Sq (96.85%) is also very close to the adjusted R-Sq (99.38%), which shows the significance of the model. The (α) value of 0.05 was used as a significance level for analysis. The p-value is compared and equated with the (α) value. The p-value of welding current and welding speed input parameters is less than the value of 0.05, which is significant in the responses. However, the CTWD input parameter has a value of more than 0.05, which is in-significant in the responses.

Table 4. 10 ANOVA for Heat Input response variable

Parameters	DOF	Adj SS	Adj MS	F-value	p-value
Welding current	2	558.9	279.46	24.14	0.04
Welding speed	2	14261.4	7130.72	616.03	0.002
CTWD	2	23.2	11.58	1.00	0.500
Error	2	23.2	11.58		
Total	8	14866.7	3		
Model summary					
S	R-Sq	R-Sq(adj)	R-Sq(Pred)		
3.40225	99.84%	99.38%	96.85%		

The following Regression equation reavals the relationship between generation of Heat Input during weld bead on plate and input welding parameters is

Heat Input (J/mm) = 138.31 - 9.39 Welding current (A) (85) - 0.51 Welding current (A) (90) + 9.89 Welding current (A) (95) + 53.19 Welding speed (mm/s) (4) - 10.64 Welding speed (mm/s) (6) - 42.56 Welding speed (mm/s) (8) - 1.41 CTWD (mm) (3) - 0.84 CTWD (mm) (5) + 2.24 CTWD (mm) (7)……(4.6)

4.16 Optimal Parameter for weld bead

The highest S/N ratio in the experimental data for all three responses was observed for sample 7 (95A-4mm/sec-7mm), as shown in Table 4.1. Three samples are welded with optimal parameters to confirm the predicted results, and the average value of the three samples' test results and S/N ratios are presented in Table 4.11. The closer value S/N ratio is observed in all three responses to the predicted values. Hence the expected input welding parameters are optimal, which were considered for further welded joints.

Table 4. 11 Predicted vs Experimental results

	Optimal welding parameters	
	Predicted	**Experimental**
Microhardness		
Level	I3-S1-L2	I1-S1-L2
Microhardness (HV)	180.7	180.68
S/N ratio	45.3865	45.15093
Dilution		
Level	I3-S1-L3	I3-S1-L3
Dilution (%)	64.41	64.85
S/N ratio	36.5658	36.22217
Heat Input	279.4	282.4
Level	I3-S1-L3	I3-S1-L3
Heat Input (J/mm)	205.20	204.57
S/N ratio	46.2435	46.21689

4.2 OPTIMIZATION OF PARAMETERS FOR CMT WELD JOINTS

4.2.1 Introduction

This study performed the following steps to find the optimized weld parameters for welded joints.

(i). Select the feasible input welding parameters

(ii). Design the experimental matrix as per the Box-Behnken model

(iii). To perform the experiments as per the experimental design matrix

(iv). Recoding the experimental results.

(v). Developing the empirical relationships

(vi). Use of ANOVA for finding the significant factors

(vii). Optimized process parameters & confirmation with experimental results

4.2.2 Select the feasible input welding parameters

After number of preliminary trials and optimized process parameters of weld bead on plate investigations, the range of CMT Butt weld joint process parameters were fixed as shown in Table 4.12. The upper and lower limits for the CMT weld parameters were chosen based on the weld bead appearance and weld joint strength.

Table 4. 12 Welding Input parametes and their levels CMT welded joints

Parameter	Notation	Levels		
		-1	0	+1
Welding Current (A)	I	85	90	95
Welding Speed (mm/s)	S	4	6	8
Contact tip to workpiece distance (mm)	D	3	5	7
Arc Correction factor	C	-10	0	10

4.2.3 Design the experimental matrix as per Box-Behnken model

The welding input process parameters were selected so that all possible combination input parameters produced welded joints without any defects. Four input welding parameters, three levels, and a Box-Behnken design matrix were used to optimize the experimental conditions in this study. This design matrix uses $\alpha = \pm 1$ with the center star points of factorial space. The upper and lower limits of the factor were denoted by the numbers +1 and -1, respectively. With the application of Design Expert software, all the coefficients were determined. The mathematical models were developed after estimating the coefficients. The coefficients were checked with a 95% confidence level, and the significant coefficients were used for the final model.

4.2.4 To perform the welded joints as per experimental design matrix

The welded joints are produced per the design matrix for finding the optimum input welding parameters. A total of 29 experiments were performed to find the best suitable combination of input process parameters for fabricating the sound welded joints as per the design matrix presented in Table 4.3.

4.2.5 Recoding the experimental results

The tensile sample is extracted from all twenty-nine experiments that produced welded joints. The universal tensile testing machine with a 50 kN capacity was used for testing tensile samples. Three tensile specimens were evaluated for each welded joint, and an average of three has taken. The experimental results of welded samples are exhibited in Table 4.13.

Table 4. 13 Design matrix and experimental results of CMT welded joints

Exp. No	Coded value				Actual value				UTS (MPa)	Elongation (%)
	I	S	D	C	I (A)	S (mm/s)	D (mm)	C		
1	-1	-1	0	0	85	4	5	0	705	76
2	1	-1	0	0	95	4	5	0	734	88
3	-1	1	0	0	85	8	5	0	695	79
4	1	1	0	0	95	8	5	0	711	92
5	0	0	-1	-1	90	6	3	-10	718	81
6	0	0	1	-1	90	6	7	-10	708	84
7	0	0	-1	1	90	6	3	10	660	79
8	0	0	1	1	90	6	7	10	759	83
9	-1	0	0	-1	85	6	5	-10	717	70
10	1	0	0	-1	95	6	5	-10	733	85
11	-1	0	0	1	85	6	5	10	708	71
12	1	0	0	1	95	6	5	10	736	82
13	0	-1	-1	0	90	4	3	0	712	86
14	0	1	-1	0	90	8	3	0	625	89
15	0	-1	1	0	90	4	7	0	704	86
16	0	1	1	0	90	8	7	0	741	92
17	-1	0	-1	0	85	6	3	0	662	76
18	1	0	-1	0	95	6	3	0	707	92
19	-1	0	1	0	85	6	7	0	728	82
20	1	0	1	0	95	6	7	0	727	89
21	0	-1	0	-1	90	4	5	-10	721	71
22	0	1	0	-1	90	8	5	-10	725	89
23	0	-1	0	1	90	4	5	10	728	86
24	0	1	0	1	90	8	5	10	725	74
25	0	0	0	0	90	6	5	0	719	88
26	0	0	0	0	90	6	5	0	725	85
27	0	0	0	0	90	6	5	0	703	84
28	0	0	0	0	90	6	5	0	725	86
29	0	0	0	0	90	6	5	0	726	89

4.2.6 Developing empirical relationships

The experimental results (responses) of the CMT welded joints are UTS, and % of elongation can be revealed as the function of input welding parameters in equation 4.7.

Ultimate Tensile Strength (UTS) = f (I, S, D, C) and % of Elongation (E) = f (I, S, D,C)…….. ……(4.7)

The polynomial form for UTS, % of elongation of the CMT welded joints, could be expressed as

$$\mathbf{UTS} = b_0 + b_1(I) + b_2(S) + b_3(D) + b_4(C) + b_{12}(IS) + b_{13}(ID) + b_{14}(IC) + b_{23}(SD) - b_{24}(SC) - b_{34}(SC) - b_{11}(I^2) - b_{22}(S^2) - b_{33}(D^2) + b_{44}(C^2) \quad \ldots\ldots(4.8)$$

$$\mathbf{E} = b_0 + b_1(I) + b_2(S) + b_3(D) + b_4(C) + b_{12}(IS) + b_{13}(ID) + b14\ (IC) + b_{23}(SD) - b_{24}(SC) - b_{34}(SC) - b_{11}(I^2) - b_{22}(S^2) - b_{33}(D^2) + b_{44}(C^2) \quad \ldots\ldots(4.9)$$

Where b0 represents the mean of all responses and b1, b2, b3,...b44 represents the coefficients influenced by the various primary and interaction factors. The responses in the expression above may not be significantly impacted by all factors (primary and interaction factors).

4.2.7 Use of ANOVA for finding the significant factors

The results of ANOVA for tensile strength are presented in Table 4.14. The models are deemed sufficient because it is established that the estimated F ratios are more significant than the 95% confidence level. Higher F ratio values represent that the respective input term has more substantial and vice versa (Phillip, 1988).

Table 4. 14 ANOVA test results for Ultimate tensile strength

Source	**Sum of Squares**	**Df**	**Mean Square**	**F-value**	**p-value**		**% Contribution**
Model	18652.77	14	1332.34	19.43	< 0.0001	Significant	**95.10**
A- I	1474.08	**1**	1474.08	21.50	0.0004		**7.51**
B- S	560.33	**1**	560.33	8.17	0.0126		**2.85**
C- D	6674.08	**1**	6674.08	97.35	< 0.0001		**34.03**
D- C	3.00	**1**	3.00	0.0438	0.8373		**0.015**
AB	42.25	**1**	42.25	0.06163	0.4455		**0.22**
AC	529.00	**1**	529.00	7.72	0.0148		**2.69**
AD	36.00	**1**	36.00	0.5251	0.4806		**0.18**
BC	3844.00	**1**	3844.00	56.07	< 0.0001		19.59
BD	12.25	**1**	12.25	0.1787	0.6789		0.062
CD	2970.25	**1**	2970.25	43.33	< 0.0001		15.14
A^2	13.95	**1**	13.95	0.2035	0.6588		**0.07**
B^2	240.70	1	240.70	3.51	0.0820		1.22
C^2	1551.68	**1**	1551.68	22.63	0.0003		**7.91**
D^2	405.68	**1**	405.68	5.92	0.0290		**2.06**
Residual	959.78	14	68.56				
Lack of Fit	584.58	10	58.46	0.6232	0.7523	not significant	
Pure Error	375.20	4	93.80				
Cor Total	19612.55	28					
Std. Dev.				**R-Sq**			0.9511
Mean				**Adjusted R-Sq**			0.9021
C.V. %	1.16			**Predicted R-Sq**			0.7984
				Adeq Precision			**21.1173**

The F- the value of 19.43 shows that the model is significant. The higher value of the F-value could occur due to little percentage of occurrence of noise, i.e., 0.01%. It is observed that A, B, C, AC, BC, CD, C^2, and D^2 are essential terms. Lack of fit F-value is always

the insignificant factor for the model compared to the error. In this model, a 75.23 % chance of lack of fit value achieved, which is not a significant value, occurs due to noise factors. Model Precision enables the user to determine the signal-to-noise ratio. Generally, the required value of this is 4, but, in this case, the value is 21.1173. So, it is denoted that design is satisfactory [Goyal et al., (2015)]. The predicted R-Sq (79.84%) is also very close to the adjusted R-Sq (90.21%), which shows the great significance of the model. The (α) value of 0.05 was used as a significance level for analysis. The p-value is compared and equated with the (α) value. The p-value of welding current, welding speed, and CTWD input parameters are less than the value of 0.05, which is significant in the responses. However, the arc correction factor input parameter p-value is more than 0.05, which is insignificant in the responses. In terms of actual input welding parameters for the final model equation for UTS is given in the following equation 4.10.

Final Equation for UTS

$$UTS = +719.60 + 11.08\times A - 6.83\times B + 23.58\times C - 0.50\times D - 3.25\times AB - 11.50\times AC + 3.00\times AD + 31.00\times BC - 1.75\times BD + 27.25\times CD - 1.47\times A^2 - 6.09\times B^2 - 15.47\times C^2 + 7.91\times D^2 \text{ MPa} \qquad (4.10)$$

The above equation can be employed for calculating the quantifiable data easily. The predicted vs. actual UTS graphs of CMT welded joints are shown in Fig. 4.8 (a). Red dots represent the highest UTS value and the blue dot represents the lowest UTS value. The perturbation plots are drawn based on the influence of welding input parameters on UTS of CMT welded joints from the empirical relationships shown in Fig. 4.10 (b). The perturbation plot depicts the deviation from the reference point on the x-axis and UTS on

the y-axis. Fig. 4. 10 (c) and (d) shows the contour plots and 3-D surface plots of UTS of welded joints between welding current & welding speed input process parameters. The welding current and speed contribute the most influencing parameters for enhancing and lowering the tensile strength of the welded joint.

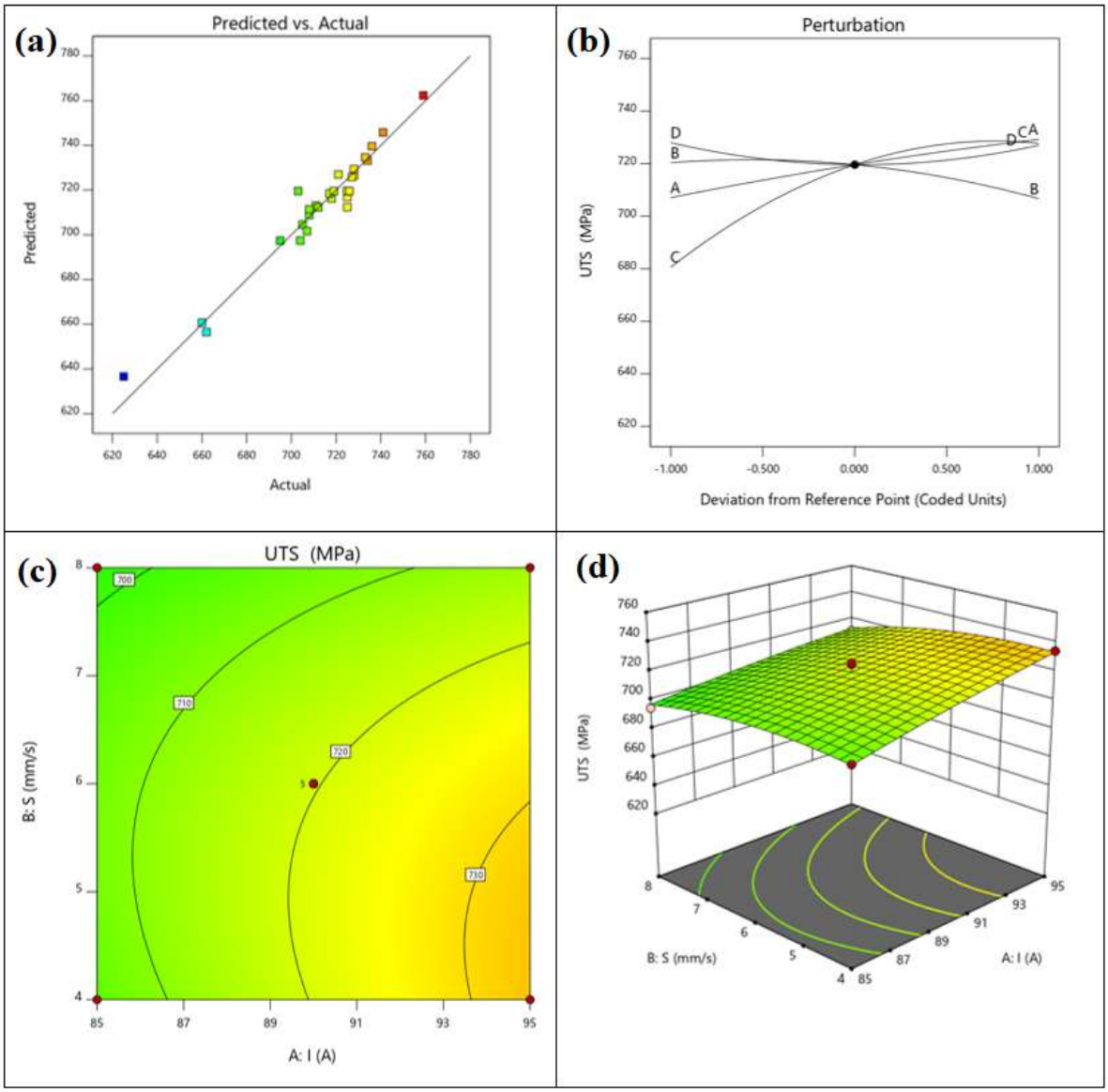

Fig. 4.10 UTS graphs (a) Predicted vs Actual (b) Perturbation plots (c) Contour plot (d) 3-D surface plot

Table 4. 15 ANOVA test results for % of Elongation

Source	Sum of Squares	Df	Mean Square	F-value	p-value		% Contribution
Model	1131.36	14	80.81	47.24	< 0.0001	significant	
A- I	456.33	**1**	456.33	266.75	< 0.0001		39.49
B- S	40.33	**1**	40.33	23.58	0.0003		3.49
C- D	14.08	**1**	14.08	8.23	0.0124		1.22
D- C	2.08	**1**	2.08	1.22	0.2884		0.18
AB	0.2500	**1**	0.2500	0.1461	0.7080		0.022
AC	20.25	**1**	20.25	11.84	0.0040		1.75
AD	4.00	**1**	4.00	2.34	0.1485		0.346
BC	2.25	**1**	2.25	1.32	0.2707		0.1947
BD	225.00	**1**	225.00	131.52	< 0.0001		19.47
CD	0.2500	**1**	0.2500	0.1461	0.7080		0.022
A^2	59.68	**1**	59.68	34.89	< 0.0001		5.165
B^2	0.3045	1	0.3045	0.1789	0.6795		0.02635
C^2	16.43	**1**	16.43	9.61	0.0078		1.422
D^2	266.38	**1**	266.38	155.71	< 0.0001		23.057
Residual	23.95	14	1.71				
Lack of Fit	6.75	10	0.6750	0.1570	0.9918	not significant	
Pure Error	17.20	4	4.30				
Cor Total	1155.31	28					
Std. Dev.	1.31			**R-Sq**		0.9793	
Mean	83.24			**Adjusted R-Sq**		0.9585	
C.V. %	1.57			**Predicted R-Sq**		0.9431	
				Adeq Precision		**23.4763**	

The results of the ANOVA for % of elongation are presented in Table 4.15. The F- the value of 47.24 shows that the model is significant. The higher value of the F-value could occur due to little percentage proportion of noise occurrences, i.e., 0.01%. It is observed that A, B, C, AC, BD, A^2, C2, and D^2 are essential terms. Lack of fit F-value is always the insignificant factor for the model compared to the error. In this model, a 99.18 %

chance of lack of fit value achieved, which is not a significant value, occurs due to noise factors. Model Precision enables the user to determine the signal-to-noise ratio. Generally, the required value of this is 4, but, in this case, the value is 23.4763. So, it is denoted that design is satisfactory [Goyal et al., (2015)]. The predicted R-Sq (94.31) is also very close to the adjusted R-Sq (95.81%), which shows the significance of the model. The (α) value of 0.05 was used as a significance level for analysis. The p-value is compared and equated with the (α) value. The p-value of current, welding speed and CTWD input parameters are less than the value of 0.05, which is significant in the responses. However, the arc correction factor input parameter p-value is more than 0.05, which is insignificant in the responses. In terms of actual input welding parameters for the final model equation for % of elongation is given in the following equation 4.11.

Final Equation for % of Elongation

$$\% \text{ Elongation} = +86.40 + 6.17\times A + 1.83\times B + 1.08\times C - 0.4167\times D + 0.25\times AB - 2.25\times AC - 1.00\times AD + 0.75\times BC - 7.50\times BD + 0.25\times CD - 3.03\times A^2 + 0.2167\times B^2 + 1.59\times C^2 - 6.41\times D^2 \quad (4.11)$$

The above equation can be employed for calculating the quantifiable data easily. The predicted vs. actual % of Elongation graphs of CMT welded joints is shown in Fig. 4.11 (a). Red dots represent the highest UTS value and the blue dot represents the lowest UTS value. The perturbation plots are drawn based on the influence of welding input parameters on % of Elongation of CMT welded joints from the empirical relationships shown in Fig. 4. 11 (b). The perturbation plot depicts the deviation from the reference point on the x-axis and the elongation percentage on the y-axis. Fig. 4.11 (c) and (d) shows the contour plots and 3-D surface plots of the elongation rate of CMT welded joints between welding current & welding speed input process parameters.

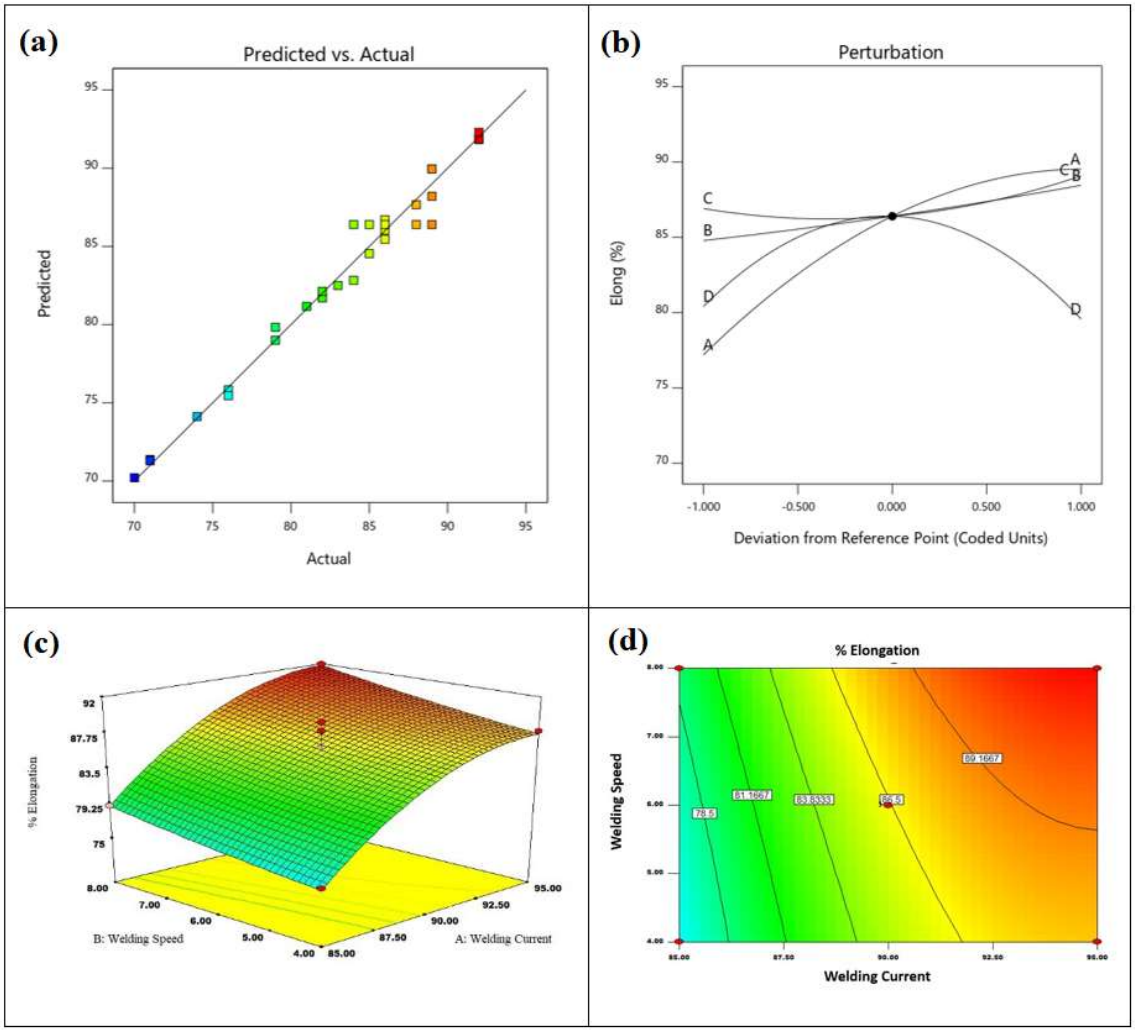

Fig. 4.11 Percentage of Elonganation graphs (a) Predicted vs Actual (b) Perturbation plots (c) Contour plot (d) 3-D surface plot

4.2.8 Optimized process parameters & confirmation with experimental results

This study uses to find the optimum input welding parameters for the highest or lowest value of output responses. The highest tensile strength and a significant elongation percentage were identified from response surface plots and 3-D contour graphs. For the optimum value responses, the corresponding input welding parameters values of welding current, welding speed, CTWD, and the arc correction factor are listed in Table 4.16. Three welded joints were fabricated from the optimized conditions in the same welding experimental setup to validate the model. From the welded joints, three tensile tests were carried out in each welded joint; an average of three is presented in Table 4.17. These results confirmed that the predicted and experimental tensile test results were in acceptable values, which is exhibited in Table 4.17. The error percentage is calculated based on the following equation (4.12).

$$\% \text{ of Error} = \frac{\text{Experimental value} - \text{Predicte value}}{\text{Experimental value}} \text{ X } 100 \quad \ldots\ldots\ldots\ldots\ldots\ldots\ldots\ldots\ldots\ldots\ldots\ldots(4.12)$$

The confirmation tensile test results revealed that the results acquired are close to the predicted values and the percentage of error is in acceptable range hence the model developed is accurate.

Table 4. 16 Optimized condition for CMT welded joints

S. No	Parameters	Optimized value	Result	
			UTS	Elongation
1.	Welding Current (I), A	92	745	92
2.	Welding Speed (S), mm/s	8		
3.	Contact tip to workpiece distance (D), mm	7		
4.	Arc Correction factor	0		

Table 4. 17 Validation of the test results

Results				% of Error	
Predicted		Experimental			
UTS (MPa)	Elong (%)	UTS (MPa)	Elong (%)	UTS (MPa)	Elong (%)
723.823	91.99	726.7	89.1	0.39	-3.24
		722.4	90.6	- 0.19	-1.53
		723.9	93.2	0.01	1.3

4.3 MICROSTRUCTURAL ANLYSIS ON CMT BUTT WELD

Fig. 4.12 depicts the microstructure of various regions of a welded specimen, (a) Weld Bead, (b) Fusion line, (c) Base metal region, and (d) HAZ. The hardness and tensile strength of SS 304 mainly depend upon the microstructural evaluation and solidification behavior of welded material [Dak and Pandey, (2020), Sridar et al., (2020)]. During welding, the filler wire fuses with parent metal in a liquid state due to refined grain size occurring in the weld bead, as seen in Fig. 4.12 (a). In HAZ, the grain size has increased due to material softening during welding, as seen in Fig 4.12 (b & d). The solidification of material after welding causes the formation of dendrites. Pandey (2020) also observed the dendrite and inter-dendritic structure in HAZ of SS304 welded material. The presence of Cr and Ni-rich elements in the HAZ are responsible for forming dendrite phases. Kumar and Shahi, (2016); Kumar and Shahi, (2011) reported that different heat input in GTAW welding of AISI 304 SS changes the mechanical properties and microstructural behavior of the welded joints. More extensive heat input experiences for forming the dendrite and inter-dendrite structure in a welded joint. The XRD confirms the austenitic γ (111) phase in the base material 304SS [Loayza et al., (2011)]. The weld bead consists of Austenite, Ferrite, $Fe_{0.64}Ni_{0.35}$, $Cr_{0.19}Fe_{0.7}Ni_{0.11}$, and $C_{0.09}$ phases, as seen in Fig. 4.13. The intensity

of the γ (111) plane in welded material has differed from the base material. The γ (111) phase of 304SS has crystal growth in the preferred orientation direction [Hsieh et al., (2013)]. Fig. 4.14 shows the FESEM with EDX results of the CMT weld bead zone. FESEM image shows the combination of austenite and martensite phases. EDX results confirm the presence of Cr and Ni elements in the weld region which is transformed from filler material as required by the chemical composition weight % of 304 SS.

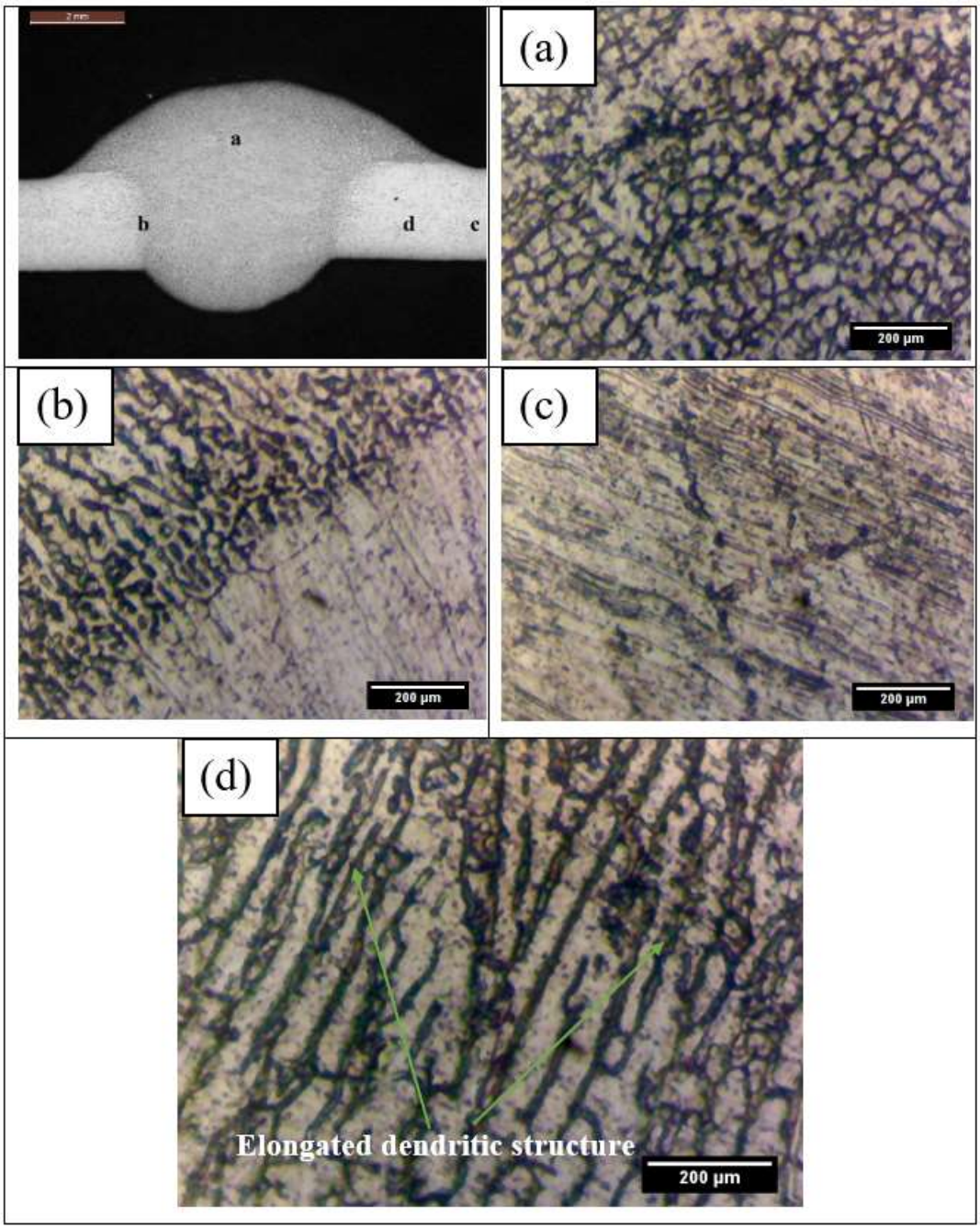

Fig. 4.12 Microstructure of weld sample (current of 95A, speed of 4 mm/sec and CTWD of 7mm) **at various position (a) Weld bead (b) Fusion Line (c) Base metal zone (d) HAZ**

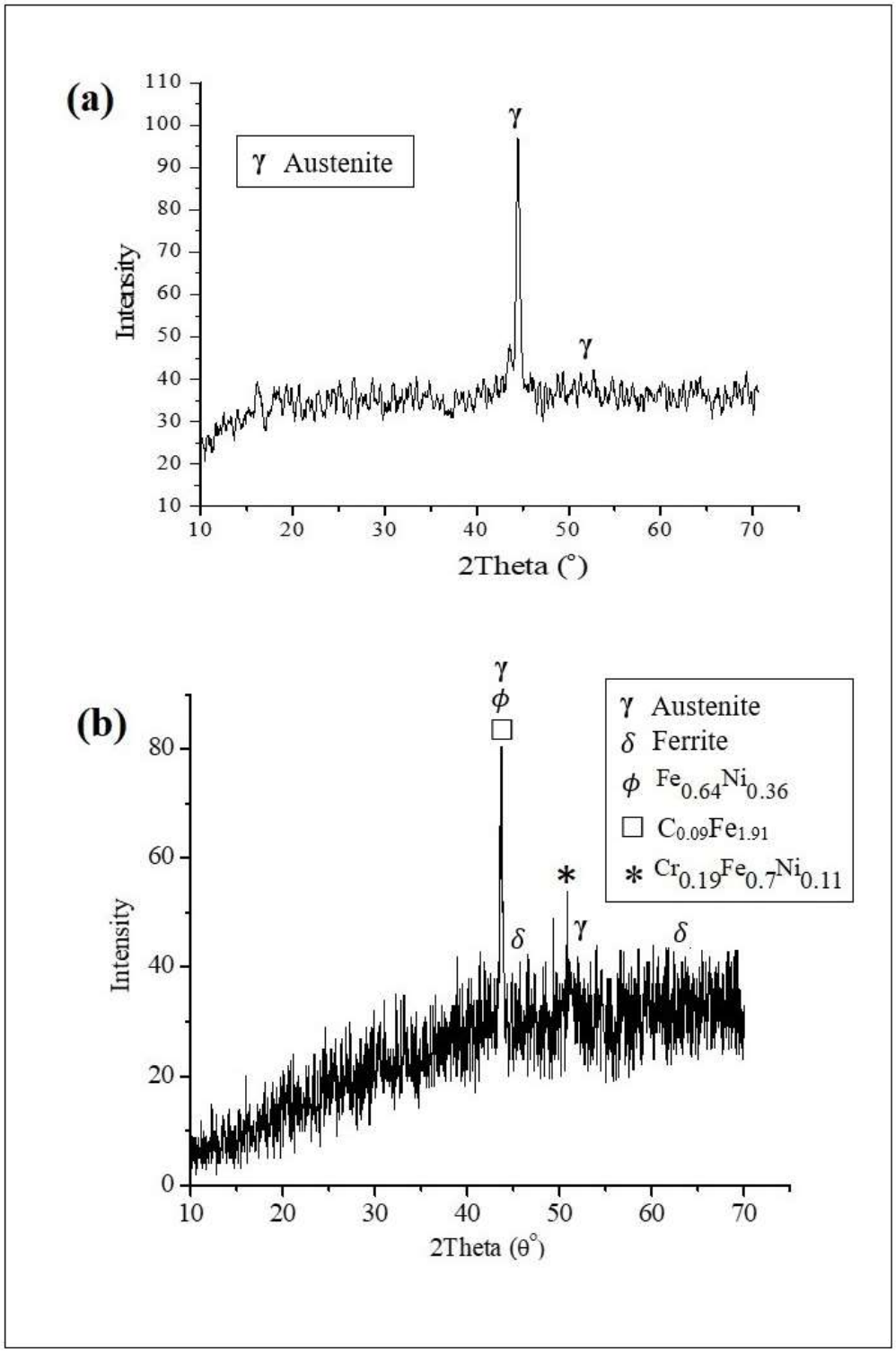

Fig. 4.13 XRD images of (a) Base material (b) Weld bead

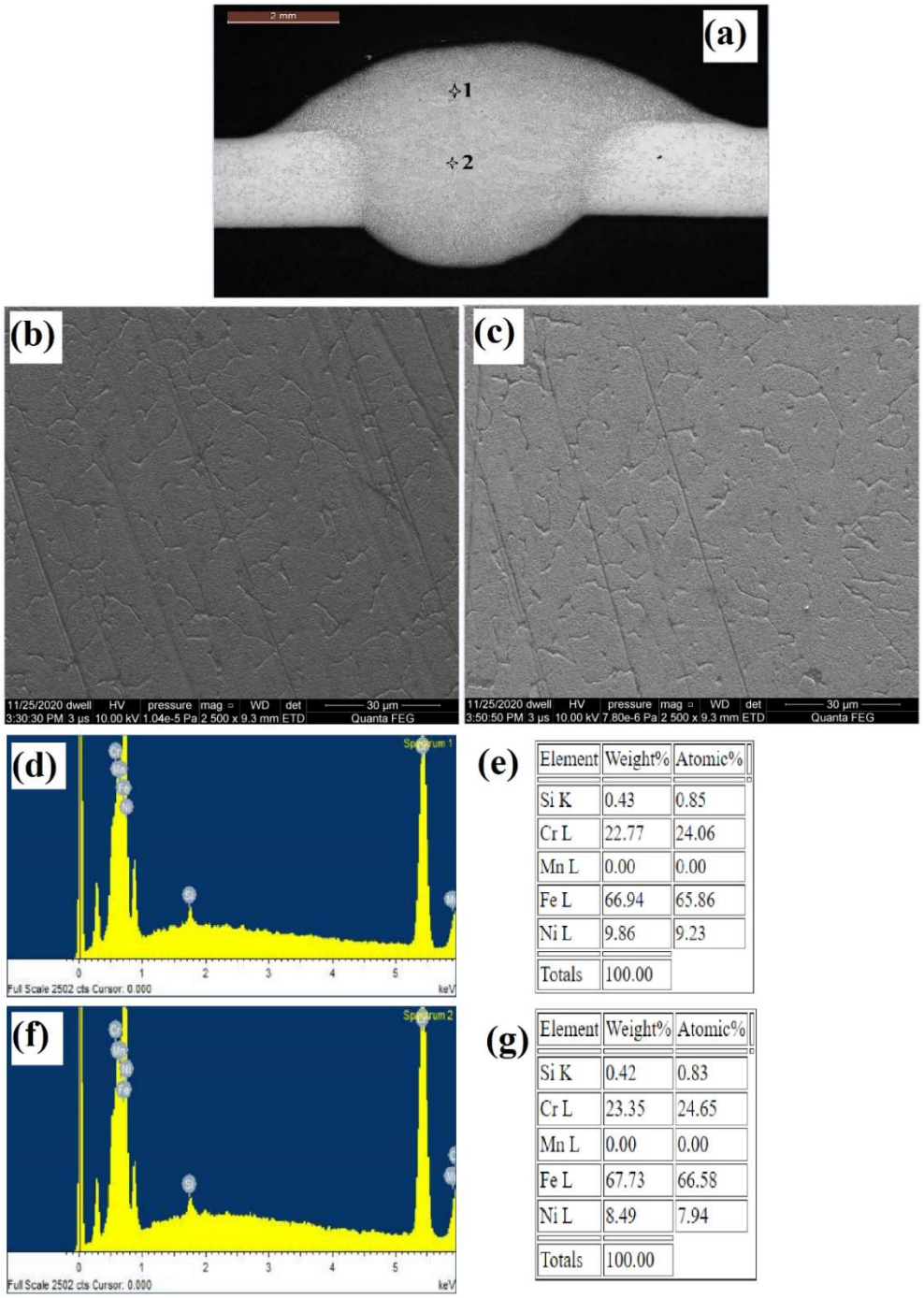

(e)

Element	Weight%	Atomic%
Si K	0.43	0.85
Cr L	22.77	24.06
Mn L	0.00	0.00
Fe L	66.94	65.86
Ni L	9.86	9.23
Totals	100.00	

(g)

Element	Weight%	Atomic%
Si K	0.42	0.83
Cr L	23.35	24.65
Mn L	0.00	0.00
Fe L	67.73	66.58
Ni L	8.49	7.94
Totals	100.00	

Fig. 4.14 FESEM and EDX results of CMT at weld bead (a) The points indicate FESEM image taken on weld bead (b) & (c) FESEM image at point 1 and point 2 respectively (d) & (e) Spectrum image of point 1 with its composition in weight % (f) & (g) Spectrum image of point 2 with its composition in weight %

4.4 MECHANICAL PROPERTIES ON CMT BUTT WELD

4.4.1 Ultimate Tensile Strength

Fig. 4.15 shows the tensile test specimens after testing. Welded Joint strength mainly depends upon the heat input during the welding process. Lesser strength welded samples occur due to the formation of higher brittle intermetallic compounds in the fusion region, which is seen from the XRD and EDX plots of the weld bead.

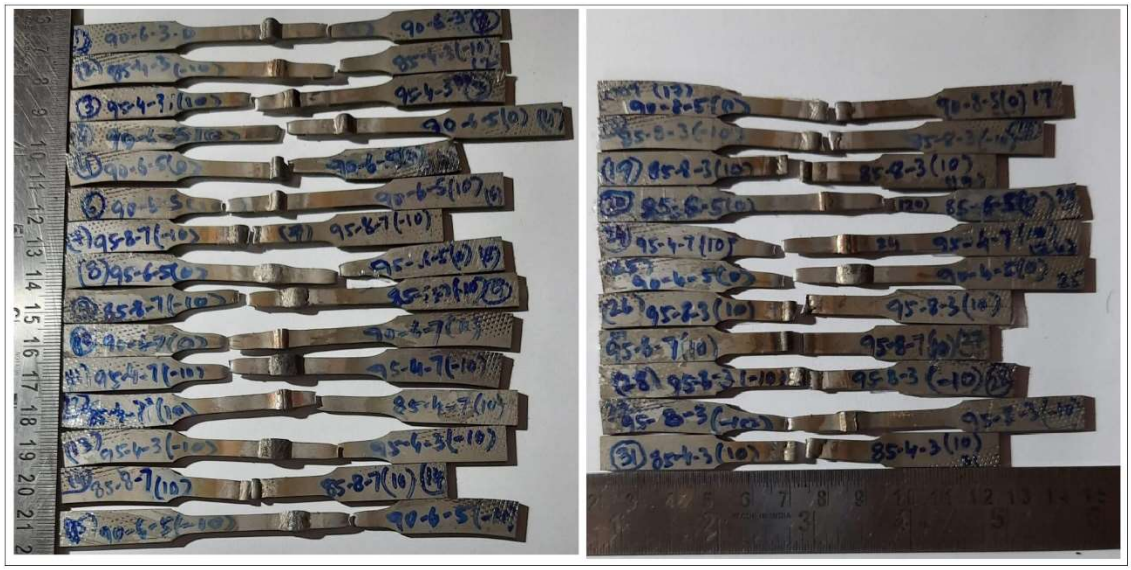

Fig. 4.15 CMT tensile samples after fracture

Heat input is mainly dependent on welding current, speed, and voltage. Welding of larger thickness material requires higher heat input. However, welding speed also depends on thickness—too high or too low welding speed results in inadequate weld penetration. The microstructure of the weld bead is affected by heat input. The austenite/ferrite balance in the welded joint greatly influences the steel properties. The refinement of grain is also governed due to controlled heat input observed from the microstructure. In this process, swift retraction of filler wire during the short circuit process takes place to manage the heat input. With the welding parameters (welding current of 95A, speed of 4mm/sec, CTWD of 7 mm), one sample is also welded with the MIG pulse welding process for

comparison with CMT sample, as shown in tensile graph Fig. 4.16. The results revealed that the tensile properties of MIG welded samples are decreased due to higher heat input. Higher heat inputs than the required rate deteriorate the mechanical properties and the microstructure of the welded joint due to material softening.

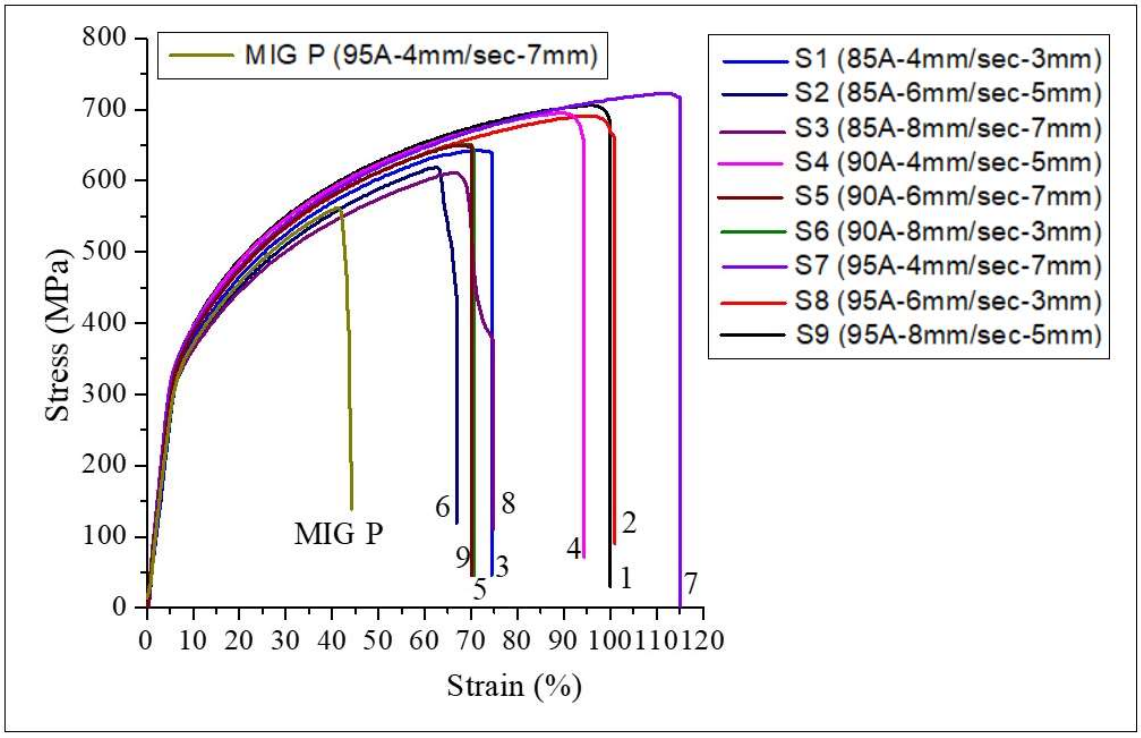

Fig. 4.16 Stress vs strain graphs of CMT and MIG P welded joint

The tensile test fractured surface FESEM images of sample welded with (welding current of 95A, speed of 4 mm/sec, and CTWD of 7mm) taken at various magnifications are shown in Fig. 4.17. It indicates dimpled morphology without cracks, and minimum carbide precipitation is noticed. Very fine dimples (microscopic pits) with various sizes of voids were observed on the tensile broken fracture surface. Due to high-stress concentration, the growth of large size microvoids and sub-microvoids takes place in the welded region [Pandey et al., (2017), Singh et al., (2018) and Pandey et al., (2018)]. The

ductile fracture is observed in Fig. 4.15 (c), which shows the material experiences higher elongation and enhances the weld joint strength. The spectrum 3 and 4 points mentioned in tensile fracture surfaces are taken for EDX studies which are exhibited in Fig. 4.15 (e & f). EDX analysis shows the presence of Cr, Ni, Mn & Fe as main elements and carbide precipitation as a secondary phase. Kumar and Shahi, (2016) observed similar dimpled morphology with a high degree of precipitation and flat, featureless region in GTAW welding of 304L SS. The high degree of precipitation affects the grain boundaries separation, which leads to the degradation of mechanical properties.

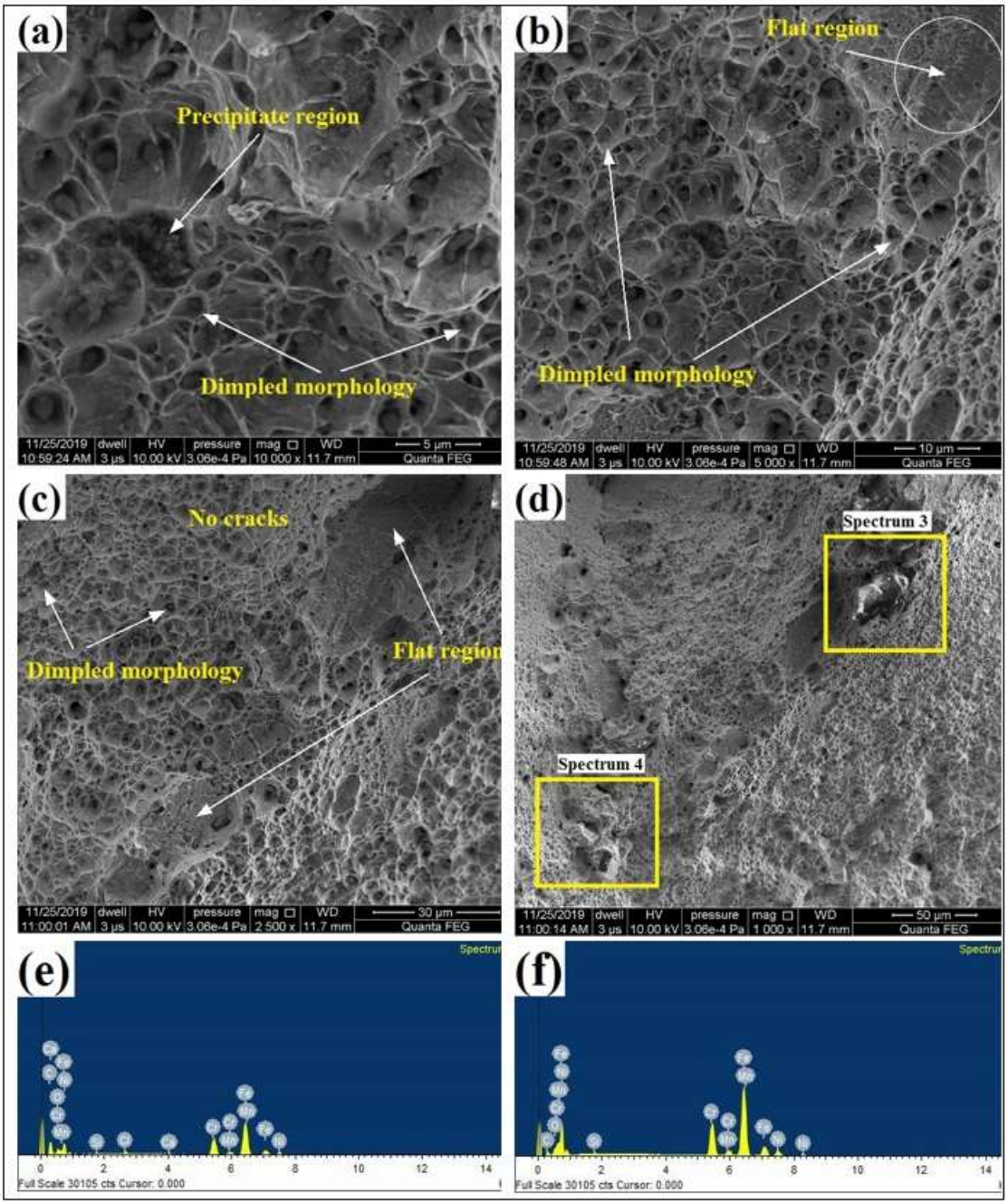

Fig. 4.17 (a – d) FESEM images of the fracture surface of CMT welded sample taken at various magnifications and (e & f) EDX was taken at spectrum 3 and 4 points

Radiography testing is conducted to check the weld joint quality. Welding defects such as cracks, porosity, lack of fusion, etc., are detected through radiography tests as per ASTM Sec.-V:2017 standards. Fig. 4.18 clearly shows no defect observed in the weld bead, indicating the stronger welded joint.

Fig. 4.18 Radiography test as per ASME Sec.-V:2017 of CMT welded sample

4.4.2 Microhardness

The micro-hardness value of the welded samples taken at various points is shown in Fig. 4.19. It is seen from the hardness of the HAZ region, and the weld bead has less than the base metal. Approximately 16 % and 25 % decrease in the microhardness is experienced in the HAZ and weld bead, respectively, compared with the base metal region. The decline in hardness in the weld region and HAZ is due to the formation of dendrites seen in microstructural image Fig. 4.12 (a) & (d). The weld zone experiences a small dendrite, whereas HAZ experiences an elongated dendritic structure. In the interface region, the grain size becomes courser due to softening behavior of higher heat input which is seen

in Fig. 4.12 (b). At higher heat input, austenitic stainless steel undergoes softening behavior, which deteriorates the tensile strength and micro-hardness [Kumar and Shahi, (2011)].

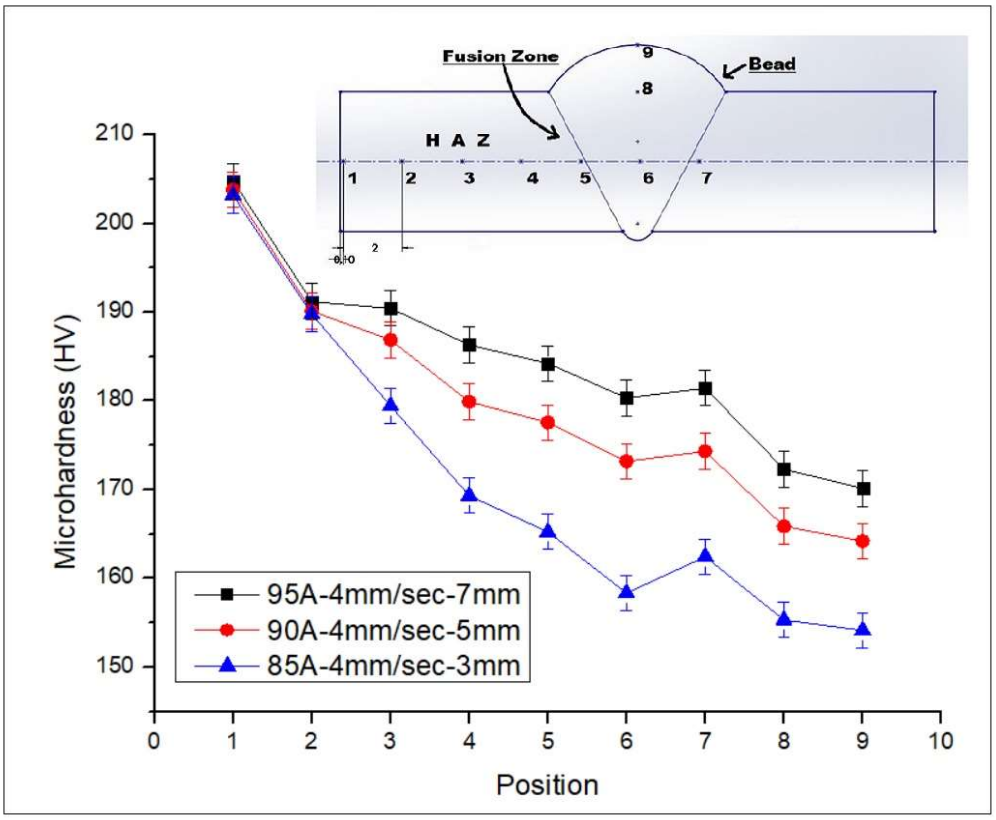

Fig. 4.19 Microhardness at various position

4.4.3 Residual Stress

Residual stresses are measured through destructive and non-destructive techniques. The most familiar destructive methods are the hole-drilling technique, deep hole method, sectioning technique, ring-core method, and contour method. Hole-drilling technique is an easy and convenient process capable of determining the direction, magnitude, and sense of residual stress distribution across a thickness. The ring core method measures the deformation of the material in a central area. This technique has

superiority over the hole-drilling method, which gives better surface strains. The deep hole technique is utilized to measure the deep interior stresses.; it has combined features of hole-drilling and ring-core methods. The contouring technique is simpler to use because it requires almost no calculations [Taraphdar et al., (2021); Pandey et al., (2018); Rossinin et al.,, (2012)]. The nondestructive techniques are based on diffraction methods. The most common nondestructive methods are X-ray diffraction, neutron diffraction, Barkhausen noise method, and ultrasonic method. In the X-ray diffraction method, the inter-planar atomic spacing can be precisely measured, and overall metal stress can be calculated.

The neutron diffraction technique can measure extensive thickness material with larger penetration than the X-ray diffraction method. The magnetic Barkhausen noise technique measures the residual surface stress of ferromagnetic materials. The ultrasonic method measures residual and applied stresses of the interior depth of material. In addition, this technique is simple, portable, economical, and free from radiation hazards [Rossinin et al., (2012); Gadallah et al., (2021); Kumar et al., (2021)]. Pandey et al., [2018] used the blind hole-drilling process for measuring the axial and transverse residual stresses of various P91 steel welded plates. Taraphdar et al., (2020) introduce a novel deep hole contour method to measure residual stress. This method can measure through-thickness residual stress distribution with a lower degree of specimen damage than the deep hole-drilling and contour process methods. Banik et al., [2021] evaluated thick welded austenite stainless-steel plates' residual stresses using the blind hole and deep hole-drilling techniques. The residual stresses

are higher throughout the thickness of higher strength welded material than lower strength welded material. Lai and Wu, (2020) investigated residual stresses of three different welded low-carbon sheets of steel by two other X-ray stress analyzers, namely μ-X360 and iXRD diffractometer.

A higher rate of solidification occurs in the upper and lower portion of the fusion region due to the weld material's fast cooling, resulting in residual stresses. When any material unexpectedly fails, it often occurs for many reasons, but tensile residual stress also creates a possibility of unexpected failure. Residual stress results at various positions of the welded joints are presented in Fig. 4.20. Uneven thermal distribution occurs in the welded joint due to contraction and expansion in HAZ and fusion zone. The different cooling rate in the weld zones influences the growth of residual stresses due to the change in microstructure pattern. The residual stresses are also affected by the phase transformation in the fusion region and HAZ [Zhang, (2020)]. The larger size of the fusion area and HAZ takes place with expansion in heat input during welding.

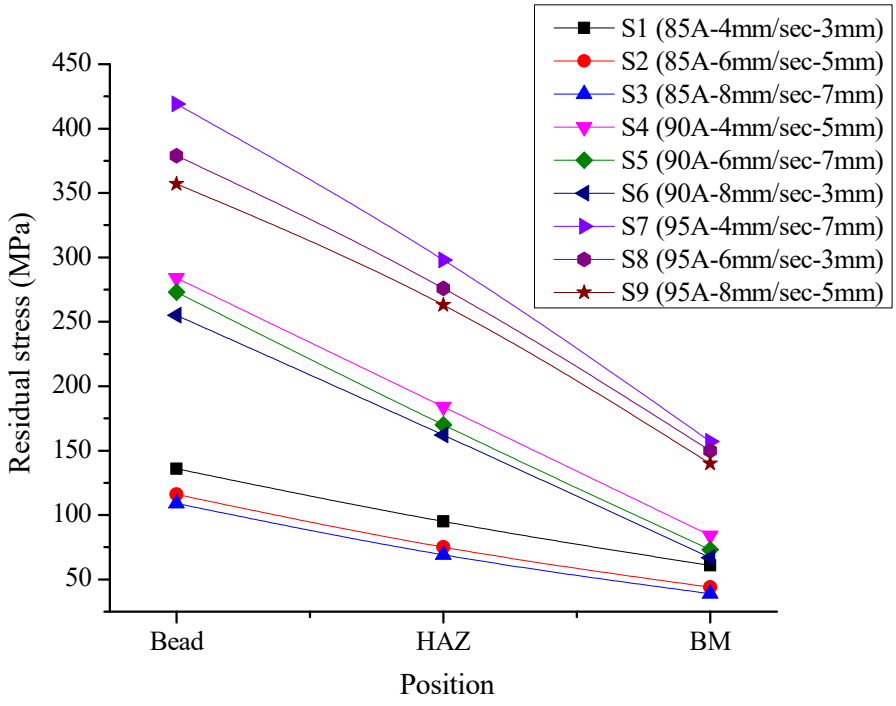

Fig. 4.20 Residual stress graph of welded samples taken at various points

In the HAZ, tensile residual stresses (positive) are observed, which results in fatigue failure and might be the possibility of crack commencement which leads to weakening of the mechanical properties. The distortion is seen in Fig. 4.21 (a) for CMT sample welded with (welding current of 95A, speed of 4mm/sec, CTWD of 7mm) at weld bead position, and a smaller amount of distortion is observed for welded sample welded with (welding current of 85A, speed of 8 mm/sec and CTWD of 7 mm) at a base metal region seen in Fig. 4.21 (b). This distortion is caused due to higher heat input which is experienced. The profile curve of residual stress at weld bead shows the number of peaks incurred in the material compared to the base material. The red color shade peaks indicate a higher absorption of residual stresses. In contrast, the blue color shade peaks indicate a negligible concentration of residual stresses, which is seen in the profile curve of Fig. 4.21 in both

cases. The UTS of welded sample (welding current of 95A, speed of 4mm/sec and CTWD of 7 mm) is higher than the tensile residual stresses, including the maximum tensile residual stress. The appropriate heat input enhances the joint efficiency, so the material breaks from the base metal.

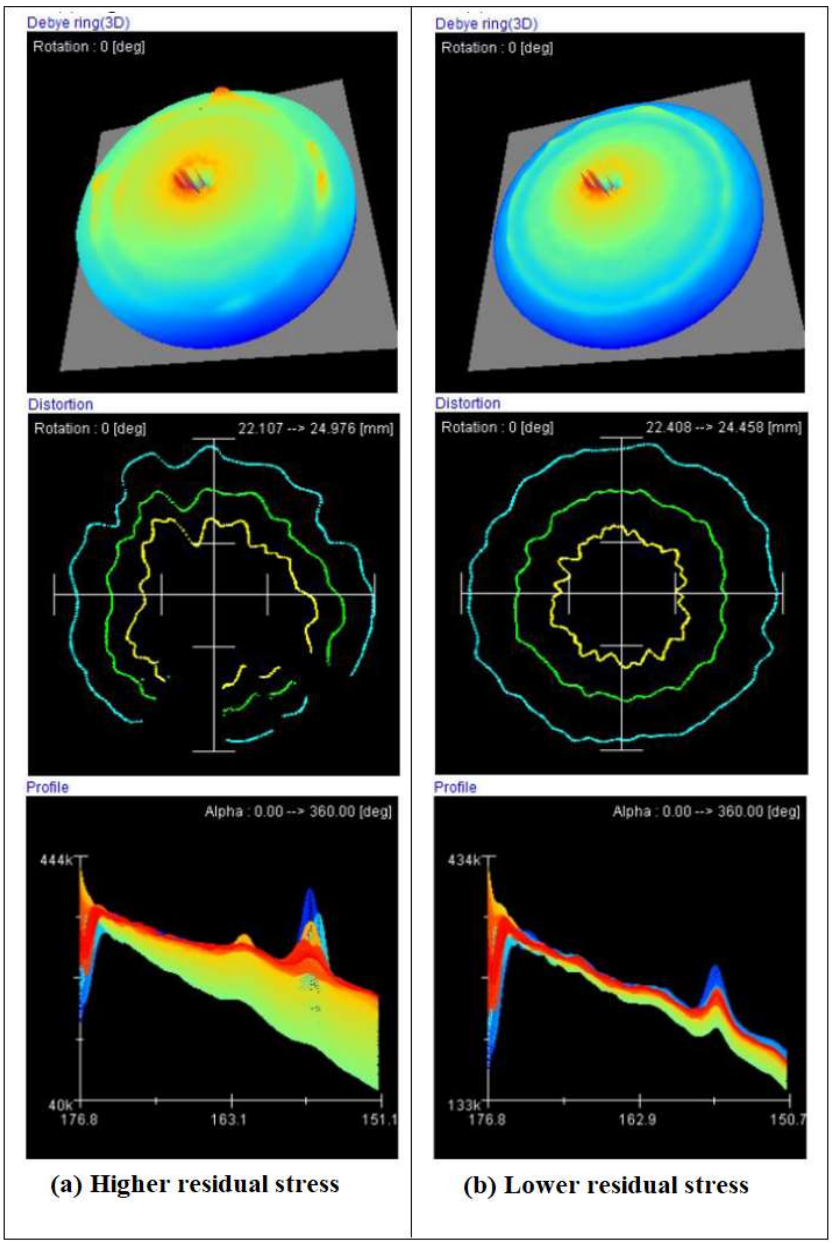

Fig. 4.21 Debye ring (3D), distortion and profile curve of residual stress for (a) Higher residual stress sample and (b) Lower residual stress sample

4.5 SUMMARY

In this chapter, Taguchi L9 orthogonal array technique is applied to find optimum input welding parameters to maximum microhardness and percentage of AISI 304 stainless steel dilution. Input parameters such as welding current, speed, and CTWD are considered. The cross-section of weld bead macro images produced with all input welding parameters combinations per the design matrix is presented. For finding the maximum tensile properties of the welded joints, RSM with the Box-Behnken model is used with four input welding parameters and three levels. The empirical regression equations predicted vs. actual plots, perturbation plots, and 3-D surface plots are plotted for validation and confirmation of the model. In the CMT welded joint, microhardness, residual stresses, and NDT radiographic technique have also been investigated to find the quality of the joint.

CHAPTER 5 : RESULTS AND DISCUSSION ON U-CMT BUTT JOINTS

5.1 Introduction

Recent years the ultrasonic vibrations assisted during welding has given more importance for due to enhancement in grain refinement of welded material and increase in homogeneity reinforcement material with the base material [Zhou et al., (2018); Wang et al., (2020)]. The ultrasonic treatment during welding enhances the mechanical properties, eliminating the heat treatment of the welded joint and reduces the residual stresses of the joint [Jose et al., (2016)]. In this chapter three different welding currents selected to fabricate welded joints; with ultrasonic vibrational assistance and without vibrational assistance. Two different ultrasonic vibrational amplitude are chosen to investigate microstructural effects, microhardness, tensile properties, and residual stresses of welded joints.

5.2 COMPARISON BETWEEN CMT AND U-CMT BUTT JOINTS

5.1.1 Effect of ultrasonic vibrations on the microstructure

The fabricated welded joints are visually examined before the characterization and ensuring that the welded samples are free from surface defects. Fig. 5.1 illustrates the schematic diagram of weld metal geometry. The variation in macro images of weld metal geometry of CMT and U-CMT welded samples is shown in Fig. 5.2. The U-CMT sample's weld width is enlarged compared to the CMT sample, which is seen in macro images of welded samples. The microstructure of the fusion region, HAZ & base metal of CMT, and U-CMT welded samples are shown in Fig. 5.3 and Fig. 5.4, respectively. Sun et al., (2009) reported that the weld width of ultrasonic-assisted 304 SS GMAW welded joints increases

in comparison with non-vibration assisted welded joints. The vibration energy increases the effect of push force continuously in the molten arc due to more filler metal being fused with the base metal. In the HAZ of the CMT welded sample (Fig. 5.4 (c)), long, size dendrites and columnar shape grains were observed. With vibration, the smaller size dendrites and equiaxed grains were observed, which is seen from Fig. 5.3 (c).

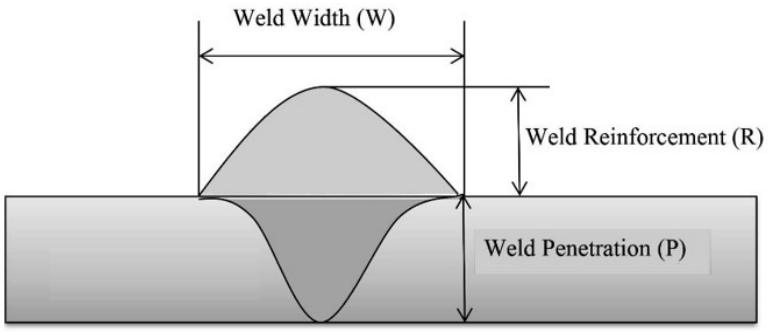

Fig. 5. 1 Schematic diagram of weld bead dimensions

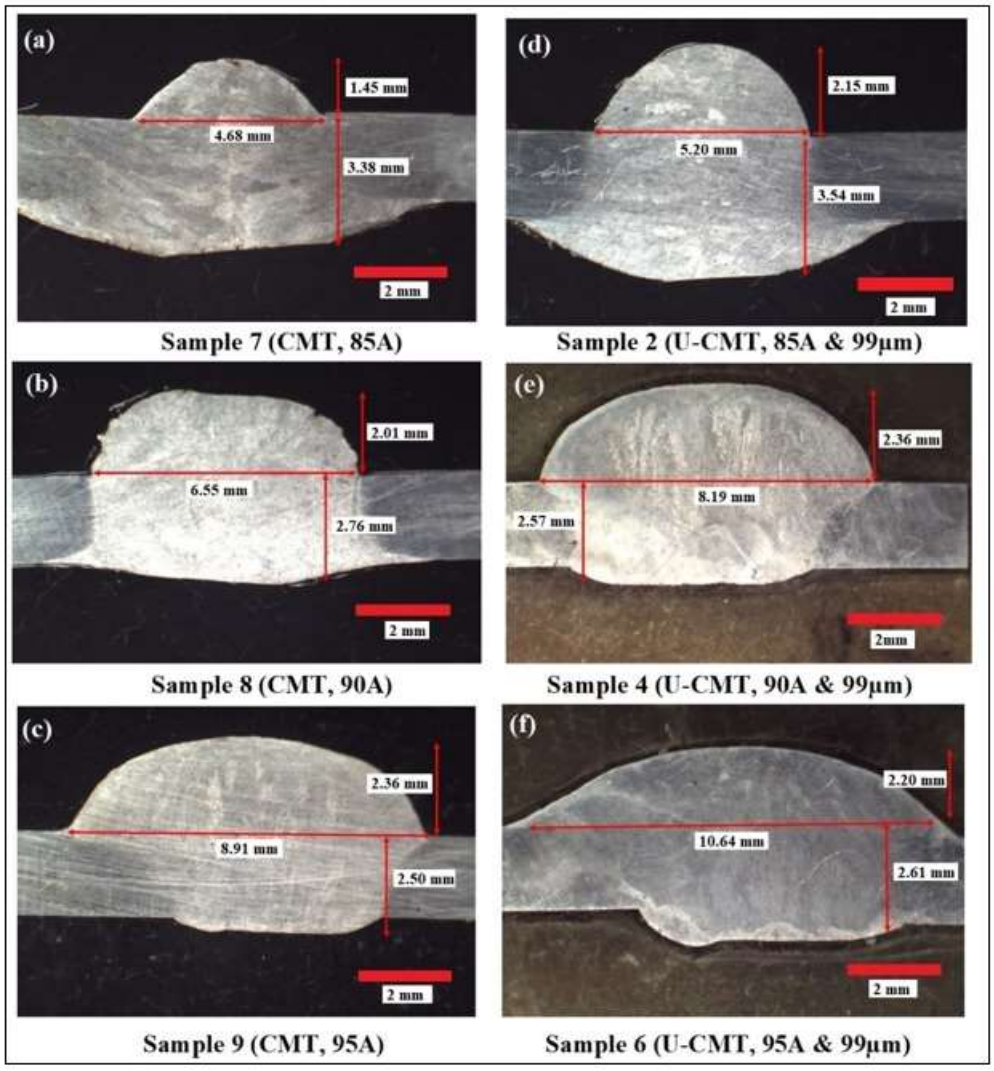

Fig. 5. 2 Variation in macro images of weld bead geometry of CMT and U-CMT welded samples

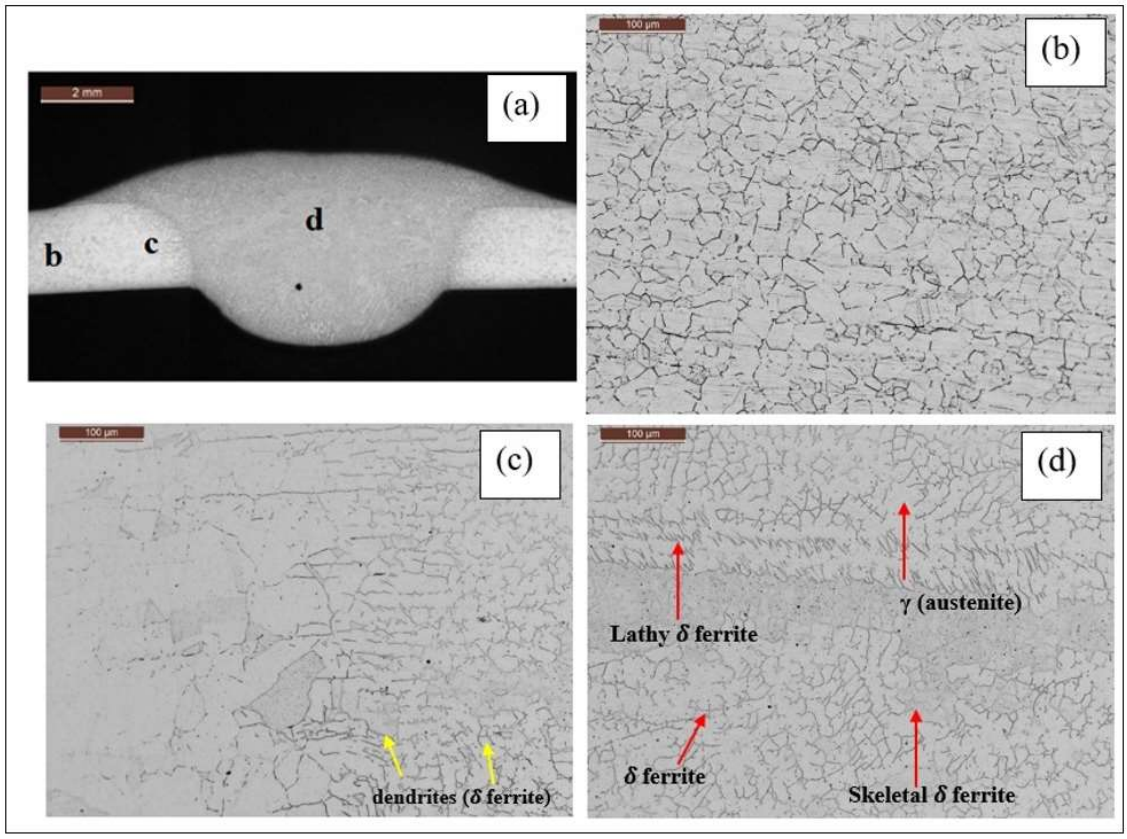

Fig. 5. 3 Macrostructure (a) and Microstructure of CMT welded sample 9 (95-4-7) at various positions (b) Base metal region (c) HAZ (d) weld region

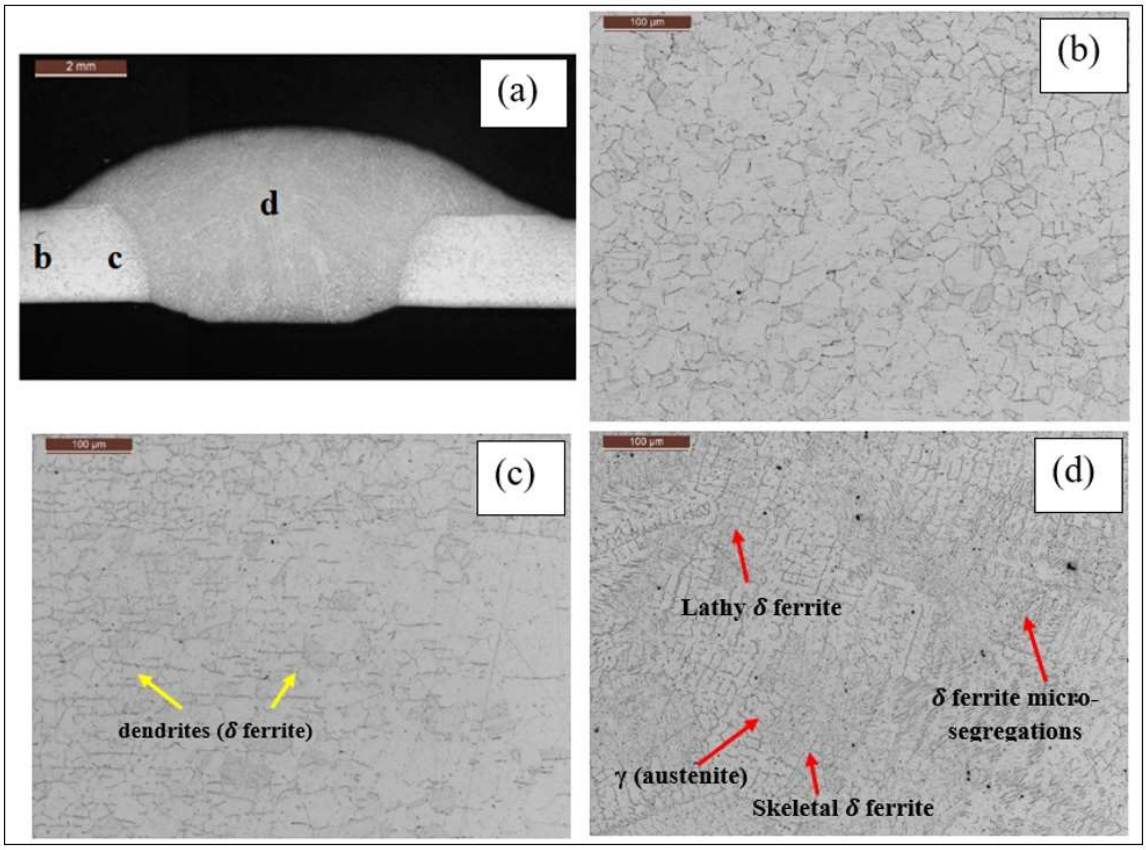

Fig. 5. 4 Macrostructure (a) and microstructure of U-CMT welded sample 6 (95-4-7, 99µm) at various positions (b) Base metal region (c) HAZ (d) weld region

With vibration, the molten weld material can break the dendrites due to the nucleation site being formed. During ultrasonic vibration-assisted welding, the temperature distribution is uniform [Kuo et.al., (2008)]. Wei, (1992) reported that the vibration fastens the disperse of molten weld material uniformly and adjusts the weld pool temperature uniformly as a result of equiaxed grains formed. The ultrasonic vibration introduction in weld pool material causes the cavitation effect in welded material, resulting in the finer size of grains of primary δ ferrite and an increase in dendritic fragmentation [Yuan et. al., (2016); Chen et. al., (2020)]. Further vibration boosts the solid-liquid interface with the help of supercooling to nucleate from weld pool liquid.

Skeletal and lathy ferrite is developed in the austenite matrix in the weld region, which is seen from Fig. 5.3 and Fig. 5.4. In HAZ, dendrite and inter-dendritic phases and a few δ ferrite patches also are observed. The lower input vibrational amplitude has a better degree of grain fragmentation. With an increase in welding current, there will be increase in grain fragmentation; subsequently, the grain size of welded samples is decreased. Chen et. al., (2017b) reported that the ultrasonic amplitude has an appreciable effect on grain fragmentation of ultrasonic-assisted welding of Al. The linear relationship takes place between welding current and grain fragmentation. The nonlinear relationship takes place between ultrasonic amplitude and grain fragmentation. Fig. 5.5 (a) and (b) show the grain size distribution chart for CMT & U-CMT samples of HAZ and fusion region, respectively. The average grain size is measured using Image J analysis from the microstructure. The selected base material's average grain size is around 50µm. The average grain size of the U-CMT samples in the fusion region is approximately 36µm, and for CMT samples are about 45µm. The vibrations reduced the contact time between the refined grains during solidification of the molten weld pool, which results in the reduction of micro-segregation in the fusion region, which can see in Fig. 5.4(d). In addition, enhanced Cr, Ni, and Fe contents segregated surface is formed in the dendritic and inter-dendritic regions.

Fig. 5.6 shows the microstructure of HAZ and fusion regions of U-CMT samples welded at 50µm and 99µm vibrational amplitude. With an increase in vibrational amplitude, smaller size ferrite (δ) was observed in the fusion region. FESEM images (Fig. 5.7) at the weld metal show the austenite (γ) at the primary region and ferrite (δ) at grain boundaries.

The filler wire coalesces with base material during welding, and solidification takes place subsequently, delta ferrite and austenite grains formed with no trace of equiaxed grains. The δ ferrite and austenite grains form due to peritectic- eutectic reactions and moderate cooling rate during solidification. Pandey, (2020) also observed the δ ferrite formation in the 304 SS welded joint due to a lack in phase transformation. The Ni enriched dendrite phase is austenite, and Cr enriched inter-dendritic phase is ferrite in the fusion region [Mirshekari et. al., (2014)].

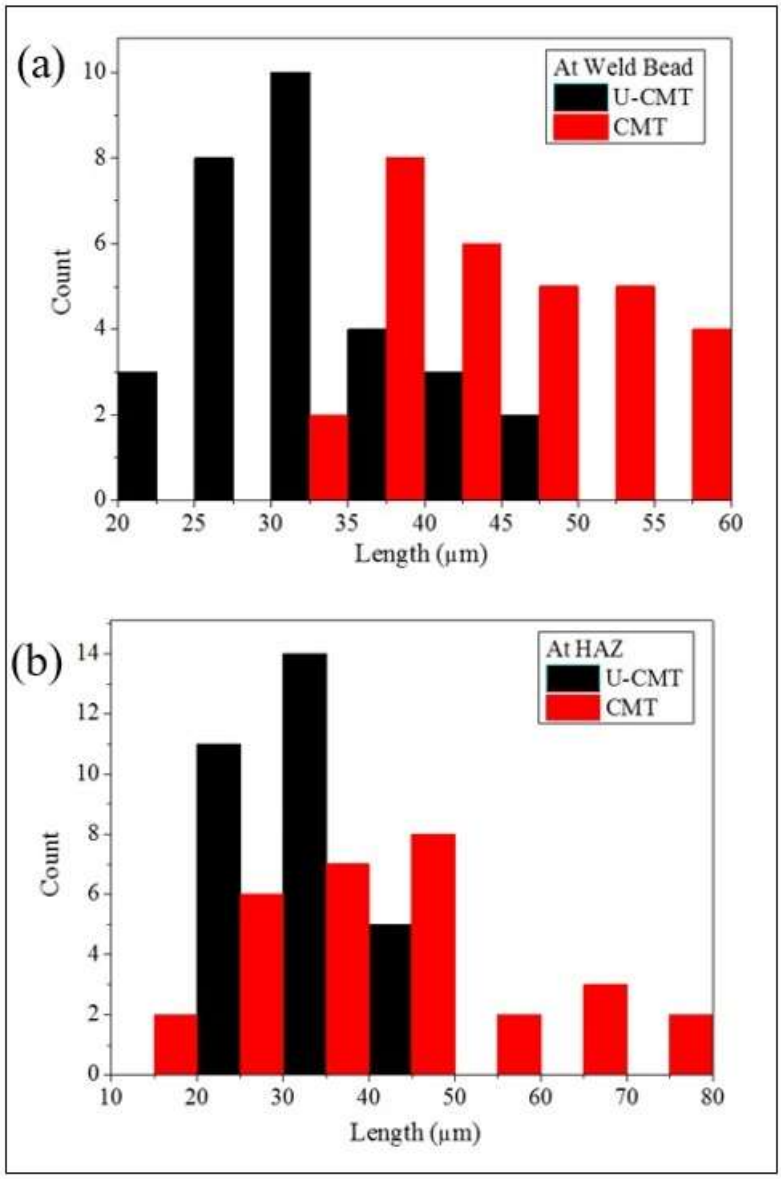

Fig. 5. 5 Grain size comparison for U-CMT and CMT samples at (a) Weld bead (b) HAZ

EDS analyses have been carried out in austenite (γ) and ferrite (δ) phases of CMT and U-CMT samples to analyses the content of main alloying elements. The points taken for EDS studies of CMT & U-CMT samples are shown in Fig. 5.7 (b) and (d), respectively. Fig. 5.8 shows the EDS analysis of welded samples. Table 5.1 exhibits the EDS results % w of Cr, Ni, and Fe contents in the CMT and U-CMT samples. With the employment of vibration, the difference in Cr content in the austenite and

ferrite region is reduced compared to without vibration sample. In addition, the Cr content in the ferrite region of the U-CMT sample is higher than the CMT sample. A similar trend of Ni content was also seen in the austenite region. The chances of Cr and Ni elements may be translated from filler wire to fusion region. The results revealed that ultrasonic vibration has a remarkable effect on the uniform distribution of alloying elements and refined microstructure.

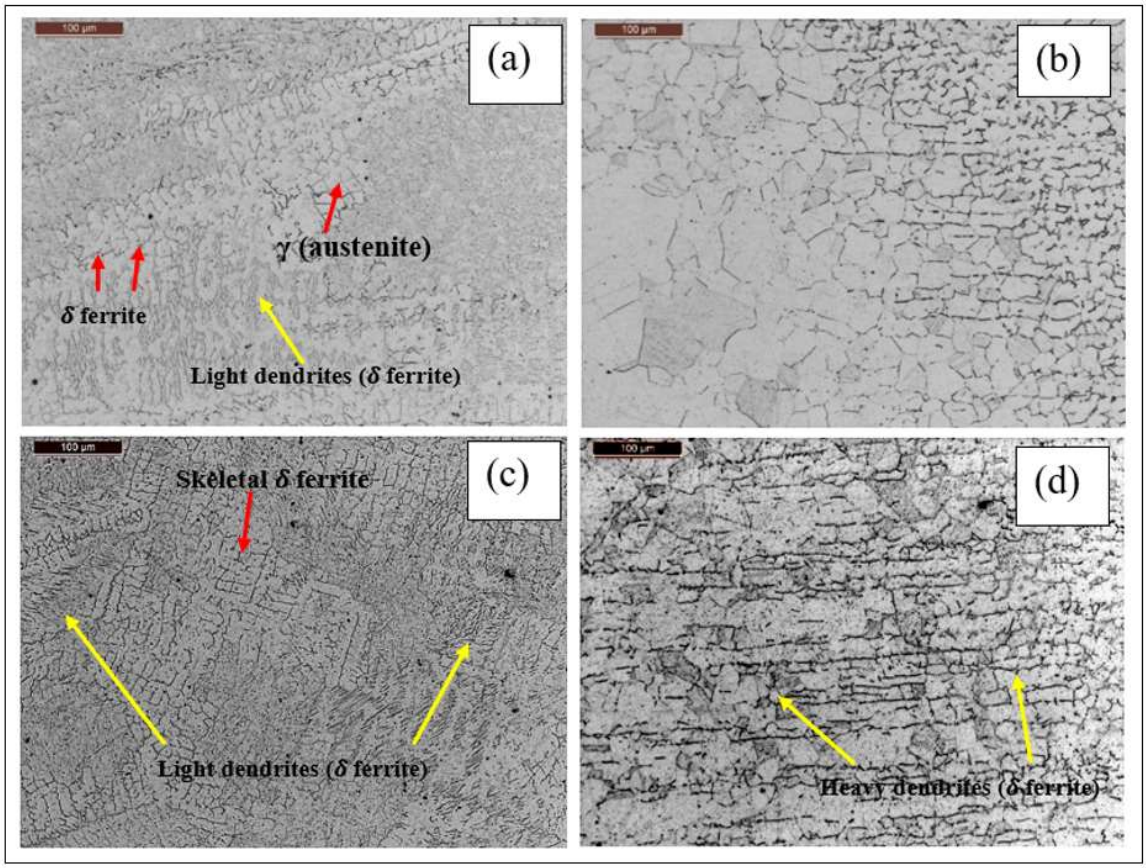

Fig. 5. 6 Microstructure of (a) Fusion region & (b) HAZ of sample 3 (U-CMT, 90A & 50µm) and (c) Fusion region & (d) HAZ of sample 4 (U-CMT, 90A & 99µm)

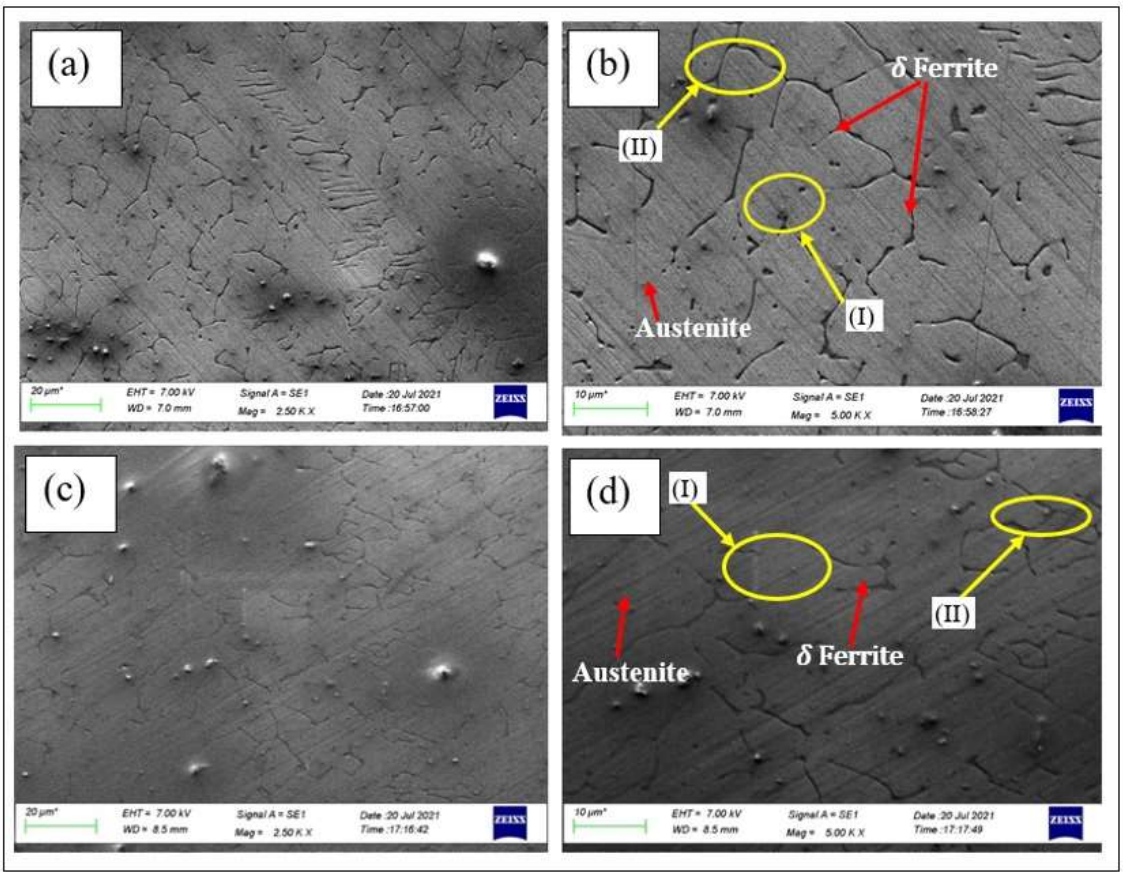

Fig. 5. 7 FESEM images of sample 5 (a) and sample 6 (c) and (b) and (d) are enlarged views

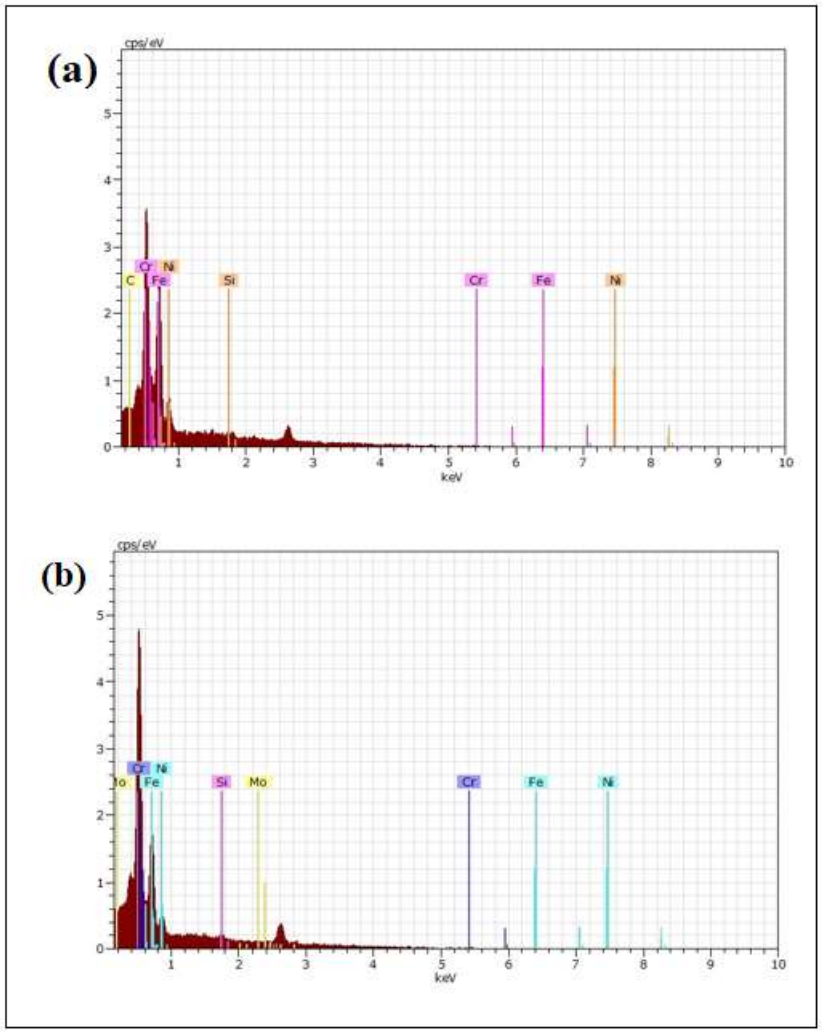

Fig. 5. 8 EDS analysis of sample 6 (U-CMT) taken at different regions in FESEM micrograph

Table 5. 1 EDS main elements in the SEM micrograph (Fig. 5.7) of CMT and U-CMT (in w%)

	Region	Cr	Ni	Fe
CMT	I	17.24	9.24	69.87
	II	21.46	7.68	70.88
U-CMT	I	19.77	10.86	65.94
	II	23.84	8.52	64.16

Fig. 5.9 shows the XRD pattern of base material and welded samples. In base material (Fig. 5.9 (a)), only austenite peaks were detected, and ferrite phases not detected due to smaller quantity may be present in the material, which XRD is not capable of detecting.

On the other hand, weld material consists of Austenite (Fe, C) and Ferrite phases. During solidification of the molten weld pool, the ferrite solidifies in the fusion region, and then transformation of ferrite to austenite takes place [Lan et al.,, (2020), Singh and Shahi (2018)]. The low heat input CMT process faster cooling occurs and having insufficient time to complete the phase transformation as a cause of ferrite retained in the fusion region which is seen in from Fig. 5.9 (b) & (c). In the welded samples, the intensity of the γ austenite plane has higher Cr enriched, and Ni depleted phases are formed [Balbande et al., (2019)]. With the employment of ultrasonic vibrations during welding, the different concentrations of Cr and Ni occur between these elements, and inter-diffusion occurs in ferrite and austenite phases. The various phases are detected by XRD in CMT welded samples are $Fe_{0.64}Ni_{0.35}$, $Cr_{0.19}Fe_{0.7}Ni_{0.11}$, $C_{0.09}Fe_{1.191}$ phases and in U-CMT welded samples are $Fe_{0.64}Ni_{0.35}$, $Cr_{0.19}Fe_{0.7}Ni_{0.11}$, $Cr_9Fe_{42}Mo_2Ti_5$.

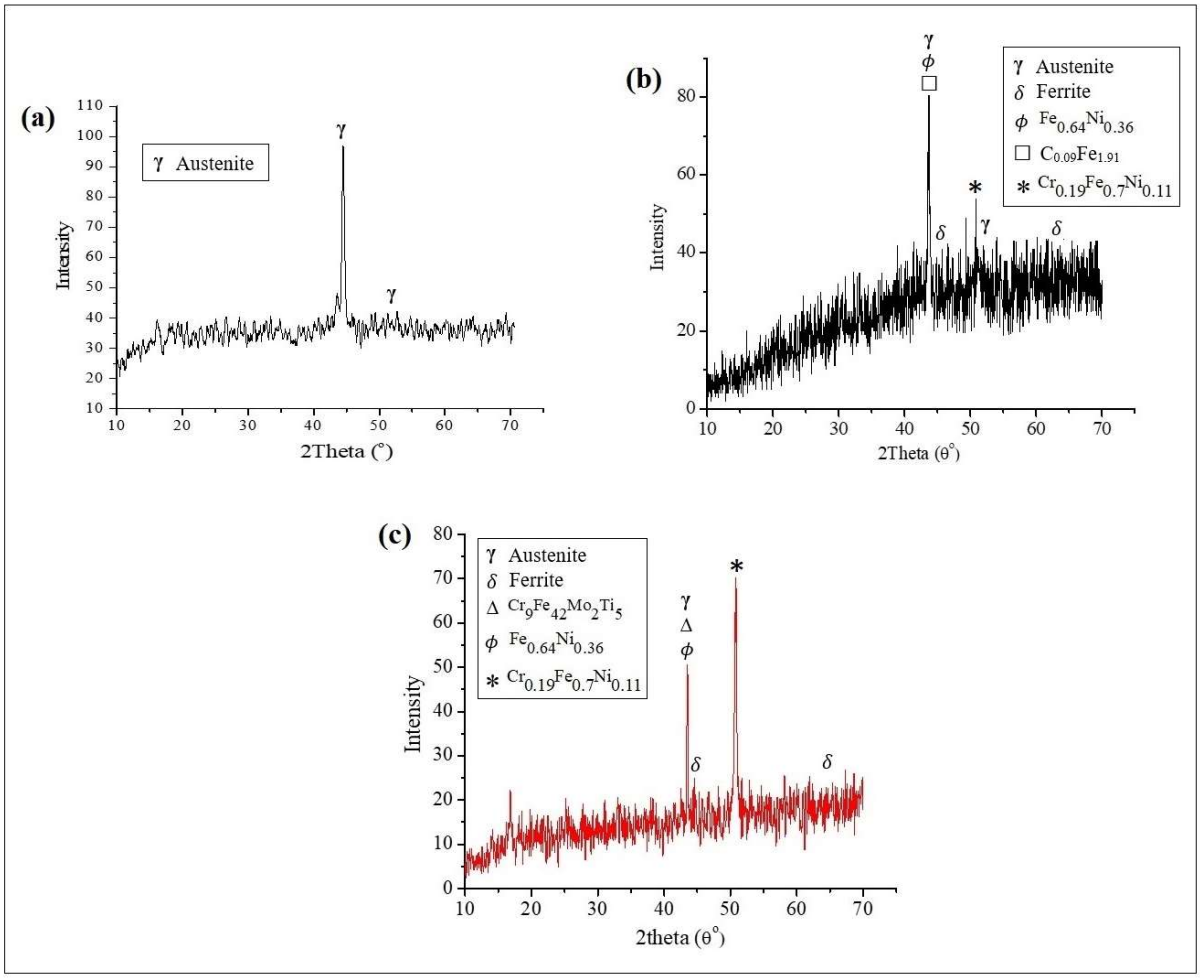

Fig. 5. 9 XRD plots of CMT and U-CMT welded samples

5.1.2 Effect of ultrasonic vibrations on the microhardness

The micro-hardness measurements of the CMT and U-CMT welded samples taken at various points are exhibited in Fig. 5.10. The micro-hardness evaluation of the CMT and U-CMT welded samples taken at the fusion region are exhibited in Table 5.1. Base material hardness is around 230HV. The increasing trend of microhardness value is

observed in the order of fusion region, HAZ, and base metal in welded samples, as seen in Fig. 5.11.

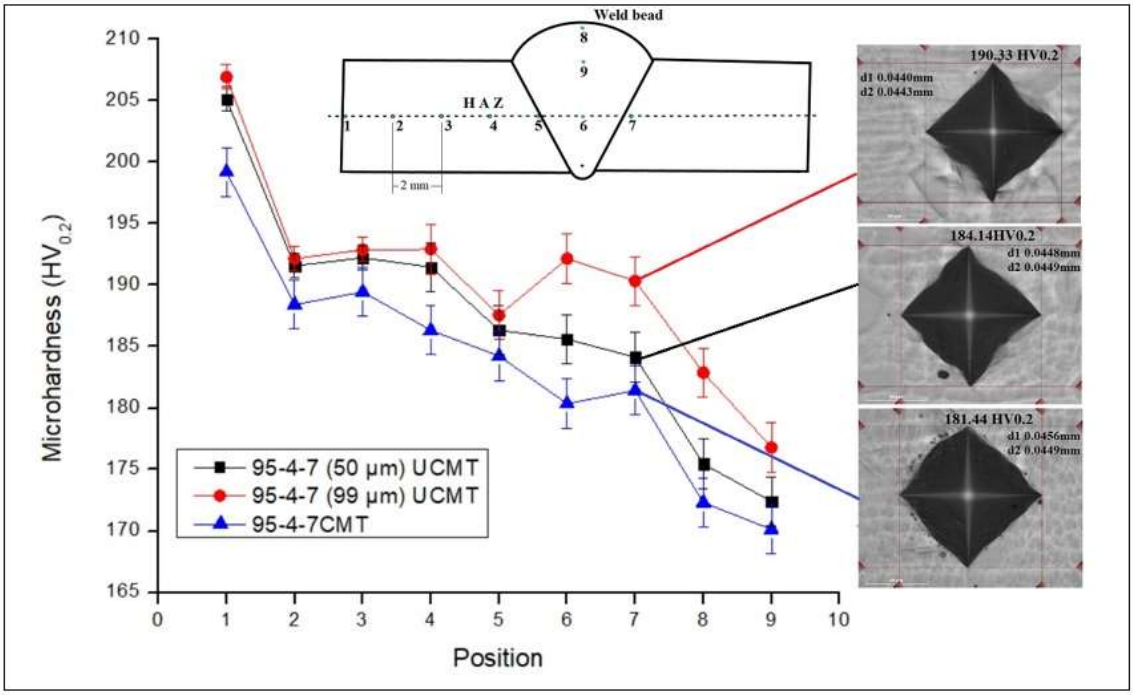

Fig. 5. 10 Micro-hardness variation of welded joints

Table 5. 2 Selected CMT & UCMT welding parameters and welded joint results

EXP NO	Weld Type	Current (A)	Ultrasonic Vibrational amplitude (µm)	UTS (MPa)	Elongation (%)	Joint efficiency (%)	Fusion region Microhardness (HV)
Sample 1	U-CMT	85	50	679	95.8	93.8	175.8
Sample 2	U-CMT	85	99	698	107	96.5	178.2
Sample 3	U-CMT	90	50	657	95.3	90.8	170.3
Sample 4	U-CMT	90	99	681	91.1	94.2	172.7
Sample 5	U-CMT	95	50	688	102	95.1	185.6
Sample 6	U-CMT	95	99	725	113	100	188.5
Sample 7	CMT	85	--	666	95	91	164.2
Sample 8	CMT	90	--	625	90.5	92	158.6
Sample 9	CMT	95	--	717	116	99.4	180.7

Minimum hardness was observed in the fusion region of all-welded samples. During welding, the heat causes the annealing effect in the fusion region, and recovery takes place for lesser hardness. In the HAZ, the tendency of hardness occurs due to a slow cooling rate in the fusion line; further grain growth occurs. However, near the base metal, a faster cooling rate occurs; therefore, finer grain may occur in the base metal [Kumar and Shahi, (2011)]. The hardness of U-CMT samples increases due to the refinement of grain size and decrease in δ-ferrite in the fusion region. In 304 SS weld material, Cr and Ni contents get atomic mobility due to increased ultrasonic vibration. Ni is quickly diffused in the austenite matrix and decreases in δ-ferrite phase. Hsieh et. al. (2014) reported a similar type of results for TIG welding of 304 SS with vibration. In the fusion region of U-CMT samples, grain refinement occurs due to ultrasonic vibration breaking the columnar grains for enhancement of hardness [Hsieh et. al., (2013)]. The ultra-sonication action generates many split dislocations in a hot molten weld pool which experiences higher hardness due to the work hardening effect of weld metal [Yu et al., (2019)]. Kolubaev et. al., (2020) reported that with the employment of vibrations, the grains of the steel welded joint are refined; as a result, a higher hardness is observed in the joint.

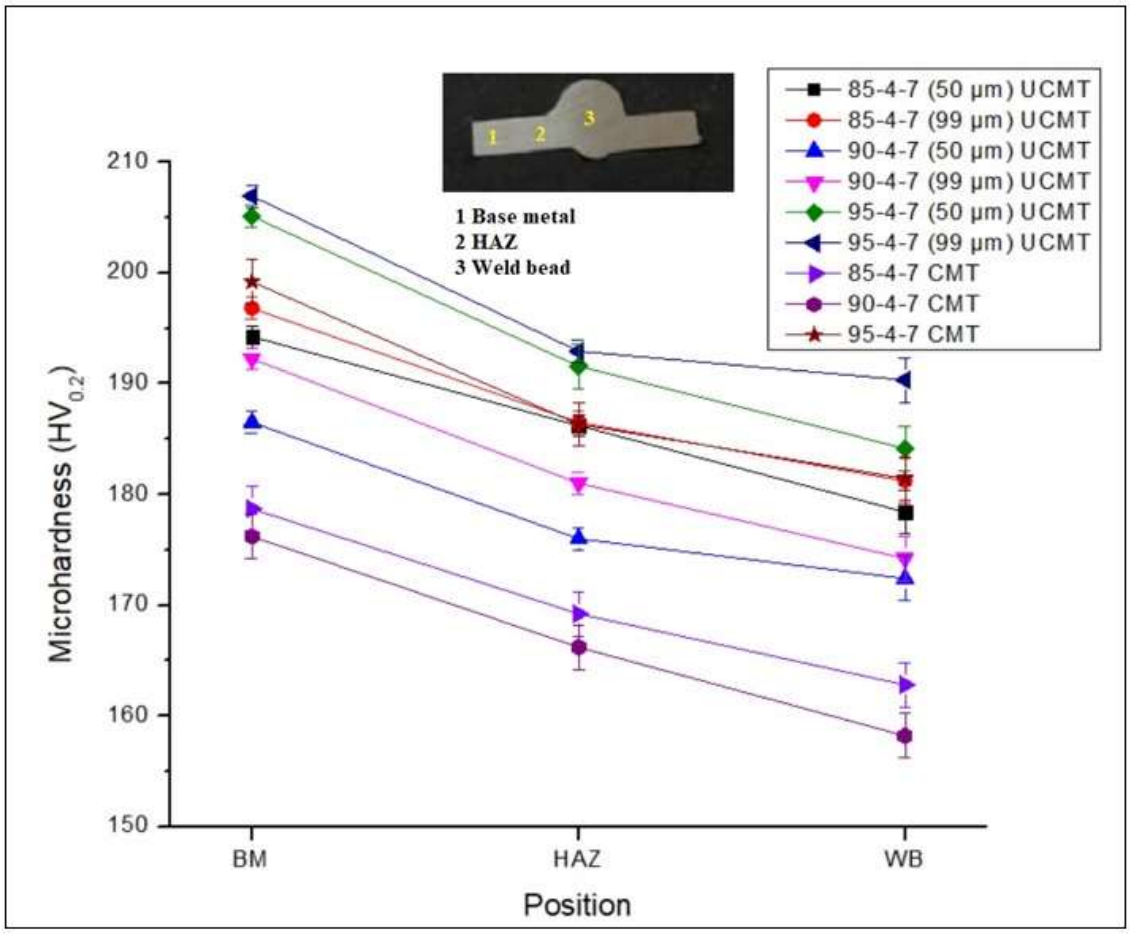

Fig. 5. 11 Microhardness of welded samples (a) Base Metal region (b) HAZ (c) Weld region

5.1.3 Effect of ultrasonic vibrations on tensile strength

Fig. 5.12 (a) and (b) shows the tensile samples before and after testing respectively. Typical Tensile stress-strain graphs of welded samples are shown in Fig. 5.13 Base material tensile strength and elongation are 723.3 MPa and 60%, respectively. The more significant tensile strength of U-CMT samples welded with 95A and vibrational amplitude of 99µm is 725 MPa, which is the marginal strength enhancement, and there is a significant improvement in elongation in comparison with CMT samples. In U-CMT samples, the strain gap is smaller inside the refined grains, and the grains form a uniform distribution, leading to lower fracturing of grains compared to coarser grains. The refined

grain size welded joint undergoes extensive deformation before it is broken and attain good elongation [Lan et. al., (2020)].

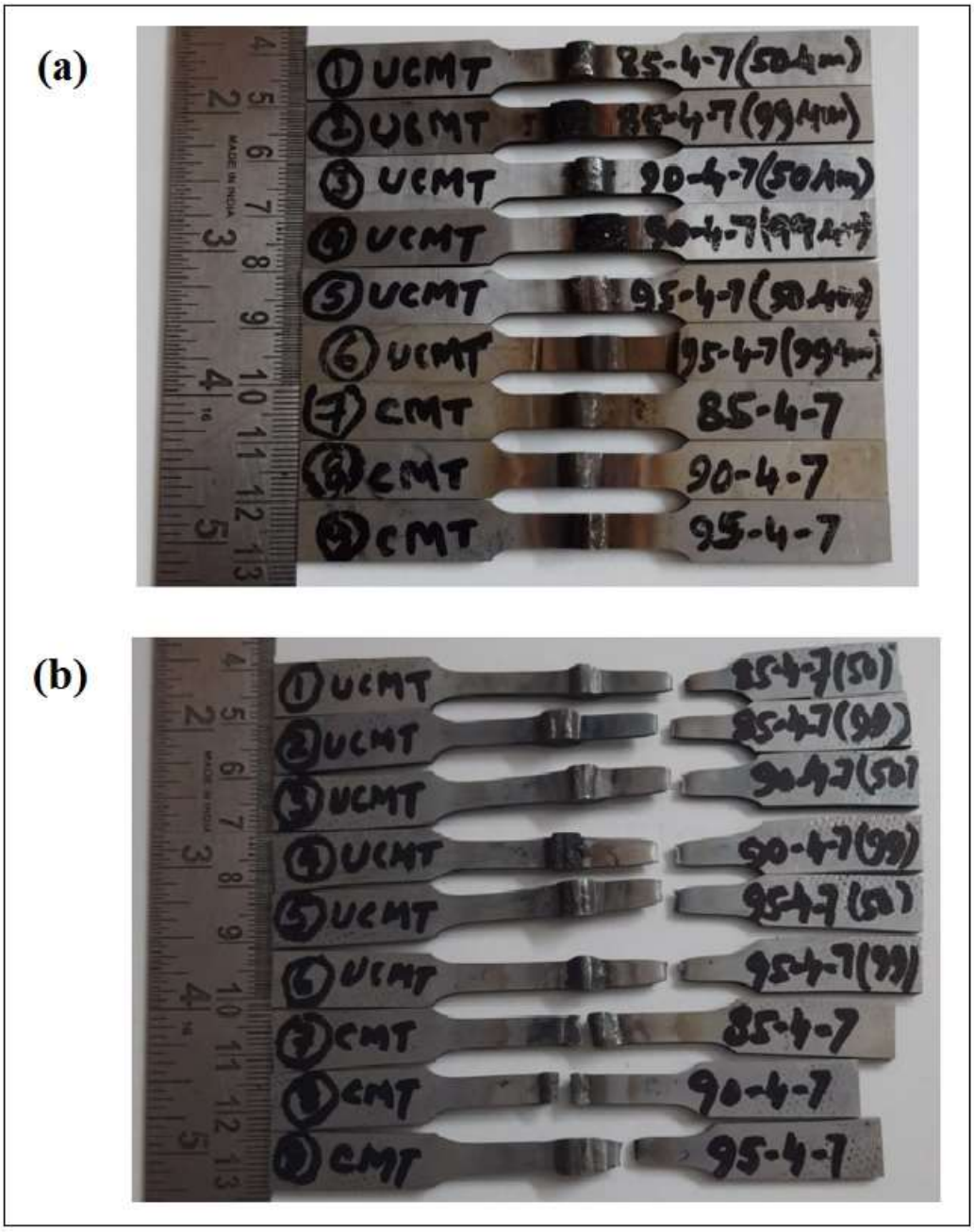

Fig. 5. 12 UCMT Tensile samples (a) Before testing (b) After tensile testing

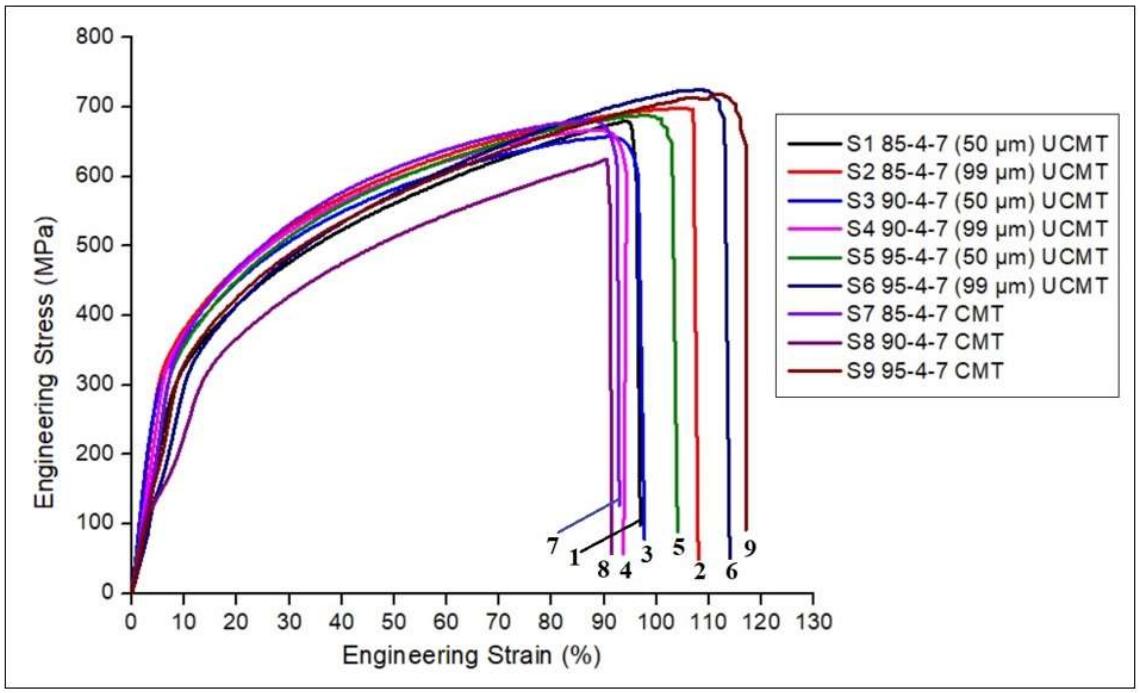

Fig. 5. 13 Stress-strain curves of welded samples

Welding current, speed, and contact to workpiece distance (CTWD) influence welding parameters for weld strength properties due to the evolution of appropriate heat input and deeper weld penetration [Koli et al., (2020b)]. The tensile test results are presented in Table 5.1. The reduction of weld strength material due to higher current generates more material melting. The fusion region material experiences smaller dendrites and lesser inter-dendrite regions at appropriate welding current [Yan et. al., (2010)]. At a higher current, the generation of heat input is to a greater extent, the welded material undergoes an increase in grain coarsening effect, which deteriorates the tensile properties. In addition, lower tensile strength joint experiences brittle intermetallic compounds in the fusion region and more extensive dendrites formation in HAZ. The CMT welded samples experiences lower tensile strength due owing to the formation of larger size dendrites and more inter-dendrite spacing in the fusion region. The broken tensile fractured surface of

CMT and U-CMT tested samples FESEM micrographs are exhibited in Fig. 5.14. Various sizes and shapes with dimples were observed in the fractured surfaces, which revealed the considerable fracture mechanism was ductile. A similar dimpled fractography with substantial precipitation was followed in welding 304 SS by Yan et. al., (2010). A higher amount of precipitation may affect the separation of grain boundaries, which reduces the tensile properties.

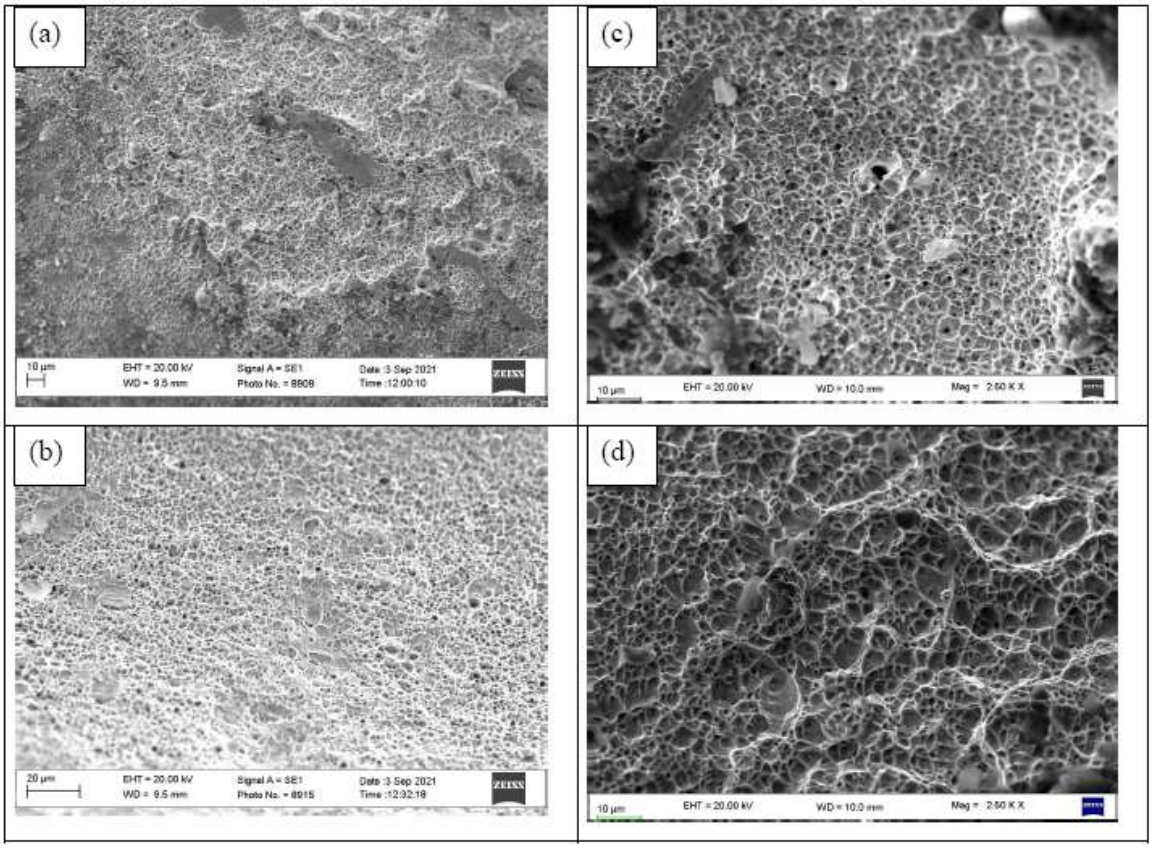

Fig. 5. 14 FESEM fractography of tensile fractured surface of (a) CMT sample -9 and (b) U-CMT sample-6, (c) and (d) are higher magnification views

5.1.4 Effect of ultrasonic vibrations on Residual Stress

During solidification of welded material, the top and bottom part of the fusion region cools rapidly compared to HAZ. Uneven temperature distribution occurs in the weldment owing to rapid heating and consecutive cooling, resulting in the evolution of residual stresses. The evolution of residual stress in welded joints is mainly controlled by the

metallurgical phase transformations and related microstructure, which impact the weld strength properties [Kumar et. al., (2021)]. During welding of thin steel plates, residual stresses may account for the development of distortion or buckling type welding defects [Eisazadeh and Aidun, (2021). By the application vibrations during welding, the generation of residual stress may be efficiently reduced to a large extent. The residual stress measurements are taken at the cross-section of welded samples at various regions, and the results are displayed in Fig. 5.15. The Fusion region has higher residual stress than other regions. U-CMT (95-4-7) sample 6 welded with 99 µm amplitude has lower residual stresses than other welded samples.

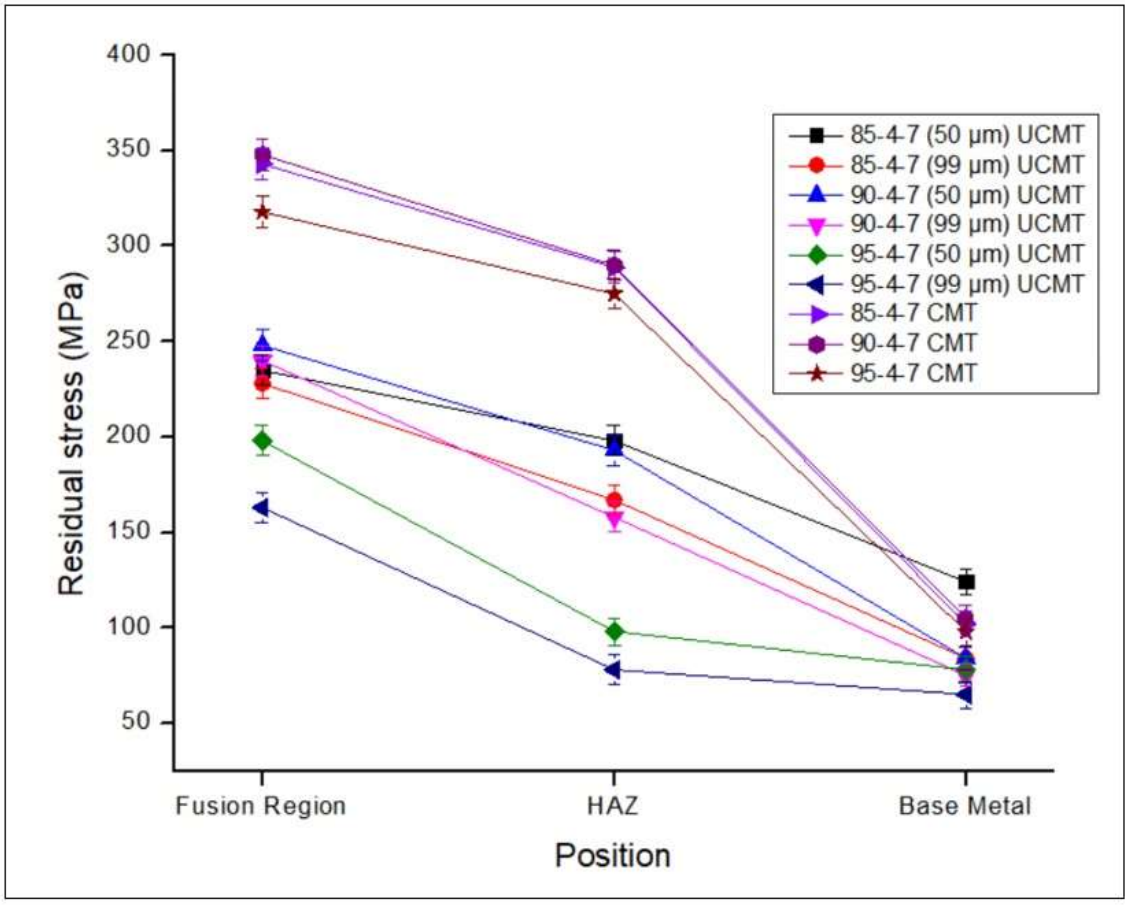

Fig. 5. 15 Residual Test results of welded samples taken at various points

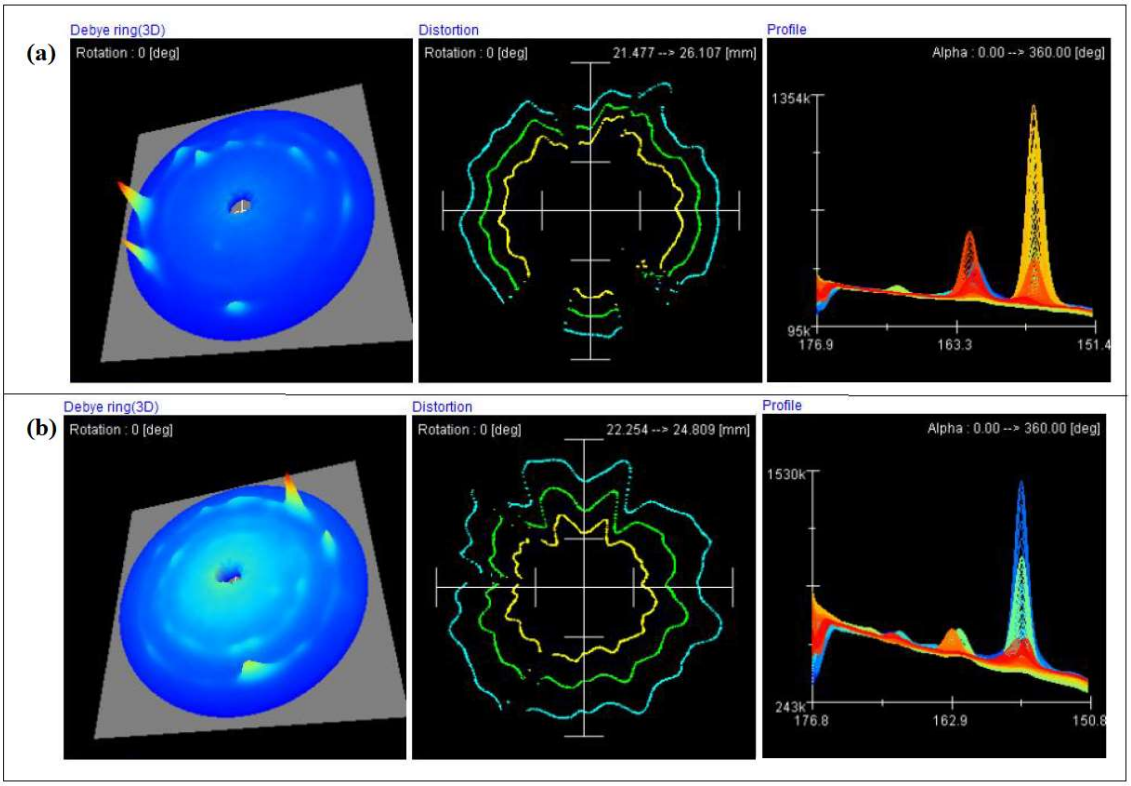

Fig. 5. 16 Residual stress distortion and profile curve of (a) Lower residual stress sample 6 and (b) Higher residual stress sample 8 at weld bead

Fig. 5.16 exhibits the Debye–Scherrer ring, distortion, and residual profile curve of welded samples. In the Debye-Scherrer ring, the red color shows more residual stresses in the tip, and the blue color shaded bottom indicates a minor concentration of residual stresses. A higher number of distortions was observed in the CMT sample due to the larger value of residual stresses, as seen from Fig. 5.16 (b). Aoki et. al., (2005), Qinghua et. al. (2008); Chuvas et. al., (2016) observed that residual stresses are reduced in the fusion region with vibration in comparison with the non-vibration welded joint. With the increase in vibrational amplitude, a higher number of residual stresses will be minimized compared to lower vibrational amplitude welded joints Hsieh et. al., (2013) reported that there is no notable development in residual stress relief of GMAW 304 SS welded joints with higher vibrational frequency. U-CMT sample has lower residual stresses with higher tensile

strength due to grain refinement occurring with vibration during welding, resulting in improved joint efficiency of the welded joint. The highest tensile strength obtained sample is taken to check the weld quality by NDT radiography inspection method as per ASTM SectionV:2017 standard. Fig. 5.17 distinctly shows that the welded joint does not consist of any welding defects such as incomplete penetration, cracks, incomplete fusion, and porosity. It reveals that the fabricated welded joint has a sound welded joint with quality.

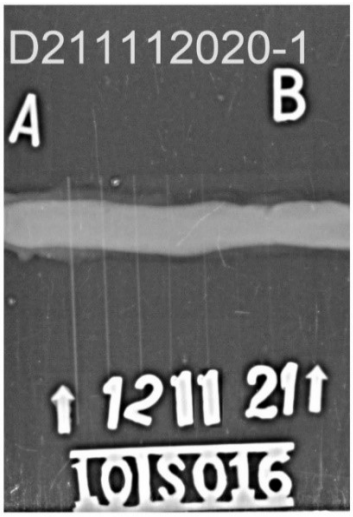

Fig. 5. 17 Radiography inspection test of U-CMT sample 6

5.3 SUMMARY

This chapter is based on a comparative analysis between CMT and U-CMT butt joints. Three welding currents are selected to fabricate welded joints; with ultrasonic and without vibrational assistance. Two different ultrasonic vibrational amplitudes are chosen to investigate the microstructural, microhardness, tensile properties, and residual stresses of welded joints. Results showed that ultrasonic vibrations during CMT welding improve grain refinement and enhance mechanical properties.

CHAPTER 6 : CONCLUSIONS AND SCOPE FOR FUTURE WORK

6.1 CONCLUSIONS

This chapter gives the main conclusions derived from the results and discussions from the above chapters.

6.1.1 CMT weld bead geometry

Initially, weld bead preliminary trials were performed on thin AISI 304 stainless steel to understand the effects of individual welding parameters on microhardness of the fusion region, weld bead geometry, and heat input. The preliminary trials helped decide the range and levels of welding parameters through the Taguchi L9 orthogonal array design matrix. The welding parameters such as welding current, welding speed, and CTWD are mainly used for finding maximum hardness and suitable weld bead geometry with higher filler metal penetration. Approximately 16% decrement in the microhardness is experienced in the HAZ and 25% decrement in weld region region, compared with the base material. The softening effect of material and the formation of courser grains are the main resons for decrement in hardness.

6.1.2 CMT weld Joint

For finding the maximum tensile properties of the CMT Butt welded joints of AISI 304 stainless-steel Response Surface Methodology with Box-Behnken model is used. The optimum input welding parameters produce (welding current of 92 A, a welding speed of 8 mm/sec, CTWD of 7 mm, and an arc correction factor of 0) tensile strength of 722 Mpa and % elongation of 93%. Tensile tests pertain to the joint efficiency in the range of 83.43

to 98.73% for appropriate all welded samples. The tensile fracture surface has dimpled morphology with lesser precipitation, significantly improving the mechanical properties. The radiography test result confirms the sound welded joint.

6.1.3 Ultrasonic-Assisted CMT Butt Joining

This chapter explains the application of ultrasonic vibrations during CMT welding. Various improvements are found in these studies for the enhancement of the quality of the weld. Excellent weld strength with more penetration exhibited in U-CMT samples with various welding parameters. The microstructure of the weld region consists of austenite and smaller δ-ferrite phases. With the application of vibrations, the equiaxed refined grains are formed, which enhancing the microstructural properties in the fusion region.

The microhardness of U-CMT samples is approximately a 16% increase in comparison with CMT welded samples at the same welding parameters due to grain refinement and work hardening effect. Tensile strength of 725MPa and ductility of 113% are attained with the vibration of CMT welded joints. Tensile fracture surface reveals fine dimpled morphology with micro and sub microvoids observed in U-CMT welded samples, indicating the weld joint's ductile failure. Significant reduction of residual stresses detected with vibration treatment during welding, which enhances joint efficiency without defects.

6.2 Scope For Future Work

- Various welding parameters such as filler wire, wire feed rate, gas flow rate, and other shielding gases can be studied.
- The welding of dissimilar alloys with activated flux can be explored.
- Robotic CMT can be employed for better accuracy for thin sheet joining of similar, dissimilar alloys.
- For joining of metal matrix composites and various alloys can be studied.
- Investigation of corrosion properties of the welded joint may be helpful for marine applications studies.
- The application of soft computing techniques and multi-criteria optimization techniques can be analyzed to find thermal analyses and process parameters during welding.

REFERENCES

[1] Ahmad, R., Bakar, M. A. (2011). Effect of a post-weld heat treatment on the mechanical and microstructure properties of AA6061 joints welded by the gas metal arc welding cold metal transfer method. Materials and Design, 32, 5120–5126.

[2] Ahsan, M. R, Cheepu, M., Ashiri, R., Kim, T. H., Jeong, C., Park, Y. D. (2017). Mechanisms of weld pool flow and slag formation location in cold metal transfer (CMT) gas metal arc welding (GMAW). Welding in the World, 61, 1275-1285.

[3] Ahsan, M. R., Kim, Y. R., Kim, C. H., Kim, J. W., Ashiri, R., Park, Y. D. (2016). Porosity formation mechanisms in cold metal transfer (CMT) gas metal arc welding (GMAW) of zinc coated steels. Science and Technology of Welding and Joining, 21, 209-215.

[4] Akbari, D., Sattari, F. (2009). Effect of the welding heat input on residual stresses in butt-welds of dissimilar pipe joints. International Journal of Pressure Vessel and Piping, 86, 769-776.

[5] Aoki, S., Nishimura, T., Hiroi, T. (2005). Reduction method for residual stress of welded joint using random vibration. Nuclear Engineering Design, 235, 1441-45.

[6] Babu, S., Panigrahi, S. K., Janaki Ram, G. D., Venkitakrishnan, P. V., Suresh Kumar, R. J. (2019) Materials Processing Technology, 266, 155.

[7] Baek, J.H., Kim, Y.P., Kim, W.S., Kho, Y.T. (2001). Fracture toughness and fatigue crack growth properties of the base metal and weld metal of a type 304 stainless steel pipeline for LNG transmission. International Journal of Pressure Vessel and Piping, 78, 351-357.

[8] Balbande, S., Taiwade, R.V., Patil, A.P., Pathak, U. (2019). Cold metal transfer welding of duplex with ferritic and super austenitic stainless steel. Materials Research Express, 6, 106542.

[9] Banik, S.D., Kumar, S., Singh, P.K. (2021). Distortion and residual stresses in thick plate weld joint of austenitic stainless steel: Experiments and analysis. Journal of Materials Processing Technology, 289, 116944.

[10] Benoit, A., Jobez, S., Paillard, P., Klosek, V., Baudin., T. (2011). Study of Inconel 718 weldability using MIG CMT process. Science Technology and Welding Joining, 16(6), 477–482.

[11] Cao, R., Feng, Z., Lin, Q., Chen, J. H. (2014). Study on cold metal transfer welding–brazing of titanium to copper. Materials and Design, 56, 165-173.

[12] Cao, R., Wen, B. F., Chen, J. H., Wang, P. C. (2013). Cold metal transfer joining of magnesium AZ31B-to-aluminum A6061-T6. Materials Science and Engineering: A, 560, 256-266.

[13] Chen, C., Fan, C., Cai, X., Lin, S., Yang, C., Zhuo, Y. (2020). Microstructure and mechanical properties of Q235 steel welded joint in pulsed and un-pulsed ultrasonic assisted gas tungsten arc welding. Journal of Materials Processing Technology, 275, 116335.

[14] Chen, C., Fan, C., Cai, X., Lin, S., Yang, C. (2019). Analysis of droplet transfer, weld formation and microstructure in Al-Cu alloy bead welding joint with pulsed ultrasonic-GMAW method. Journal of Materials Processing Technology, 271, 144-151.

[15] Chen, C., Fan, C., Lin, S., Cai, X., Zhou, L., Ye, S., Yang, C. (2018). Effect of ultrasonic pattern on weld appearance and droplet transfer in ultrasonic assisted MIG welding process Journal of Manufacturing Process, 35, 368-372.

[16] Chen, H., Guo, N., Zhang, Z., Liu, C., Zhou, L., Wang, G. (2020). A novel strategy for metal transfer controlling in underwater wet welding using ultrasonic-assisted method. Materials Letters, 270, 127692.

[17] Chen, M., Zhang, D., Wu, C. (2017a). Current waveform effects on CMT welding of mild steel, Journal of Materials Processing Technology, 243. 395–404.

[18] Chen, Q. H., Lin, S. B, Yang, C. L., Fan, C. L., Ge, H. L. (2016). Effect of ultrasound on heterogeneous nucleation in TIG welding of Al–Li alloy. Acta Metallurgica Sinica (English), 29(12), 1081-88.

[19] Chen, Q., Lin, S., Yang, C., Fan, C., Ge, H. (2017b). Grain fragmentation in ultrasonic-assisted TIG weld of pure aluminum. Ultrasonics Sonochemistry, 39, 403-413.

[20] Chuvas, T. C., Castello, D. A., Fonseca, M. P. C. (2016). Residual stress relief of welded joints by mechanical vibrations. Journal of Brazilian Society of Mechanical Science Engineering, 38, 2449-2457.

[21] Comez, N., Durmus, H. (2020). Corrosion behavior and mechanical properties of cold metal transfer welded dissimilar AA7075-AA5754 alloys. Journal of Central South University, 27, 18−26.

[22] Cong, B., Ouyang, R., Qi, B., Ding, J. (2016). Influence of Cold Metal Transfer Process and Its Heat Input on Weld Bead Geometry and Porosity of Aluminum-Copper Alloy Welds. Rare Metal Materials and Engineering, 45(3), 606-611.

[23] Cornacchia, G., Cecchel, S., Panvini, A. (2018). A comparative study of mechanical properties of metal inert gas (MIG)-cold metal transfer (CMT) and fiber laser-MIG hybrid welds for 6005A T6 extruded sheet. International Journal of Advanced Manufacturing Technology, 94, 2017–2030.

[24] Costanza, G., Sili, A., Tata, M.E. (2016). Weldability of austenitic stainless steel by metal arc welding with different shielding gas. Procedia Structural integrity, 2, 3508-3514.

[25] Dai, W. L. (2003). Effects of high-intensity ultrasonic-wave emission on the weldability of aluminum alloy 7075-T6. Materials Letters, 57, 2447-2454

[26] Dak, G., Pandey, C. (2020). A critical review on dissimilar welds joint between martensitic and austenitic steel for power plant application. Journal of Manufacturing Process, 58, 377-406.

[27] Dharmik, Y. B., Lautre, N. K. (2020). Performance Assessment of CMT over GTA welding on stacked thin sheets of CRNGO Electrical steel. Materials Letters,127901.

[28] Dhobale, A. L., Mishra, H. K. (2015). Review on effect of heat input on tensile strength of butt weld joint using MIG welding. International Journal of Innovations in Engineering Research and Technology, 2(9), 1-13.

[29] Dos Santos, E.B.F., Kuroiwa, L.H., Ferreira, F.C., Pistor, R., Gerlich, A. (2017). On the Visualization of Gas Metal Arc Welding Plasma and the Relationship Between Arc Length and Voltage, Applied Science, 7(5), 503.

[30] Dutra, J.C., Silva., R.H.G., Savi, B.M., Marques, C., Alarcon, O.E. (2015). Metallurgical characterization of the 5083H116 aluminum alloy welded with the cold metal transfer process and two different wire-electrodes (5183 and 5087). Welding in the World, 59, 797–807.

[31] Eisazadeh H, Aidun, D. K. (2021). Residual stress reduction in dissimilar metals weld. Journal of Manufacturing Process, 64, 1462–1475.

[32] Elrefaey, A. (2015). Effectiveness of cold metal transfer process for welding 7075 aluminium alloys. Science and Technology of Welding and Joining, 20, 280-285.

[33] Fan, F., Zhou, L., Liu, Z., Yang, C., Lin, S., Xie, W., Tong, H. (2018). Arc character and droplet transfer of pulsed ultrasonic wave-assisted GMAW. The International Journal of Advanced Manufacturing Technology, 95, 2219-2226.

[34] Fattahi, M., Ghaheri, A., Arabian, N., Amirkhanlu, F., Moayedi, H. (2020). Applying the ultrasonic vibration during TIG welding as a promising approach for the development of nanoparticle dispersion

strengthened aluminum weldments. Journal of Materials Processing Technology, 282, 116672.

[35] Feng, J., Zhang, H., He, P. (2009). The CMT short-circuiting metal transfer process and its use in thin aluminium sheets welding. Materials and Design, 30, 1850-1852.

[36] Feng-yuan, SHU., Ze, TIAN., Yao-hui, LU., Wen-xiong. HE., Fei-yang, LU., Jian-jun, LIN., Hong-yun, ZHAO., Bin-shi, XU. (2015). Prediction of vulnerable zones based on residual stress and microstructure in CMT welded aluminum alloy joint. Transactions of Nonferrous Metals Society of China, 25, 2701−2707.

[37] Gadallah, R., Tsutsumi, S., Aoki Y., Fuji, H. (2021). Investigation of residual stress within linear friction welded steel sheets by alternating pressure via X-ray diffraction and contour method approaches. Journal of Manufacturing Process, 64, 1223-1234.

[38] Ghosh, P.K., Dorn, Lutz., Kulkarni, Shrirang., Hofmann, F. (2009). Arc characteristics and behaviour of metal transfer in pulsed current GMA welding of stainless steel. Journal of materials processing Technology, 209, 1262-1274.

[39] Girinath, B., Siva Shanmugam, N., Sankaranarayanasamy, K. (2019). Investigation on the Effect of Torch Angle on the Formability of AA5052 CMT Weldments, Transactions of Indian Institute of Metals, 72, 1551-1555.

[40] Gorunov, A. I., Nyukhlaev, O. A, Kh, A. (2018). Investigation of microstructure and properties of low-carbon steel during ultrasonic-

assisted laser welding and cladding. The International Journal of Advanced Manufacturing Technology, 99, 2467-2479.

[41] Goyal, H., Mandal, N., Roy, H., Mitra, S. K., Mondal, B. (2015). Multi response optimization for processing Al–SiCp composites: an approach towards enhancement of mechanical properties. Transactions of the Indian Institute of Metals, 68(3), 453-463.

[42] Hsieh, C., Lai, C., Wu, W. (2013). Effect of Vibration on Microstructures and Mechanical Properties of 304 Stainless Steel GTA Welds. Metals Materials International, 19, 835-844.

[43] Hsieh, C., Wang, P., Wang, J., Wu, W. (2014). Evolution of Microstructure and Residual Stress under Various Vibration Modes in 304 Stainless Steel Welds. The Scientific World Journal, 895790 http://dx.doi.org/10.1155/2014/895790.

[44] Hu, S., Zhang, H., Wang, Z., Liang, Y., Liua, Y. (2016). The arc characteristics of cold metal transfer welding with AZ31magnesium alloy. Journal of Manufacturing Processes, 24, 298–306.

[45] Hua, C., Lua, H., Yu, C., Chen, J., Wei, X., Xu, J. (2017). Reduction of ductility-dip cracking susceptibility by ultrasonic-assisted GTAW. Journal of Materials Processing Technology, 239, 240-250

[46] Huan, P. C., Wang, X. N., Zhang, J., Hu, Z. R., Chen, W. G., Nagaumi, H., Di, H. S. (2020). Effect of wire composition on microstructure and properties of 6063 aluminium alloy hybrid synchronous pulse CMT welded joints. Materials Science and Engineering: A, 790, 139713.

[47] Ibrahim, I. A., Mohamat, S. A., Amir, A., Ghalib, A. (2012). The Effect of Gas Metal Arc Welding (GMAW) processes on different welding parameters. Procedia Engineering, 41, 1502-1506.

[48] Irizalp, A. O., Durmus, H., Yuksel, N., Turkmen, I. (2016). Cold metal transfer welding of AA1050 aluminum thin sheets. Revista Materia, 11730, 615-622.

[49] Jan, F., Kaplan, A. F. H., Lamas, J. (2014). Comparison of CMT with other arc modes for laser-arc hybrid welding of steel. Welding in the World, 58, 649-660.

[50] Jha, A. K., Diwakar, V., Sreekumar, K. (2003). Stress corrosion cracking of stainless-steel bellows of satellite launch vehicle propellant tank assembly. Engineering Failure Analysis, 10, 699-709.

[51] Jin, J., Lu, Q., Zhang, P., Li, C., Yan, H. (2020). Research on Microstructure and Fatigue Properties of Vibration-Assisted 5052 Aluminum Alloy Laser Welded Joints. Journal of Materials Engineering Performance, 29, 4197-41205.

[52] Jose, M. J, Kumar, S. S., Sharma, A. (2016). Vibration assisted welding processes and their influence on quality of welds. Science Technology Welding Joining, 21, 243-258.

[53] Kannan, A. R., Rajesh, N., Shanmugam, N. S., Naveenkumar, S. (2019 a). Effect of arc length correction on weld bead geometry and mechanical

properties of AISI 316L weldments by cold metal transfer (CMT) process. Materials Today Proceedings, 18, 3916-3921.

[54] Kannan, A. R., Shanmugam, N. S., Vendan, S. A. (2019 b). Effect of cold metal transfer process parameters on microstructural evolution and mechanical properties of AISI 316L tailor welded blanks. International Journal of Advanced Manufacturing Technology, 103, 4265-4282.

[55] Koli, Y., Yuvaraj, N., Vipin, Aravindan, S. (2020b). Investigations on weld bead geometry and microstructure in CMT, MIG pulse synergic and MIG welding of AA6061-T6. Materials Research Express, 6, 265e5.

[56] Kolubaev, A. V., Sizova, O. V., Fortuna, S. V., Vorontsov, A. V., Ivanov, A. N., Kolubaev, E. A. (2020). Weld structure of low-carbon structural steel formed by ultrasonic-assisted laser welding. Journal of Constructional Steel Research, 172, 106190.

[57] Kumar, B., Bag, S., Mahadevan, S., Paul, C. P, Das, C. R, Bindra, K. S. (2021). On the interaction of microstructural morphology with residual stress in fiber laser welding of austenitic stainless steel. CIRP Journal of Manufacturing Science Technology, 33, 158-175.

[58] Kumar, N. P., Vendan, S. A., Shanmugam, N. S. (2016). Investigations on the parametric effects of cold metal transfer process on the microstructural aspects in AA6061. Journal of Alloys and Compounds, 658, 255-264.

[59] Kumar, S., Shahi, A. S. (2011). Effect of heat input on the microstructure and mechanical properties of gas tungsten arc welded AISI 304 stainless steel joints. Materials and Design, 32, 3617-3623.

[60] Kumar, S., Shahi, A. S. (2016). Studies on metallurgical and impact toughness behavior of variably sensitized weld metal and heat-affected zone of AISI 304L welds. Materials and Design, 89, 399-412.

[61] Kumar, S., Wu, C. S., Padhy, G. K., Ding, W. (2017). Application of ultrasonic vibrations in welding and metal processing: A status review. Journal of Manufacturing Process, 26, 295-322.

[62] Kuo, C-W., Yang, S-M., Chen, J-H., Lai, G-H., Wu, W. (2008). Study of vibration welding mechanism, Science and Technology of Welding and Joining, 13(4), 357–362.

[63] Lai, H., Wu, W. (2020). Practical examination of the welding residual stress in view of low-carbon steel welds. Journal of Materials Research and Technology, 9, 2717-2726.

[64] Lan, H., Gong, X., Zhang, S., Wang, L., Wang, B., Nie, L. (2020) Ultrasonic vibration assisted tungsten inert gas welding of dissimilar metals 316L and L415. International Journal of Minerals, Metallurgy and Materials, 27, 943-953.

[65] Lei, H., Li, Y., Carlson, B. (2017). Cold metal transfer spot welding of 1 mm thick AA6061-T6. Journal of Manufacturing Processes, 28, 209–219.

[66] Leo, P., Ostuni, D., Casalino, G. (2016). Hybrid welding of AA5754 annealed alloy: Role of post weld heat treatment on microstructure and mechanical properties. Materials and Design, 90, 777–786.

[67] Li, G., Zhang, C., Gao, M., Zeng, X. (2014). Role of arc mode in laser-metal active gas arc hybrid welding of mild Steel. Materials and Design, 61, 239-250.

[68] Li, Y., Tian, S., Wu, C., Tanaka, M. (2021). Experimental sensing of molten flow velocity, weld pool and keyhole geometries in ultrasonic-assisted plasma arc welding. Journal of Manufacturing Processes, 64, 1412-1419.

[69] Liang, Y., Hu, S., Shen, J., Zhang, H., Wang, P. (2017). Geometrical and microstructural characteristics of the TIG-CMT hybrid welding in 6061 aluminum alloy cladding. Journal of Materials Processing Technology, 239, 18-30.

[70] Liang, Y., Shena, J., Hua, S., Wanga, H., Panga, J. (2018). Effect of TIG current on microstructural and mechanical properties of 6061- T6 aluminium alloy joints by TIG–CMT hybrid welding. Journal of Materials Processing Technology. 255, 161–174.

[71] Lin, J., Ma, N., Lei, Y., Murakawa, H. (2013). Shear strength of CMT brazed lap joints between aluminum and zinc-coated steel. Journal of materials processing technology, 213(8), 1303-1310.

[72] Liu, A., Tang, X., Lu, F. Study on welding process and prosperities of AA5754 Al-alloy welded by double pulsed gas metal arc welding, Materials and Design 50 (2013) 149–155.

[73] Liu, H., Yanga, S., Xie, C., Zhang, Q., Cao, Y. (2017). Microstructure characterization and mechanism of fatigue crack initiation near pores for

6005A CMT welded joint. Materials Science and Engineering A, 707, 22–29.

[74] Loayza, C. R. L., Borges, D. J. A., Cardoso, D. C. S., Assuncao, P. D. C., Ferreira, V. O., Baia, P. E. C., Castro, A. A. F., Reis, M. A. L., Braga, E. M. (2019). A new approach for the reinforcement of SS 304L via arc welding: Using nanostructured flux cored electrode. Diamond and Related Materials, 92, 138-145.

[75] Luchten-Berg, P., Campos, P. T., Soares, P., Laurindo, C. A. H., Maranho, O., Torres, R. D. (2019). Effect of welding energy on the corrosion and tribological properties of duplex stainless-steel weld overlay deposited by GMAW/CMT process. Surface and Coatings Technology, 375, 688-693.

[76] Madhavan, S., Kamraj, M., Vijayaraghavan, L., Rao, K. S. (2017). Cold Metal Transfer welding of Dissimilar A6061 Aluminium Alloy-AZ31B Magnesium Alloy: Effect of Heat Input on Microstructure, Residual Stress and Corrosion Behavior. Transactions of Indian Institute of Metals, 70, 1047-1054.

[77] Meena, L. S., Butola, R., Murtaza, Q., Jayantilal, H., Niranjan, M.S. (2017). Metallurgical investigation of microstructure and microhardness across the various zones in synergic MIG welding of stainless steel. Materials today proceedings, 4, 8240-8249.

[78] Mehrani, M. A., Paidar, M., Khodabandeh, A., Nategh, S. (2016). Influence of filler wire and wire feed speed on metallurgical and mechanical properties of MIG welding–brazing of automotive galvanized

steel/5754 aluminum alloy in a lap joint configuration. The International Journal of Advanced Manufacturing Technology, 82, 1495-1506.

[79] Mirshekari, G. R., Tavakoli, E., Atapour, M., Sadeghian, B. (2014). Microstructure and corrosion behavior of multipass gas tungsten arc welded 304L stainless steel. Materials and Design, 55, 905-911.

[80] Mohammad, R., Rao, M., Rao, S. (2017). Welding of nickel free high nitrogen stainless steel: Microstructure and mechanical properties. Defence Technology, 13, 59-71.

[81] Mou, G., Hua, X., Wang, M., Lia., F. (2019). Effects of Ni addition on removing Fe-Ti intermetallic compounds in cold metal transfer arc-brazed TC4/304L dissimilar joints. Journal of Manufacturing Processes, 38, 104-112.

[82] Ning, F., Cong, W. (2016). Microstructures and mechanical properties of Fe-Cr stainless steel parts fabricated by ultrasonic vibration-assisted laser engineered net shaping process. Materials Letters, 179, 61-64.

[83] Okagawa, R. K., Dixon, R. D., Olson, D.L. (1982). The influence of nitrogen from welding on stainless steel weld metal microstructures. 63rd AWS Annual Meeting held at Kausa City, Missouri, April 26-30.

[84] Ola, O.T., Doern, F.E. (2014). A study of cold metal transfer clads in nickel-base INCONEL 718 superalloy. Materials and Design, 57, 51–59.

[85] Ou, Y., Lu, O., Li, C., Yan, H., Zhang, P., Jin, J. (2021). Effect of Vibration Frequency on Microstructure and Properties of Laser-Welded

Inconel 718 Nickel-Base Superalloy. Journal of Materials Engineering Performance, 30, 2399-407.

[86] Pandey, C. (2020). Mechanical and Metallurgical Characterization of Dissimilar P92/SS304 L Welded Joints Under Varying Heat Treatment Regimes. Metallurgical and Materials Transactions A, 51A, 2126-42.

[87] Pandey, C., Mahapatra, M. M., Kumar, P., Saini, N. (2018). Effect of Weld Consumable Conditioning on the Diffusible Hydrogen and Subsequent Residual Stress and Flexural Strength of Multipass Welded P91 Steels. Metallurgical and Materials Transactions B, 49B, 2881-2895.

[88] Pandey, C., Saini, N., Mahapatra, M. M., Kumar. P. (2017). Study of the fracture surface morphology of impact and tensile tested cast and forged (C&F) Grade 91 steel at room temperature for different heat treatment regimes. Engineering Failure Analysis, 71, 131-147.

[89] Pang, J., Hu, S., Shen, J., Wang, P., Liang, Y. (2016). Arc characteristics and metal transfer behavior of CMT + P welding process. Journal of Materials Processing Technology, 238, 212–217.

[90] Pavan Kumar, N., Vendan, A., Siva Shanmugam, N. (2016). Investigations on the parametric effects of cold metal transfer process on the microstructural aspects in AA606. Journal of Alloys and Compounds, 658, 255e264.

[91] Phillip, J. R. (1988). Taguchi techniques for quality engineering. Mc Graw-Hill, New York.

[92] Pickin, C. G., Williams, S. W., Lunt, M. (2011). Characterization of the cold metal transfer (CMT) process and its application for low dilution cladding. Journal of Materials Processing Technology, 211(3), 496-502.

[93] Pickin, C. G., Young, K. (2013). Evaluation of cold metal transfer (CMT) process for welding aluminium alloy. Science and Technology of Welding and Joining, 11, 583-585.

[94] Posch, G., Chaladil K., Chladil, H. (2017). Material properties of CMT-metal additive manufactured duplex stainless steel blade-like geometries. Welding in the World, 61, 873-882.

[95] Qinghua, L., Ligong, C., Chunzhen, N. (2008). Effect of vibratory weld conditioning on welded valve properties. Mechanics of Material, 40, 565-574.

[96] Ragu Nathan, S., Balasubramanian, V., Malarvizhi, S., Rao, A. G. (2015). Effect of welding processes on mechanical and microstructural characteristics of high strength low alloy naval grade steel joints. Defence Technology, 11, 308-317.

[97] Rajeev, G. P., Kamaraj, M., Srinivasa, R., Bakshi. (2019). Effect of correction parameters on deposition characteristics in cold metal transfer welding. Materials and Manufacturing Processes, 34(11), 1205-1216.

[98] Rossini, N. S, Dassisti, M., Benyounis, K. Y., Olabi, A. G. (2012). Methods of measuring residual stresses in components. Materials and Design, 35, 572-588.

[99] Satyanarayana, V. V., Reddy, G. M., Mohandas, T. (2005). Dissimilar metal friction welding of austenitic–ferritic stainless steels. Journal of Materials Processing Technology, 160(2), 128-137.

[100] Selvi, S.A, Vishvaksenan, E., Rajasekar, (2017). Cold metal transfer (CMT) technology-An overview. Defence Technology, 14(1), 1-17.

[101] Singh, D. K., Sahoo, G., Basu, R., Sharma, V. Mohtadi-Bonab, M. A. (2018). Investigation on the microstructure—mechanical property correlation in dissimilar steel welds of stainless steel SS 304 and medium carbon steel EN 8. Journal of Manufacturing Processes, 36, 281-292.

[102] Singh, J. Shahi, A. S. (2018). Weld joint design and thermal ageing influence on the metallurgical, sensitization and pitting corrosion behavior of AISI 304L stainless steel welds. Journal of Manufacturing Processes, 33, 126-135.

[103] Sridhar, P. V. S. S., Biswas, P., Mahanta, P. (2020). Effect of process parameters on bead geometry, tensile and microstructural properties of double-sided butt submerged arc welding of SS 304 austenitic stainless steel, Journal of Brazilian Society of Mechanical Sciences and Engineering, 42, 551.

[104] Stanciu, E. M., Pascu, A., Gheorghiu, I. (2017). CMT Welding of Low Carbon Steel Thin Sheets. In IOP Conference Series. Materials Science Engineering, 209, 012051.

[105] Sun, Q. J., Lin, S.B., Yang, C.L., Zhao, G.Q. (2009). Penetration increase of AISI 304 using ultrasonic assisted tungsten inert gas welding. Science and Technology Welding Joining, 65, 767.

[106] Tang, Y. L., Ye, X., Ding, L. C., Zhang, P. L., Yu, Z. S., Yang, S. L, Wu, D., Fu, K. (2020). High-temperature tensile properties and interface structure of NiFe dissimilar butt joints welded using the cold metal transfer process. Journal of Materials Research and Technology, 9(6), 5023-15033.

[107] Taraphdar, P. K., Pandey, C., Mahapatra, M. M. (2020). Finite element investigation of IGSCC-prone zone in AISI 304L multipass groove welds. Archives of Civil and Mechanical Engineering, 20, 54.

[108] Taraphdar, P. K., Thakare, J. G., Pandey, C., Mahapatra, M. M. (2020a). Novel residual stress measurement technique to evaluate through thickness residual stress fields. Materials Letters, 277, 128347.

[109] Tian, Y., Shen, J., Hu, S., Wang, Z., Gou, J. (2018). Effects of ultrasonic vibration in the CMT process on welded joints of Al alloy. Journal of Materials Processing Technology, 259, 282-291.

[110] Wang, P., Hu, S., Shena, J., Liang, Y. (2017). Characterization the contribution and limitation of the characteristic processing parameters in cold metal transfer deposition of an Al alloy. Journal of Materials Processing Technology, 245, 122–133.

[111] Wang, Y., Yu, C., Lu, H., Chen, J. (2020). Research status and future perspectives on ultrasonic arc welding technique. Journal of Manufacturing Processes, 58, 936-954.

[112] Watanabe, T., Shiroki, M., Yanagisawa, A., Sasaki, T. (2010). Improvement of mechanical properties of ferritic stainless steel weld

metal by ultrasonic vibration. Journal of Materials Processing Technology, 210, 1646-1651.

[113] Wei, B. (1992). Unidirectional dendritic solidification under longitudinal resonant vibration. Acta Metallurgica et Materialia, 40(10), 2739–2751.

[114] Xu, P., Hua, X., Chena, N., Moua, G., Jia, X., Li, F. (2020). Effect of the microstructure of IMCs and zinc accumulation on the mechanical properties of aluminum/galvanized steel joints in the VP-CMT process. Journal of Manufacturing Processes, 58, 894-904.

[115] Yagati, K. P., Bathe, R., Joardar, J., Phaniprabhakar, K. V., Padmanabham, G. (2019). Al–Steel Joining by CMT Weld Brazing: Effect of Filler Wire Composition and Pulsing on the Interface and Mechanical Properties. Transactions of Indian Institute of Metals, 72, 2763.

[116] Yan, J., Gao, M., Zeng, X. (2010). Study on microstructure and mechanical properties of 304 stainless steel joints by TIG, laser and laser-TIG hybrid welding. Optics and Lasers in Engineering, 48, 512-517.

[117] Yang, J., Hu, A., Li, Y., Zhang, P., Saha, D. C., Yu, Z. (2019). Heat input, intermetallic compounds and mechanical properties of Al/steel cold metal transfer joints. Journal of Materials Processing Technology, 272, 40-46.

[118] Yang, W., Chen, D., Liu, H., Feng, S., Tang. (2013). Research on the welding process of high nitrogen steels with mid-thickness by MIG welding. International conference on education technology and information system (ICETIS).

[119] Yu, S., Tarasov, A. V, Vorontsov, S. V., Rubtsov, V. E, Krasnoveikin, V. A, Kolubaev, E. A. (2019). Ultrasonic-assisted laser welding on AISI 321 stainless steel. Welding in the World, 63, 875-886.

[120] Yuan, T., Kou, S., Luo, Z. (2016). Grain refining by ultrasonic stirring of the weld pool. Acta Materialia, 106, 144-154.

[121] Zhang, C., Li, G., Gao, M., Yan, J., Zeng, X. (2013). Microstructure and process characterization of laser-cold metal transfer hybrid welding of AA6061 aluminum alloy. International Journal Advanced Manufacturing Technology, 68, 1253-1260.

[122] Zhang, H. T. Feng, J. C., He, P. (2008). Interfacial phenomena of cold metal transfer (CMT) welding of zinc coated steel and wrought aluminium. Materials Science Technology, 24, 346-1349.

[123] Zhang, H., Wang, Y., Han, T., Bao, L., Wu, Q., Gu, S. (2020). Numerical and experimental investigation of the formation mechanism and the distribution of the welding residual stress induced by the hybrid laser arc welding of AH36 steel in a butt joint configuration. Journal of Manufacturing Processes, 51, 95-108.

[124] Zhang., C., Li, Y., Gao, M., Zeng, X. (2018). Wire arc additive manufacturing of Al-6Mg alloy using variable polarity cold metal transfer arc as power source. Materials Science & Engineering A, 711, 415–423.

[125] Zhao, G., Wang, Z., Hu, S., Duan, S., Chen, Y., (2020). Effect of ultrasonic vibration of molten pool on microstructure and mechanical

properties of Ti-6Al-4V joints prepared via CMT+ P welding. Journal of Manufacturing Processes, 52, 193-202.

[126] Zhou, J., Shen, J., Hu, S., Zhao, G., Wang, Q. (2019). Microstructure and mechanical properties of AISI 430 ferritic stainless-steel joints fabricated by cold metal transfer welding. Materials Research Express, 6, 116536.

[127] Zhou, S., Ma, G., Wu, D., Chai, D., Lei, M. (2018). Ultrasonic vibration assisted laser welding of nickel-based alloy and Austenite stainless steel. Journal of Manufacturing Processes, 31, 759-767.

LIST OF PUBLICATIONS

List of papers published in SCI/SCIE journals

1. Jayanta Ghosh Roy, N. Yuvaraj, Vipin Effect of welding parameters on mechanical properties of Cold Metal Transfer welded thin AISI 304 stainless-steel sheets. ***Transactions of Indian Instiute of Metals****,* (2021), 74(9):2397–2408, https://doi.org/10.1007/s12666-021-02326-2. **(Impact factor: 1.205).**

2. N.Yuvaraj, Jayanta Ghosh Roy, Vipin, Enhancement of Microstructural and Mechanical Properties of Ultrasonic Vibration-Assisted Cold Metal Transfer Welding of 304 Stainless Steel. ***Journal of Material Engineering and Performance*** (2022). https://doi.org/10.1007/s11665-022-06877-3. **(Impact factor: 1.819).**

List of papers published in International Conferences

1. J.Ghosh Roy, N.Yuvraj, Vipin "Study of mechanical properties of austenitic stainless steel with GMAW process" ICAPIE 2018, DTU, Delhi.

2. J.Ghosh Roy, N.Yuvraj, Vipin "A comparative experimental study with and without epoxy bonded thin sheet AISI 304 TIG welded lap joint" IMRSE, 2021, NIT Jalandhar.

CURRICULUM VITAE

JAYANTA GHOSH ROY obtained his Bachelor of Science in 1979 from A.B.N.S. College (Formerly known as Victoria College) West Bengal, India, Bachelor's degree in 1983, Mechanical Engineering from Jalpaiguri Government Engineering College, West Bengal, India, and Masters Degree in 1989, Mechanical Engineering from Indian Institute of Technology (I.I.T), Delhi, India. He worked in Testing, analysis, Research, and Calibration in National Test House, Govt. of India, at Ghaziabad, in the position of Scientist-A from 1984 to 1995. Then he has been working as an Associate Professor in the Department of Mechanical Engineering, Aryabhatt Institute Technology, Delhi-110033, Under Deptt. of Training and Technical Education, Govt. of N.C.T of Delhi. He is doing active research in the area of welding and industrial maintenance. He also got Research Excellence Award for commendable research in January 2022 from Delhi Technological University.